2015

A modeling-based assessment of acousto-optic sensing for monitoring high-intensity focused ultrasound lesion formation

BOSTON UNIVERSITY

COLLEGE OF ENGINEERING

Dissertation

A MODELING-BASED ASSESSMENT OF ACOUSTO-OPTIC SENSING FOR MONITORING HIGH-INTENSITY FOCUSED ULTRASOUND LESION FORMATION

by

MATTHEW TYLER ADAMS

B.S., Union College, 2009

M.S., Boston University, 2012

Submitted in partial fulfillment of the

requirements for the degree of

Doctor of Philosophy

2015

Approved by

First Reader

Ronald A. Roy
Professor of Mechanical Engineering
University of Oxford
Adjunct Professor of Mechanical Engineering

Second Reader

Robin O. Cleveland
Professor of Engineering Science
University of Oxford
Adjunct Professor of Mechanical Engineering

Third Reader

Tyrone M. Porter
Associate Professor of Mechanical Engineering
Associate Professor of Biomedical Engineering

Fourth Reader

Aaron J. Schmidt
Assistant Professor of Mechanical Engineering

Acknowledgments

Over the course the past five years I have spent undertaking my PhD research, I have received a tremendous amount of help, both professionally and personally, from a number of important people in my life. I owe each and every one of them a sincere thank you. I have been extremely lucky to study under the supervision of two excellent advisors, Drs. Ron Roy and Robin Cleveland, who have both been flexible, patient, and encouraging role models. I would like to thank them not only for showing me how to be a first-class scientist, but also for providing me with a support structure throughout all of my endeavors. Over the course of my degree I have presented at numerous conferences, attended a summer school, taken off an entire summer to work as an intern for the Navy, and spent nine months as a visiting research fellow at the University of Oxford. Thank you for allowing me all of these amazing opportunities.

One of the best perks of studying at Boston University was the opportunity to be near my friends and family. I am lucky to have had a great, big, and always interesting family within a short driving distance, and to have spent as much time as I have with amazing friends. Thank you all for providing me with an excellent balance between work and fun, and for helping me keep perspective as to what is important. I'd particularly like to thank my parents, Robin and Phil, for all of their support (and their food), and my siblings Andrew, Mike, Allie, and Chris for always keeping things light and fun. To my friends, and especially my girlfriend Olivia, thank you all for helping make the past five years some of the best of my life.

I would also like to thank many of my colleagues and labmates from the last five years. I'd like to particularly acknowledge Jim McLaughlan, who put up with me when I was a clueless and pestering first year graduate student. Thanks for showing me the ropes. Other BU labmates deserving recognition are Puxiang Lai, Dave Giraud, Qi Wang, Andy Draudt, and Jon Kracht; each of whom helped me

with my research in some way. I would also like to thank Drs. Glynn Holt, Tyrone Porter, and Aaron Schmidt; all of whom have served on both my PhD qualifying exam committee and my dissertation defense committee. I'd like to thank the entire BUBBL at Oxford for hosting me during my fellowship, for making me feel welcome during my stay, and for helping me experience the (pub) culture of the UK. Finally, I would like to thank the people at the Naval Surface Warfare Center for allowing me to work on some incredibly interesting projects. Living on the beach wasn't a bad perk either. Thanks to Drs. Mike Strand and Joe Lopes, along with Dave Malphurs, for being my mentors during the summer, and to the other interns for all of the great times outside of the lab.

Financial support for this research was provided by the Gordon Center for Subsurface Sensing and Imaging Systems (NSF ERC Award Number EEC-9986821), the Boston University College of Engineering, and the Whitaker International Fellowship Program.

A MODELING-BASED ASSESSMENT OF ACOUSTO-OPTIC SENSING FOR MONITORING HIGH-INTENSITY FOCUSED ULTRASOUND LESION FORMATION

MATTHEW TYLER ADAMS

Boston University, College of Engineering, 2015

Major Professor: Ronald A. Roy, Professor of Mechanical Engineering, University of Oxford
Co-advisor: Robin O. Cleveland, Professor of Engineering Science, University of Oxford

ABSTRACT

Real-time acousto-optic (AO) sensing – a dual-wave modality that combines ultrasound with diffuse light to probe the optical properties of turbid media – has been demonstrated to non-invasively detect changes in *ex vivo* tissue optical properties during high-intensity focused ultrasound (HIFU) exposure. The AO signal indicates the onset of lesion formation and predicts resulting lesion volumes. Although proof-of-concept experiments have been successful, many of the underlying parameters and mechanisms affecting thermally induced optical property changes and the AO detectability of HIFU lesion formation are not well understood. In thesis, a numerical simulation was developed to model the AO sensing process and capture the relevant acoustic, thermal, and optical transport processes.

The simulation required data that described how optical properties changed with heating. Experiments were carried out where excised chicken breast was exposed to

thermal bath heating and changes in the optical absorption and scattering spectra (500 nm – 1100 nm) were measured using a scanning spectrophotometer and an integrating sphere assembly. Results showed that the standard thermal dose model currently used for guiding HIFU treatments needs to be adjusted to describe thermally induced optical property changes.

To model the entire AO process, coupled models were used for ultrasound propagation, tissue heating, and diffusive light transport. The angular spectrum method was used to model the acoustic field from the HIFU source. Spatial-temporal temperature elevations induced by the absorption of ultrasound were modeled using a finite-difference time-domain solution to the Pennes bioheat equation. The thermal dose model was then used to determine optical properties based on the temperature history. The diffuse optical field in the tissue was then calculated using a GPU-accelerated Monte Carlo algorithm, which accounted for light-sound interactions and AO signal detection. The simulation was used to determine the optimal design for an AO guided HIFU system by evaluating the robustness of the systems signal to changes in tissue thickness, lesion optical contrast, and lesion location. It was determined that AO sensing is a clinically viable technique for guiding the ablation of large volumes and that real-time sensing may be feasible in the breast and prostate.

Contents

List of Tables

List of Figures

List of Abbreviations

AO	.....	Acousto-Optic
AOCT	.....	Acousto-Optic Coherence Tomography
AOI	.....	Acousto-Optic Imaging
APD	.....	Avalanche Photodiode
ARFI	.....	Acoustic Radiation Force Impulse Imaging
CCD	.....	Charged-Coupled Device
CEM	.....	Cumulative Equivalent Minutes
CMOS	.....	Complementary Metal-Oxide-Semiconductor
CFPI	.....	Confocal Fabry-Pérot Interferomer
CW	.....	Continuous Wave
DAQ	.....	Data Acquisition
DOT	.....	Diffuse Optical Tomography
DRA	.....	Diffuse Reflectance Accessory
FUS	.....	Focused Ultrasound Surgery
FDTD	.....	Finite-Difference Time-Domain
GPU	.....	Graphics Processing Unit
HIFU	.....	High-Intensity Focused Ultrasound
IAD	.....	Inverse Adding–Doubling
LP	.....	Low Pass
LSE	.....	Least-Squares Error
MCX	.....	Monte Carlo eXtreme
MR	.....	Magnetic Resonance
NIR	.....	Near Infrared
PAM	.....	Passive Acoustic Mapping
PCD	.....	Passive Cavitation Detector
PMT	.....	Photomultiplier Tube
PRC	.....	Photorefractive Crystal
RMS	.....	Root Mean Square
RTE	.....	Radiative Transfer Equation
SHB	.....	Spectral Hole Burning
SNR	.....	Signal-to-Noise Ratio
TWM	.....	Two Wave Mixing

Chapter 1

Introduction

1.1 HIFU for the Treatment of Cancer

1.1.1 HIFU Background and Principles

Ultrasound has long been employed as a diagnostic medical tool, providing real time images with fine spatial resolution deep within the body. However, therapeutic ultrasound is also emerging as a promising non-invasive alternative to open surgery for the resection of solid, cancerous tumors (Kennedy, 2005; ter Haar and Coussios, 2007a; Coussios and Roy, 2008). Additional therapeutic applications include the treatment of bone and soft tissue injuries (Watson, 2008), the destruction of kidney stones and gall stones (Rassweiler et al., 2011), and targeted drug delivery (Mo et al., 2012). High-intensity focused ultrasound (HIFU), otherwise known as focused ultrasound surgery (FUS), was first investigated as a method for the thermal ablation of tumors in the 1940's (Lynn et al., 1942; Lynn and Putnam, 1944). The technique uses either spherically focused single-element ultrasound transducers or phased arrays to create significantly localized region of high pressures. The energy of the ultrasound is absorbed by the tissue and converted to heat, causing the cells in the ultrasonic focus – a volume which is approximately the size and shape as a grain of rice for a typical HIFU frequency of 1 MHz – to rapidly undergo irreversible coagulative necrosis, while leaving the surrounding tissue undamaged (ter Haar, 1995; ter Haar and Coussios, 2007b). The concept is illustrated in Fig. 1·1, and the region of tissue that is destroyed is referred to here as a lesion. In addition to the thermal effects caused by

ultrasound absorption, mechanical effects such as high shear stresses and cavitation can cause further ablation within the HIFU focus (Coussios et al., 2007). In order to ablate large volumes of tissue, there are two strategies. The surgeon may either create an array of lesions one at a time, or may continuously scan the HIFU transducer to create one large lesion (ter Haar, 2012).

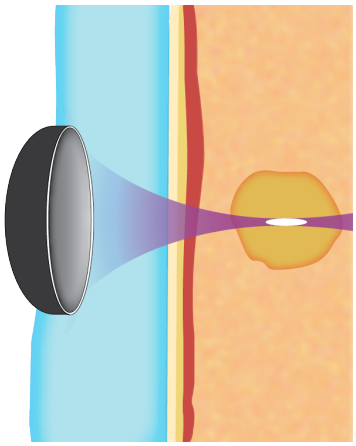

Figure 1·1: An illustration of non-invasive tumor ablation with HIFU. The megahertz-frequency ultrasound traverses the intervening tissue and creates a lesion about the size and shape of a grain of rice at the focus inside of the tumor.

To date, HIFU has been used clinically in the treatment of tumors of the prostate, breast, brain, liver, kidney, uterine, pancreas, and bone (Kennedy, 2005; Al-Bataineh et al., 2012). These exploratory treatments have been investigated using commercially available systems guided by either diagnostic ultrasound or Magnetic Resonance (MR) imaging. These guidance methods, along with several other developmental technologies, are discussed in detail in Section 1.1.3.

1.1.2 The Role of HIFU in Cancer Therapy

Several methods currently exist for the palliative and curative treatment of cancer. The most firmly established treatment methods are chemotherapy, open surgery, hormonal therapy, immunotherapy, gene therapy, radiotherapy, radio frequency ablation,

cryoablation, laser ablation, and electroporation (Pazdur and Hoskins, 2003). The last five techniques listed are considered minimally invasive. Several of these approaches are often used in combination in an effort to more effectively treat the disease.

HIFU shows great promise as an alternative to both open surgery and the minimally-invasive techniques listed above. Advantages include: a reduced risk of infection, resulting in decreased mortality and morbidity (Kennedy, 2005), leaving necrosed tumor tissue *in situ*, which has been shown to result in an increased immune response (Wu et al., 2001, 2007), and minimal risk of hemorrhage from visceral or vascular puncture provided the HIFU exposure is operated to avoid excessive cavitation or boiling activity. Moreover, HIFU is completely non-ionizing. Consequently, treatments can be repeated without any lasting damage being done to the patient, and with no risk of side effects other than minor skin burns (Wu et al., 2001, 2004; Illing et al., 2005). Overall, HIFU shows promise as a supplement to any type of cancer therapy, but it is particularly applicable as a non-invasive and non-ionizing alternative to open surgery and radiotherapy for the treatment of deep-seated, solid tumors.

1.1.3 HIFU Guidance

As HIFU is completely non-invasive and treatment planning is difficult due to patient and time-dependent environmental factors – blood flow, respiration, body temperature, intervening tissue heterogeneities, etc. – a reliable treatment monitoring and guidance technique is imperative for its efficacy and its clinical acceptance (Rivens et al., 2007). The likelihood that a given set of exposure parameters will result in lesion formation is difficult to ensure *a priori*, owing the complexity of the situation. Targeting errors, changes in perfusion blood cooling, and the presence or absence of cavitation all impact the location, volume, and shape of a HIFU lesion. Since the treatment of a large volume usually requires that multiple lesions be formed, and some therapies are performed in sensitive organs where minimizing the damage to

surrounding healthy tissue is imperative, it is extremely desirable to be able to monitor treatment progress in real time for each lesion that is created. A surgeon must be certain that the target volume is adequately treated, while ensuring that surrounding or intervening healthy tissue is unaffected. To date, diagnostic ultrasound (ter Haar et al., 1989; Sanghvi et al., 1996; Wu et al., 2004) and magnetic resonance (MR) thermometry (Hynynen et al., 1996; McDannold, 2005) are the only two guidance methods that have seen substantial clinical use. While each of these techniques have particular advantages and disadvantages, they both leave much to be desired in the way of providing reliable and cost-effective real-time feedback for HIFU guidance.

B-mode images from diagnostic ultrasound scanners have been used to image HIFU induced tissue damage since the 1970's (Fry et al., 1970), and have been widely employed in the years since due to their low cost, portability, and capability of imaging in real-time. Although these factors certainly make diagnostic ultrasound guidance an attractive option, there is a fundamental problem with the approach. It has been demonstrated that there is insufficient contrast between necrotic and healthy tissue to reliably image HIFU lesions on a B-mode scan (Hill and Ter Haar, 1995; Vaezy et al., 2001; Rabkin et al., 2005, 2006; Coussios et al., 2007). Instead, the use of B-mode imaging for HIFU guidance relies on enhanced echogenecity associated with the generation of sizable, stable gas and/or vapor bubbles generated within the treatment volume. The bubbles are either generated by the substantial tensile stress present in intense sound fields (i.e. acoustic cavitation) or by elevated temperatures induced by HIFU heating (i.e. boiling). When present, these bubbles have been shown to produce unpredictable and abnormally formed lesions (Meaney et al., 2000; Bailey et al., 2001; Khokhlova et al., 2009). In addition to the unpredictability of lesion formation associated with the generation of vapor bubbles, some studies have found no correlation between the presence of enhanced echogenicity on a scan and

the rate of tumor destruction (Sibille et al., 1993). Moreover, it is possible, and in some cases desirable, to generate HIFU lesions in tissue without boiling or excessive cavitation activity, resulting in necrotic tissue that is not visible in a B-mode image, as demonstrated in Fig. 1·2.

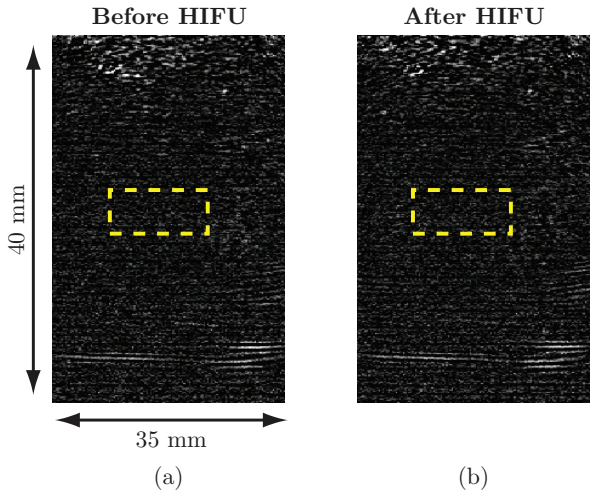

Figure 1·2: B-mode images of *ex vivo* chicken breast obtained immediately before (a) and after (b) a 40 s HIFU exposure with a target peak positive pressure of 10 MPa and a frequency of 1.1 MHz, resulting in an approximately 200 mm^3 lesion. The HIFU focus is located inside of the dashed yellow boxes. (Images courtesy of Dr. Puxiang Lai, Washington University in St. Louis)

Unlike diagnostic ultrasound, which directly measures mechanical changes in tissue, MR thermometry uses measurements of proton resonance frequency shifts to calculate temperature rise (Ishihara et al., 1995) and from this infers the likelihood of lesion formation based on the temperature-time history of the target volume. MR thermometry is currently considered the "gold standard" for HIFU guidance (Rivens et al., 2007; Goldberg et al., 2009; Tempany et al., 2011). Current systems are able to provide two dimensional, quasi-real time temperature measurements *in situ* every 1-5 s with a spatial resolution on the order of 1-2 mm, with a trade-off between speed and accuracy (Rivens et al., 2007). An example of the image that a surgeon sees

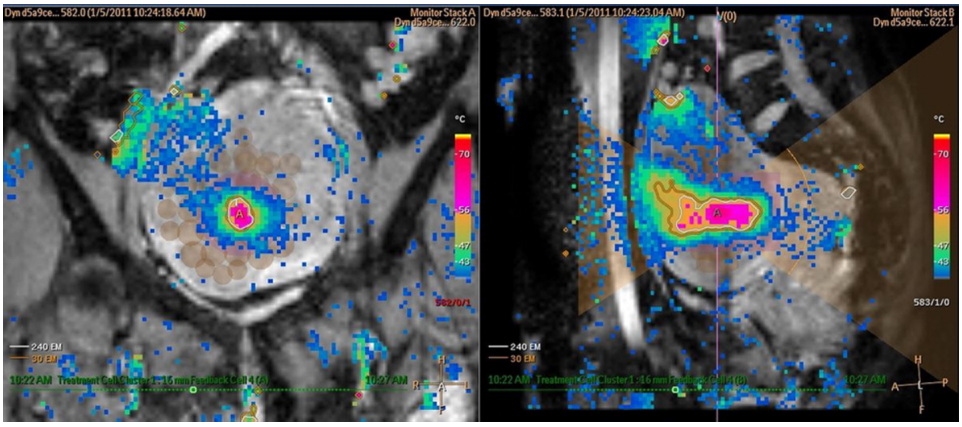

Figure 1·3: Coronal (a) and sagittal (b) plane temperature maps seen by a surgeon during uterine fibroid ablation using a Phillips Sonalleve MR-HIFU machine. Typical temperature voxels are 2.5 x 2.5 x 7 mm^3 and temperature maps are acquired every 2.9 s. Spatially-dependent thermal dose is calculated at every temperature acquisition, and the areas which have accumulated a thermal dose of 30 equivalent minutes and 240 equivalent minutes are outlined in yellow and white, respectively. The image displayed under the temperature map is acquired before treatment, and an estimation of the acoustic field is overlaid in light orange (Kim et al., 2014).

during the treatment is shown in Fig. 1·3. MR thermometry measures temperature, and not a damage dependent lesion property; therefore it is an indirect measurement. Consequently, a temperature dependent model is needed to infer the thermal damage inflicted by temperature elevation. These models may not accurately predict tissue ablation (Church, 2007). MR guided HIFU systems using the CEM_{43} thermal dose model (Sapareto and Dewey, 1984) to calculate the likelihood of thermal damage are the current gold standard for HIFU guidance (Tempany et al., 2011). However, they are expensive, complex, non-portable, and sensitive to patient movement (Kennedy, 2005).

The weaknesses associated with both ultrasound and MR guidance techniques elicit the motive for new approaches to monitoring lesion formation. The development of new HIFU guidance techniques is an active area of research, and several different

methods are currently under development which range from techniques that leverage the contrast between the shear modulus of normal and lesioned tissue – including elastography (Righetti et al., 1999) and acoustic radiation force impulse imaging (ARFI) (Nightingale et al., 2001) – to techniques which image bubble activity in the HIFU focus, such as passive acoustic mapping (PAM) (Nandlall et al., 2011; Jensen et al., 2012). Another alternative method for monitoring HIFU lesion formation is to image or sense optical properties as they change with thermal damage. Thermal necrosis induces large changes in the optical absorption and scattering coefficients of tissues, and thus exhibit high optical contrast as shown in Fig. 1·4. Although there is a high optical contrast between lesioned and native tissue, the the high scattering coefficients possessed by biological tissues limit the spatial resolution at which optical systems are able to sense or image contrast within the body. Alternatively, dual-wave imaging methods – such as photoacoustics (Xu and Wang, 2006) and acousto-optics – utilize the interaction between light and sound to image optical contrast at depth with a spatial resolution dictated by the ultrasound beam.

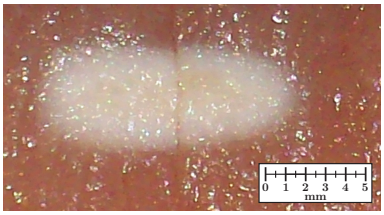

Figure 1·4: Cross-section photo of a lesion created in *ex vivo* chicken breast by a 50 s HIFU exposure with a target peak positive pressure of 10 MPa and a frequency of 1.1 MHz. The ultrasound propagated from left to right and its focal plane was in the center of the lesion. (Courtesy of Dr. Puxiang Lai, Washington University in St. Louis.)

Although photoacoustic and acousto-optic (AO) techniques both use light-sound interactions to image optical contrast with acoustic resolution, their operating principles are very different. Photoacoustic imaging operates by detecting ultrasound emitted by a volume of tissue as it rapidly expands following the absorption of a

short pulse of light – an effect which is dependent on both the temperature and optical absorption properties of the tissue. Therefore, photoacoustic techniques hold an advantage over acousto-optic techniques for HIFU guidance as they can either measure temperature (Nikitin et al., 2012) or optical changes (Khokhlova et al., 2006; Chitnis et al., 2010; Prost et al., 2012; Alhamami et al., 2014), albeit with a penetration depth severely limited by acoustic absorption and optical exposure limits. Alternatively, AO techniques operate by detecting phase modulations which are imparted on diffuse light as it passes through an ultrasound beam. This technique boasts several advantages over photoacoustics. AO sensing is inherently sensitive to both optical absorption and scattering. Additionally, AO sensing does not rely on sensitive noise detection and thus can be utilized in real time, while the HIFU field is turned on. Finally, AO can sense contrast at deeper depths and with better spatial resolution at depth. Recently, AO sensing of thermally induced changes in the optical properties of *ex vivo* tissues has been demonstrated as a viable technique for monitoring non-cavitating HIFU exposures in real time (Lai et al., 2011; Murray et al., 2012). The technique is the subject of this thesis, and it will be discussed in detail in the following section.

1.2 Acousto-Optic Imaging and Sensing

1.2.1 AO Background and Principles

Optical imaging is gaining traction as a powerful diagnostic tool for an assortment of medical applications, as the interaction of light with tissue has been shown to reveal detailed structural and functional information (Tuchin, 2002). In addition to the large amount of information available from optical imaging, it is also a desirable modality because it is non-ionizing and it is completely innocuous at low intensities (ANSI, 2007, 2005; International Commission on Non-Ionizing Radiation Protection,

1996). Unfortunately, the applicability of optical imaging at depth is limited in tissue due to the absorption of light by tissue chromophores – hemoglobin, melanin, water, etc. – and the strong scattering of light from variations in refractive index (Cheong et al., 1990; Jacques, 2013). To avoid strong absorption deep inside of tissue, near infrared (NIR) light with a wavelength in the 'biological window' (650-900 nm), where tissue chromophores display low absorption, can be used (Vo-Dinh, 2010; Wang and Wu, 2012). Additionally, certain tissues such as brain (Yaroslavsky et al., 2002), breast (Pifferi et al., 2004), and prostate (Pantelides et al., 1990) are deemed optically penetrable as they possess much lower absorption than highly perfused tissues such as liver. Unfortunately, scattering is still a dominant factor when illuminating tissue with light in the biological window. In practice, scattering typically limits the penetration of light to ∼6-7 cm in tissue, and spatial resolution is limited to ∼10 mm using standard diffuse optical imaging techniques such as diffuse optical tomography (DOT) (Arridge, 1999; Boas et al., 2001). While scattering does fundamentally limit the penetration depth of light within tissue, spatial resolution can be improved using multimodal techniques such as photoacoustics or acousto-optics.

Acousto-optic imaging (AOI) – otherwise known as ultrasound modulated optical tomography (Wang and Zhao, 1997), acousto-optic tomography (Kempe et al., 1997; Forget et al., 2003), and ultrasound tagging of light (Marks et al., 1993; Mahan et al., 1998) – is a dual-wave modality that uses ultrasound to phase modulate diffuse light at depth in turbid media in order to image optical contrast with a spatial resolution dictated by the dimensions of the ultrasound beam (Dolfi and Micheron, 1992; Marks et al., 1993; Leutz and Maret, 1995; Wang et al., 1995b). By measuring the flux and magnitude of the phase modulations of the modulated, or "tagged", light (Leveque et al., 1999), one is able to infer the optical properties of the tissue in the HIFU focus.

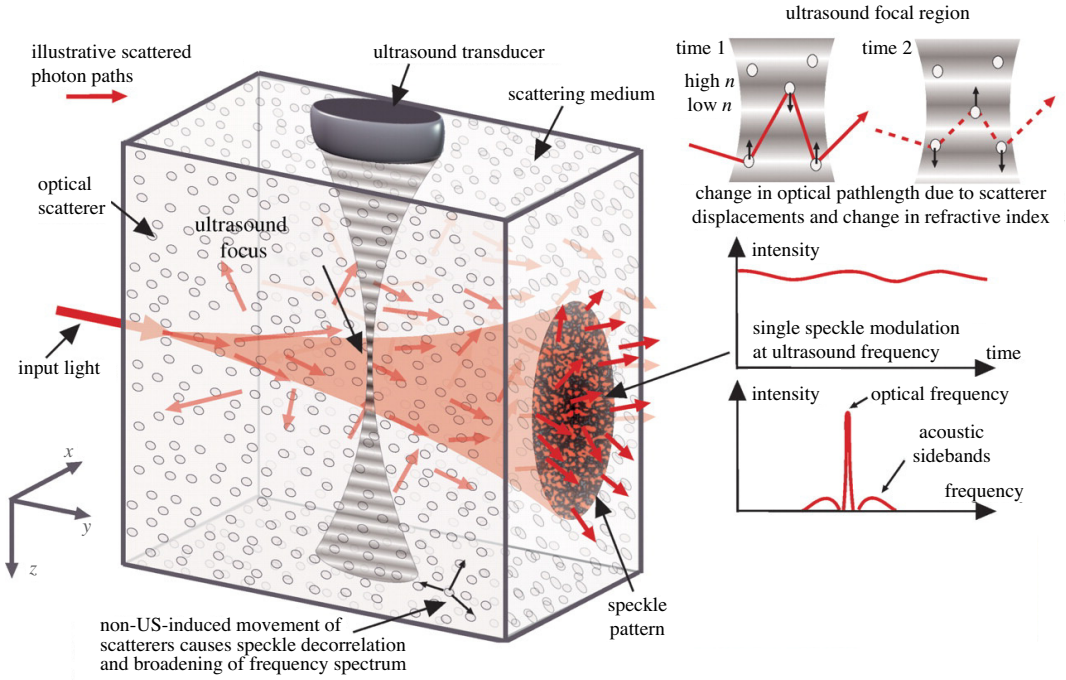

Figure 1·5: Illustration of the principles of AO imaging and sensing. As diffuse light propagates through the focused ultrasound beam, it becomes phase modulated by periodic scatterer displacements and periodic modulations in the refractive index. The intensity modulation of a single speckle grain is shown in the time and frequency domain. Note that scattering is low in this illustration and that no absorbers are included. Image reproduced from Elson et al. (2011).

Figure 1·5 illustrates the working principles of AOI. The sample being imaged is simultaneously illuminated and insonified with either pulsed or continuous wave (CW) light and sound. As light propagates through the medium, each individual photon traverses a unique optical path, with the average distance between consecutive scattering events given by the scattering mean free path, or the reciprocal of the scattering coefficient. (A detailed description of light propagation in tissue is provided in Chapter 2.) When the tissue is under insonification from the ultrasound, the optical scatterers inside of the ultrasound field are periodically displaced with a magnitude proportional to the local acoustic pressure. Additionally, the ultrasound induces

a periodic compression and rarefaction inside of the tissue, resulting in a periodic density and thus refractive index variation that is proportional to the local pressure. Therefore, each photon path experiences a unique modulation in its optical path as it traverses through the ultrasound field due to the displacement of scatterers and the changing refractive index. (Further details on ultrasound induced modulation of light can be found in Chapter 3.) The two described mechanisms (Marks et al., 1993; Leutz and Maret, 1995; Wang, 2001b,a) and the correlation between them (Sakadžić and Wang, 2005) result in a net cumulative phase shift of the light propagating through the tissue. It should be noted that density variations also result in a small amplitude modulation of the light, but the amplitude modulation is a much smaller effect than the phase modulation and has not been observed experimentally (Wang and Zhao, 1997).

Because the magnitude of the ultrasound induced phase shift is dependent upon a combination of the optical properties of the medium and the local acoustic pressure, the net phase shifts are significantly more sensitive to the optical properties in the acoustic focus than elsewhere in the field (Murray et al., 2004; Ramaz et al., 2004; Sakadžić and Wang, 2004; Xu et al., 2007; Li et al., 2008b; Rousseau et al., 2008; Lai et al., 2009). Thus, the area where the focus of the ultrasound is coincident with diffuse light is termed the "AO interaction volume" (Murray and Roy, 2008), and the dimensions of this volume characterize the spatial resolution of the system. In order to construct an image, the interaction volume can be scanned in one, two, or three dimensions. However, it may prove sufficient to monitor or measure optical properties at one location, in which case the interaction volume remains stationary. This is referred to as AO sensing (Lai et al., 2011).

The optical field in the sample is a composition of the partial waves that propagate along unique optical paths. The interference between each of these paths causes

a speckle pattern to form at the tissue boundaries (Goodman, 2007), as shown in Fig. 1·5. Because the phase of the light at each speckle grain is independent, the ultrasound induced phase modulations are not correlated from speckle to speckle and are therefore spatially incoherent. Because of this spatial incoherence, detection cannot be performed with a large single aperture photodetector. Additionally, due to tissue motion and blood flow, the speckle field is subject to a temporal decorrelation on the order of 0.5 ms *in vivo* (Gross et al., 2005; Lev and Sfez, 2003). Consequently, the detection of AO signals is non-trivial. The primary AO detection methods currently in use are discussed in the following section.

1.2.2 AO Detection Methods

The purpose of this section is to present a comprehensive survey of the primary AO detection methods currently in use. A detailed analysis of each method is beyond the scope of this discussion, however a more complete review may be found in Elson et al. (2011). In reviewing detection methods, a clear distinction can be made between incoherent techniques – based on spectral filtering of the scattered light to select the acoustic sidebands – and coherent techniques which measure ultrasound induced phase modulations by detecting an intensity modulation. The two established incoherent techniques are presented first, followed by the coherent techniques.

Confocal Fabry-Pérot Interferomer Filtering

A confocal Fabry-Pérot interferomer (CFPI) is a filter consisting of two partially transmitting mirrors aligned to create a reflective cavity. Light enters the cavity and undergoes self-interference due to multiple reflections. The center frequency of the filter is adjustable by controlling the distance between the two mirrors, and the bandwidth is a function of the distance between the mirrors and their reflectivity. To detect tagged photons, the filter is tuned to a center frequency of $\omega_0 \pm \omega_a$, where ω_0

is the optical source frequency and ω_a is the acoustic frequency (Monchalin, 1985; Monchalin et al., 1989). The bandwidth of the filter must be less than ω_a. A single aperture photodetector measures the intensity of the light that passes through the CFPI. By isolating the acoustic sideband, one is able to make a direct measurement of the flux of the modulated light. This has the distinct advantage of being insensitive to complications associated with the spatial and temporal incoherence of the speckle pattern. Most current implementations use multiple passes through the CFPI to reduce the bandwidth of the filter and further reject the light at ω_0 (Sakadžić and Wang, 2004; Rousseau et al., 2009). Unfortunately, in order to achieve sufficient suppression of the unmodulated light, it is generally necessary to use a relatively high ultrasound frequency ($\geq$ 5 MHz). Therefore, a CFPI based detector is best suited for shallow imaging applications, such as high-resolution AO microscopy (Kothapalli and Wang, 2008, 2009).

Spectral Hole Burning

In an attempt to overcome the limitations of a CFPI, spectral hole burning (SHB) has been proposed as an alternative spectral filtering technique for AO detection (Li et al., 2008a,b). An SHB crystal is a rare-earth ion doped, inhomogeneously broadened optical absorber with an inhomogenous bandwidth of a gigahertz. The crystal can be modeled as a two level system, meaning when atoms are in their ground state they possess high absorption properties, but when excited they allow optical transmission. When cryogenically cooled and illuminated with a sufficiently intense laser, an SHB crystal can possess a spectral "hole", or transparency, with a sub-megahertz homogeneous linewidth (Li et al., 2008b). For use with AO detection, a high-power pump laser is frequency shifted to one of the acoustic sidebands and is used to burn a spectral hole in the crystal. Like with CFPI, the light at the acoustic sideband is transmitted through the SHB crystal and is collected with a single aperture photode-

tector. Current implementations use multiple passes through the SHB to improve its filtering efficiency (Xu et al., 2010). This detection method has many advantages. It exhibits a high étendue (light collection efficiency), it is insensitive to the temporal and spatial incoherence of the speckle pattern, and it can be used with an optical wavelength around 800 nm. However, it requires expensive and non-portable equipment, and with recently demonstrated techniques the efficiency of the spectral filter is low, exhibiting a 2.6 dB suppression of the acoustic sideband and an 18 dB suppression of the laser frequency (Xu et al., 2010; Li et al., 2008b).

Point Detection

The first attempts of detecting ultrasound induced phase modulations were made with fast single point detectors, such as photodiodes or photomultiplier tubes (PMTs), that were configured with apertures small enough to monitor intensity modulations in the light from individual speckles (Wang et al., 1995b; Wang and Zhao, 1997). This technique is inherently different from previously discussed detection methods, which measure phase modulations, as it only detects weak intensity modulations caused by changes in optical properties within the HIFU focus. In these studies, an electronic filter was used to isolate the AC component of the detected signal, and thus the modulated light. More recently, other point detection techniques have been demonstrated that either use a local oscillator (Kempe et al., 1997) or a digital autocorrelator (Powell and Leung, 2013a) in order to better measure phase modulations. The advantage of point detection techniques is that they are simple and very fast, allowing detection to be made before the speckle temporally decorrelates due to blood flow or tissue motion (i.e. $\ll 0.5$ ms). Unfortunately, the intensity of the modulated signal detected from a single speckle is extremely weak, and thus the signal-to-noise ratio (SNR) is very poor. It is possible to collect more light by detecting over N_g speckle grains, but the modulation depth of the signal – the total modulated fluence divided by the

unmodulated fluence – decreases with $\sqrt{N_g}$ because of the spatial incoherence of the speckle pattern.

Parallel Speckle Modulation Processing

By detecting over N_g speckle grains with independent sensors, such as the pixels of a camera, the SNR can be improved by $\sqrt{N_g}$ without compromising the modulation depth (Marks et al., 1993; Gleyzes et al., 1995; Leveque et al., 1999). However, the limited acquisition speed of current charged-coupled device (CCD) and complementary metal-oxide-semiconductor (CMOS) cameras prevent them from directly recording AO modulations. In order to work around this limitation, the light source is amplitude modulated at the acoustic frequency, creating a low frequency beating which is detectable by the camera. Four images are recorded, each corresponding to different relative phases between the illumination and the ultrasound. By computing linear combinations of the four images, the amplitude and phase of the modulated light can be recovered at each pixel (Leveque et al., 1999; Yao et al., 2000). However, the time required to acquire the four images is much greater than the speckle decorrelation time, which introduces a large amount of noise. Additionally, data is normally post-processed, so this detection method has not been demonstrated in real time.

Digital Off-Axis Holography

Many of the problems associated with parallel speckle modulation processing arise from the fact that the intensity of the modulated light is very weak compared to the intensity of the unmodulated light. It is necessary to employ detectors with large dynamic ranges to measure these signals, and even then the signal is normally much smaller than the background noise of the detectors. In order to address this issue, Gross et al. (2003) have demonstrated the implementation of digital off-axis heterodyne holography (Le Clerc et al., 2000) for the detection of AO signals. By

splitting the illumination laser prior to reaching the sample to create a local oscillator, then frequency shifting the local oscillator to one of the acoustic sidebands, the signal becomes amplified above the camera's read noise and the system becomes shot-noise limited. Then, by introducing an additional small frequency shift (1/4 of the camera's frame rate) to the local oscillator, the camera records the interference pattern between the signal beam and the local oscillator with four different relative phases. With these four images, the modulation depth can be calculated at each pixel (Yamaguchi and Zhang, 1997). Additionally, by introducing a small angle between the signal beam and the local oscillator, the interference between the signal beam and the local oscillator creates a sinusoidally modulated interference pattern in space. By taking a spatial Fourier transform of the recorded holograms, the interference pattern can selected and the speckle decorrelation noise can be filtered out (Gross et al., 2003). Although the speckle decorrelation noise can be filtered out over long exposure times, fast frame rates are still required to achieve axial resolution – either using pulsed ultrasound or AO coherence tomography (AOCT) (Benoit a la Guillaume et al., 2012). Recently, a state-of-the-art CMOS camera has been developed which functions with a frame rate of 4 kHz and features in-pixel processing for holography based AOCT (Laforest et al., 2013). The 4 kHz frame rate of the camera allows holograms to be recorded before the speckles temporally decorrelate, and the on-board processing dramatically reduces image acquisition times.

Laser Speckle Contrast

In an attempt to detect AO signals from a single camera image, as opposed to the multiple images required for parallel speckle modulation processing or digital holography, Li et al. (2002) proposed an analysis of the blurring of the speckles during the camera exposure time. As the scatterers within the tissue are displaced by the ultrasound during the camera exposure time, the camera records a moving speckle

pattern, causing the speckle grains to appear blurred. By measuring the contrast of the image, the degree of speckle blurring can be determined, and a correlation can be made to the amount of modulated light at the detector. While this technique has the advantage of only requiring one image, the signal is very weak as the images need to be acquired within the temporal coherence time of the speckles, and therefore the SNR is generally poor. Additionally, any small movement of the tissue during the camera exposure time has a large impact on the measured modulation.

Photorefractive Holograpy

Introduced to the field of AOI by Murray et al. (2004) and Ramaz et al. (2004), a photorefractive crystal (PRC) is material whose index of refraction adaptively varies according to the spatial distribution of incident optical illumination (Teich and Saleh, 1991; Solymar et al., 1996). As light is absorbed in a PRC, free carriers (electrons or holes that are free to move throughout the semiconductor lattice) are generated in a process known as photogeneration. Because of spatial concentration gradients, the free carriers diffuse from bright regions in the PRC and become trapped in dark regions[1], resulting in a non-uniform space-charge distribution and thus a spatially modulated electric field. The time required for the formation of this electric field is referred to the PRC response time (Millerd et al., 1998). Because the PRC is electro-optic (i.e. its refractive index is proportional to its internal electric field), the spatially modulated electric field also creates a holographic refractive index pattern which diffracts the incident light.

By splitting the illumination laser prior to the sample, a reference beam is created. When this reference beam is recombined with the signal beam at the PRC, an interference pattern is created, which is then recorded as a hologram inside the

[1] The application of an external field enhances this process and creates a stronger refractive index grating (Delaye et al., 1997; Millerd et al., 1998), resulting in a higher two-wave mixing gain.

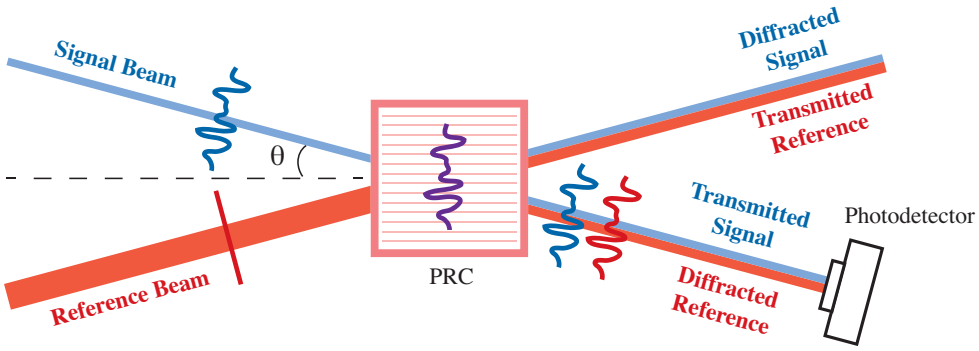

Figure 1·6: An illustration of two wave mixing in a photorefractive crystal. As the complex wavefront of the signal beam interferes with the planar wavefront of the reference beam at the PRC, a complex interference pattern is created and a hologram is recorded. The hologram partially diffracts each of the beams in the direction of the other, perfectly phase matching the reference beam to the signal beam in this case. Detection is then performed with a large single aperture photodetector. Among other factors, the TWM gain is dependent upon the intensity of the beams and the angle between them.

crystal. In a process known as two-wave mixing (TWM), the signal beam and the reference beam exchange energy and a portion of the reference beam is refracted in the direction of the signal beam, creating a constructive interference between the two beams. If the crystal is properly configured (Sui et al., 2005), the two beams will be perfectly in phase, as shown in Fig. 1·6. Ultrasonically induced phase modulation occurs too quickly for the crystal to adapt to. Therefore, ultrasound induced phase modulation in the signal beam translates into spatially coherent intensity modulation in the interference between the signal and reference beams. The entire speckle pattern can then be integrated over a large single aperture detector without averaging out the modulation over multiple speckles. By selecting the frequency of the reference beam to be either the illumination frequency or the acoustic sideband frequency, one can detect either the unmodulated or the modulated light, respectively (Gross et al., 2009). It bears mentioning that it is also possible to perform PRC-based AO detection with a self-referenced signal beam, but the response time of the crystal is

dramatically reduced in this configuration (Benoit a la Guillaume et al., 2013).

The main advantage of a PRC-based detection system is that fast detection can be performed with a single aperture detector over multiple speckles with a large étendue. However, there are also several disadvantages. First, the spectral response of PRCs limits their use to specific wavelengths. Additionally, the response time of the crystal needs to be sufficiently fast to adapt to speckle decorrelation caused by blood flow and physiological movement. While the use of a tellurium-doped tin thiohypodiphosphate (SPS:Td) ferroelectric crystal has been demonstrated at 790 nm, its response time (100 ms) is too slow for *in vivo* applications (Farahi et al., 2010). Likewise, phototorefractive polymer films (Suzuki et al., 2013) have been demonstrated to have large étendues and high TWM gains, achieving AOI in tissue-mimicking phantoms of up to 9.4 cm in thickness (Lai et al., 2013), but their response times are on the order of many seconds. An AO system with a GaAs crystal, which works at a wavelength of 1064 nm, has has been reported to achieve a response time of 0.25 ms, which is compatible with *in vivo* imaging of thick tissues (Lesaffre et al., 2007). Unfortunately, achieving a fast response time requires the use of a very intense reference beam, which then may be scattered and cause an additional noise source at the detector. To date, photorefractive holography based detection with a GaAs crystal is the only technique that has been used for HIFU guidance and this approach will be discussed in further detail in Chapter 3.

Summary

Because of their insensitivity to the decorrelation of both the light source and the speckle pattern, incoherent AO detection techniques appear most suitable for *in vivo* imaging. However, each of the current incoherent detection techniques have significant limitations. The Fabry-Pérot interferometer suffers from a low étendue and a severe lack of robustness because its spectral selectivity is disrupted in the presence

of vibrations. Spectral hole burning has advantages as a detection system, but it has not been widely adopted because it is technically difficult to achieve low enough temperatures to achieve the narrowband filters necessary for AO detection. Among the coherent detection techniques, no clear preference has been made within the AO scientific community. The choice of technique generally depends on the equipment available and the expertise of the researcher employing it. With the development of fast CMOS cameras (Laforest et al., 2013) and high very étendue PRC systems (Lai et al., 2012), both digital off-axis holography and PRC holography techniques show great promise for *in vivo* AO imaging and sensing in thick tissues.

1.2.3 AO Sensing for HIFU Guidance

Using a GaAs PRC-based lock-in detection system, real-time AO sensing of thermally induced changes in the optical properties of *ex vivo* tissues has been demonstrated during non-cavitating HIFU exposures (Lai et al., 2011; Murray et al., 2012). A schematic of the apparatus is presented in Fig. 1·7. Light from a single longitudinal mode 1064 nm Nd:YAG laser is split into a signal beam and a reference beam by a variable beam splitter, which allows the operator to select the power ratio between the beams. The signal beam is then expanded to lower the intensity incident upon the sample, and the reference beam is collimated and expanded to the size of the PRC. The sample is insonified by a 1.1 MHz HIFU transducer, which is 100% amplitude modulated at 50 Hz. The synchronous output from the 50 Hz HIFU modulation signal serves as a reference input for the lock-in amplifier. A passive cavitation detector (PCD) monitors inertial cavitation activity in the HIFU focus during insonication in order to rule out the presence of bubble activity which affects the stability of the AO signal. Diffuse modulated and unmodulated light is collected in transmission through the sample by a large lens, and is focused to the face of the PRC. The sample beam and the reference beam create a hologram in the PRC, and the TWM gain is enhanced

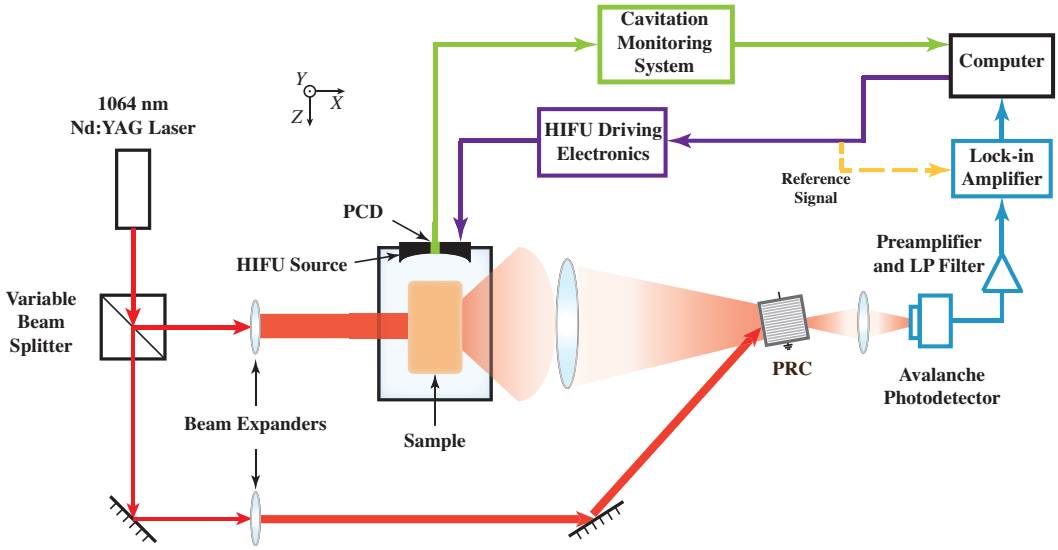

Figure 1·7: A schematic of the apparatus used for real-time sensing of HIFU lesions with PRC-based lock-in detection. The tissue is insonified by the HIFU system along the $+Z$-axis and illuminated by the sample beam along the $+X$-axis. The apparatus consists of four subsystems: a HIFU drive system, an illumination system, a passive cavitation detection system, and a PRC based AO detection system. A synchronization output from the HIFU drive system serves as a reference input for the lock-in amplifier.

by the application of an external AC voltage field. Without any ultrasound, the light at the output of the PRC is a constructive interference between the signal beam and the reference beam. In the presence of ultrasound induced modulations, the PRC can not adapt to the quickly changing signal beam, and the constructive interference between the signal beam and the reference beam is compromised. Therefore, ultrasound induced modulations in the signal beam cause an intensity modulation at the output of the PRC. The light at the output of the PRC is focused by another lens onto the active element of a high-gain and fast-response avalanche photodiode (APD), which is then low-pass (LP) filtered, amplified, and sent to the lock-in amplifier. More details of the setup can be found in Lai et al. (2011).

Because the HIFU drive signal is amplitude modulated, so is the intensity of the

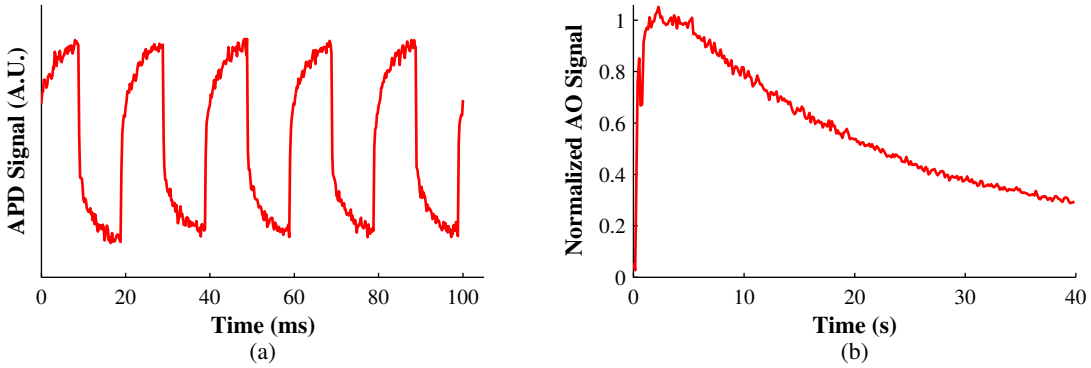

Figure 1·8: (a) A typical time domain AO signal measured at the output of the low-pass (LP) filter (see Fig. 1·7) using a relatively low ultrasound focal pressure (1 MPa peak positive) in *ex vivo* chicken breast. This waveform was obtained by coherently averaging over 1,000 sweeps of the 10-ms HIFU burst, which took more than 20 s. The curvature in the signal is due to the finite response time of the PRC. (b) A typical AO signal at the output of the lock-in amplifier. The exposure was a 10 MPa target peak positive pressure for 40s in *ex vivo* chicken breast. As the optical properties in the HIFU focus change, the AO signal drops in proportion to the lesion volume. The data is taken from Lai et al. (2011).

light measured by the APD, as shown in Fig. 1·8(a). The output of the lock-in amplifier is a low-noise signal that is proportional to the root mean square (RMS) value of the amplitude modulated intensity measured by the APD. More details on this signal are provided in Chapters 3 and 5. Because the amplitude of the modulated intensity at the APD is proportional to the magnitude of the phase modulations, it is a function of the optical properties in the focus of the HIFU. Therefore, by monitoring the output of the lock-in amplifier, one is able to directly monitor the optical properties in the focus of the HIFU. It is this signal that we will term the "real-time AO signal". As the tissue in the HIFU focus undergoes thermal necrosis, its optical properties change and so does the magnitude of the AO signal. Figure 1·8(b) shows the AO signal as a function of time for a 40 s exposure of 10 MPa target peak positive pressure in chicken breast. By making HIFU lesions in *ex vivo*

chicken breasts under many different exposure conditions, Lai et al. (2011), see Fig. 1·9, showed that the resulting lesion volume was a function of the normalized change in the AO signal, independent of the exposure parameters. This motivates the work reported in this thesis.

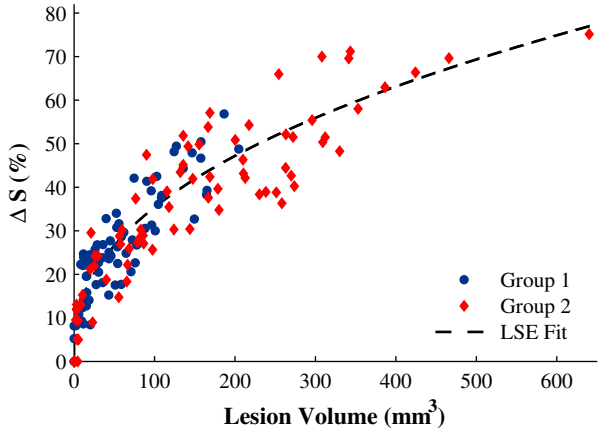

Figure 1·9: The percent reduction in AO signal amplitude (ΔS) as a function of resulting lesion volume for 40 s exposures of a target peak pressure of 8 MPa (group 1) and 5-60 s exposures of 6-10 MPa (group 2) in *ex vivo* chicken breast samples. The least-squares error (LSE) fit of the data is able to predict the resulting lesion volume for all investigated exposures. For more information on the exposure parameters and the fit, see Lai et al. (2011).

1.3 Recapitulation and Specific Aims

The largest barrier to the widespread acceptance of HIFU for the treatment of cancer is the lack of a reliable and accessible feedback and monitoring technique. Improvement in feedback and monitoring will reduce treatment time, will increase the safety and efficacy of treatments, will reduce the costs of treatments, and will increase its accessibility. Real-time AO sensing of lesion formation has been proposed as a supplemental or alternative monitoring technique to the current gold standard of MR thermometry guidance. Although proof-of-concept experiments have demonstrated

the feasibility of real-time AO sensing for HIFU guidance in *ex vivo* tissues, the technique has not been optimized and the parameters which affect the AO detectability of HIFU lesions are not well understood. Not only are system design considerations such as illumination wavelength, detector size, and illumination/detection configuration not well understood, but the literature lacks reliable data to describe the optical contrast between undamaged and thermally lesioned tissues.

The two main goals of this work are to better understand the optical contrast between native and lesioned tissues, and to assess and improve upon current AO guided HIFU techniques using a modeling based approach. To accomplish these goals, the following specific aims are established:

1. Quantify the optical properties of native and thermally necrosed *ex vivo* tissues, and develop a model to describe the kinematics of thermally induced optical property changes.

2. Develop a comprehensive model to describe the AO guidance of HIFU. This includes calculations of acoustic pressure and intensity, temperature changes due to ultrasound absorption and thermal diffusion, thermally induced optical property changes, light propagation, ultrasound induced phase modulations, and AO signal detection.

3. Use the model to determine an optimal design for an AO guided HIFU system, and assess the robustness of its AO signal to changes in factors such as tissue thickness, lesion optical contrast, and lesion location.

4. Use the model to assess the clinical viability of AO guided HIFU by examining its ability to guide the ablation of large volumes, and by predicting the SNR of AO signals in different organ models.

In Chapter 2, the theory of light-tissue interactions and optical property measurements in tissue are presented. These principles are used to introduce measurements of the optical properties of native and thermally necrosed chicken breast tissue, and to develop a time-temperature model to describe the kinematics of thermally induced optical property changes. In Chapter 3, the development of the AO guided HIFU model is presented, including all relevant theory, numerical implementations, and validations. In Chapter 4, the model is employed to accomplish specific aim number 3, and in Chapter 5 modeling results are presented which pertain to specific aim number 4. Finally, a brief summary of the important results from Chapters 2-5 is presented in Chapter 6, and suggestions for future work are made.

Chapter 2

Optical Properties and Thermally Induced Changes

The optical contrast between undamaged and thermally necrosed tissue is the basis for AO guided HIFU. To explain this contrast, a basic understanding of light-tissue interactions is required. This chapter introduces the fundamental concepts of light propagation in tissue, defines the optical properties used to characterize light-tissue interactions, and describes how these properties change with thermal damage. Experiments performed to measure optical properties and their thermal dependence were previously published (Adams et al., 2014), and are again presented here. The results show that thermally induced optical property changes can be predicted using the thermal dose model, provided an appropriate isodose constant is employed. These results are used as a basis for modeling work which is presented in Chapter 3.

2.1 Light-Tissue Interactions

The interactions between light and tissue can generally be described by two dominant mechanisms – absorption and scattering. These mechanisms are governed by the wavelength of the light and the size, shape, density, and chemical composition of the tissue's constituents (cellular organelles, proteins, fibers, etc.). The absorption and scattering of light in tissue are described in the following sections.

2.1.1 Absorption

The absorption of light occurs when the chromophores present in a medium convert the energy of a photon into a different form – typically heat or molecular excitation – resulting in a reduction of the light's intensity. The reduction in the intensity of light passing through a homogeneous, non-scattering medium can be described by the Beer-Lambert law (Wang and Wu, 2012):

$$I(\lambda) = I_0 e^{-\mu_a(\lambda)L}, \tag{2.1}$$

where I_0 is the initial intensity, L is the optical path length within the medium, and μ_a is the wavelength dependent optical absorption coefficient of the medium. The optical absorption coefficient of a medium is a function of the molar concentration, c_i, and the molar absorptivity (or extinction coefficient), ϵ_i, of each chromophore within the medium. Specifically,

$$\mu_a(\lambda) = \sum_{i=1}^{N} c_i \epsilon_i(\lambda) \tag{2.2}$$

where N is the total number of chromophores present in the medium. As a bulk property, μ_a is typically given in units of cm^{-1} and it describes the probability of photon absorption per unit path length. Alternatively, $1/\mu_a$ gives the mean free path between absorption events.

In tissue, the absorption of visible light is dominated by blood – which is dependent upon its oxygenation – and absorption due to water becomes important when using near-infrared (NIR) light. The absorption spectra of these chromophores is shown in Fig. 2·1(a,b). Other chromophores which contribute to the absorption of light in tissue are fat, melanin, billrubin, and beta-carotene (Jacques, 2013). The bulk absorption coefficient of a tissue can be expressed as a linear combination of each of

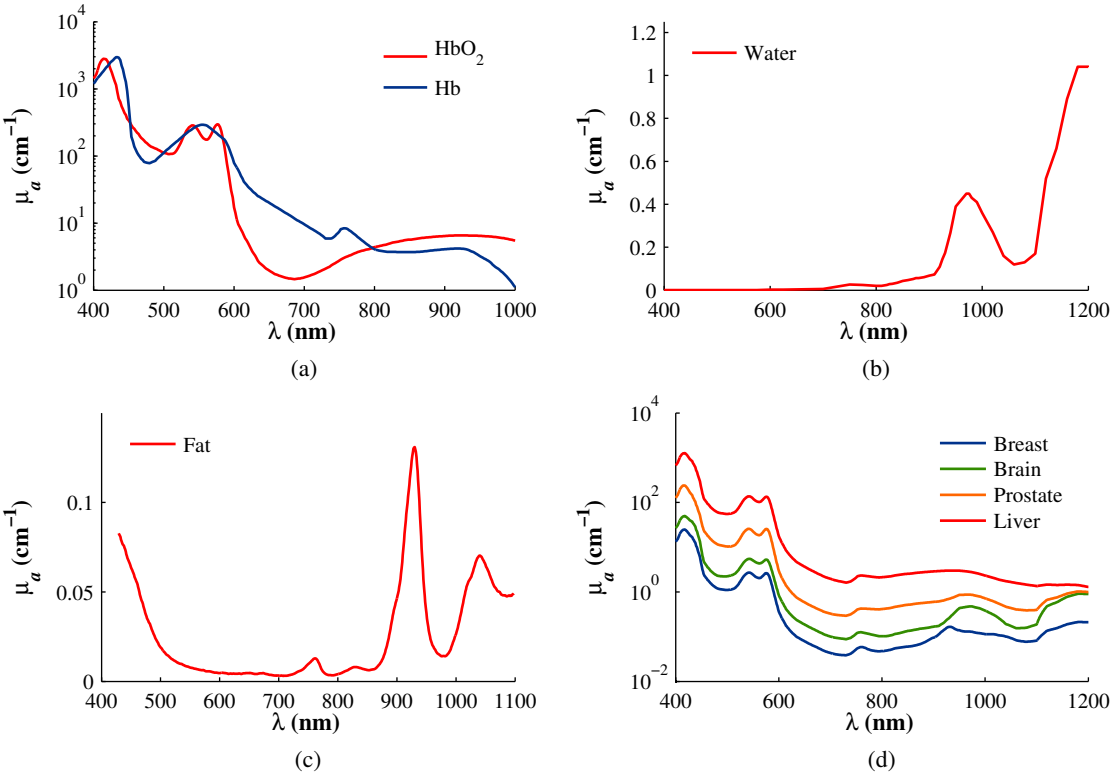

Figure 2·1: Absorption coefficients of dominant chromophores in tissue (a-c) and selected bulk tissues (d). (a) Absorption coefficient of oxyhemoglobin (HbO_2) and deoxyhemoglobin (Hb) (Prahl, 2012a). (b) Absorption coefficient of water (Hale and Querry, 1973). (c) Absorption coefficient of fat (Prahl, 2012a). (d) Approximate absorption coefficients of selected tissues calculated using blood, water, and fat content (Jacques, 2013).

its chromophores:

$$\mu_a(\lambda) = f_b S \mu_{a,HbO_2}(\lambda) + f_b(1-S)\mu_{a,Hb}(\lambda) + f_w \mu_{a,H_2O}(\lambda) + \sum_{i=1}^{N} f_i \mu_{a,i}(\lambda), \quad (2.3)$$

where f is the volume fraction of the blood (b), water (w), or other chromophore (i), S is the oxygen saturation of the hemoglobin (Hb) in the blood, and the summation term is the contribution from all other chromophores. For many tissues this term may be ignored, but in tissues with high fat contents, such as breast, or high melanin

contents, such as dark skin, other chromophores become important. The approximate absorption coefficient of a tissue can be calculated if the concentration of important chromophores and the oxygenation of blood is known (Jacques, 2013), and calculated coefficients for selected organs are shown in Fig. 2·1(d). As shown, tissues with high blood content, such as liver, have very high absorption coefficients, making optical imaging undesirable. Alternatively, tissues such as breast and brain have relatively low absorption coefficients, making them optically penetrable.

2.1.2 Scattering

Optical scattering originates from the refraction and/or reflection of light as it passes through spatial gradients, or interacts with discrete discontinuities, in the medium's index of refraction, n. The refractive index is a non-dimensional parameter given by the speed of light *in vacuo* divided by the speed of light in the medium. To first order, scattering alters light trajectory without incurring energy loss, whereas absorption dissipates light energy without impacting trajectory. In tissue, optical scattering dominates over absorption, as light scatters off of biological structures with sizes ranging from cell membranes ($\sim$0.01 μm) to whole cells ($\sim$10 μm). In general, the larger the size of a scattering structure (relative to the optical wavelength) and the greater the difference in refractive index, the greater the scattering cross section will be. In most healthy biological tissues, the structures with the highest scattering cross sections are cell nuclei and mitochondria which both have characteristic dimensions on the order of 1 μm and both have refractive indices of 1.38–1.41, compared to $\sim$1.36 for extracellular fluid and cytoplasm (Drezek et al., 1999; Wang and Wu, 2012). Like absorption, the process of multiple scattering in bulk tissue can be described as the probability of a photon experiencing a scattering event per unit length, and is given by μ_s. Again, $1/\mu_s$ gives the mean free path between scattering events. The intensity of unscattered (or ballistic) light after passing through a non-absorbing medium can

be calculated by replacing μ_a with μ_s in Eq. 2.1.

In addition to the probabilistic treatment of the frequency of scattering events in bulk tissue, the distribution of scattering angles that a photon experiences at each scattering event is generalized. The probability that a photon will scatter into a unit solid angle oriented at a zenith angle θ relative to its original trajectory is governed by the phase function $p(\theta)$ of the scattering structure (Henyey and Greenstein, 1941). In tissue, the phase function is generalized as a single anisotropy factor, g, which is defined as the expectation value of the cosine of θ. The azimuthal angle Ψ, shown in Fig. 2·2, is randomly distributed between 0 and 2π. The anisotropy factor is mathematically expressed as:

$$g = \int_0^{\pi} p\left(\theta\right) \cos\theta 2\pi \sin\theta \, \mathrm{d}\theta, \tag{2.4}$$

and its possible values range from -1 to 1, representing complete backscattering and complete forward scattering, respectively. For normal optical wavelengths in tissue, g typically ranges from 0.75–0.99, with an average value of about 0.9 (Cheong et al., 1990; Jacques, 2013).

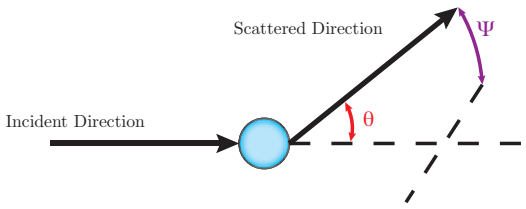

Figure 2·2: A schematic of a photon scattering from a particle with a zenith scattering angle θ and an azimuthal angle Ψ.

In diffuse optics applications such as AOI, μ_s and g are often combined into a

single parameter known as the reduced scattering coefficient:

$$\mu_s' = \mu_s (1 - g). \tag{2.5}$$

The purpose of μ_s' is to describe the diffusion of photons in a random walk of step size of $1/\mu_s'$ where each step involves isotropic scattering ($g = 0$). This is equivalent to the description of photon migration using many small steps of length $1/\mu_s$ with independent scattering angles, calculated based on the tissue's g, provided there are many scattering events before an absorption event ($\mu_s' \gg \mu_a$) (Graaff et al., 1993). This similarity relation has also been shown to extend to calculations of ultrasound induced phase modulations for the purposes of AOI (Sakadžić and Wang, 2002).

Unlike absorption, the wavelength dependence of μ_s' is not based on the chemical composition of the tissue. Instead, it is based solely on a relationship between the size of the tissue's scattering structures and the wavelength of the light, and it can normally be described by Mie theory (Bohren and Huffman, 2008) with a power law (Jacques, 1996):

$$\mu_s'(\lambda) = \mu_{s,0}' \left(\frac{\lambda}{\lambda_0} \right)^{-b}, \tag{2.6}$$

where $\mu_{s,0}'$ is the reduced scattering coefficient at λ_0 and b is a dimensionless parameter dependent upon the mean size of the scattering particles within the tissue. Wavelength dependent reduced scattering coefficients of selected tissues are shown in Fig. 2·3 where values for $\mu_{s,0}'$ and b are taken from Jacques (2013). It should be noted here that these values are approximate, especially in the case of brain tissue where different types of brain tissues exhibit drastically different optical properties.

2.1.3 Thermally Induced Changes

The application of heat to tissue – from HIFU or otherwise – can cause irreversible thermal damage leading to immediate cell death or a delayed secondary effect well

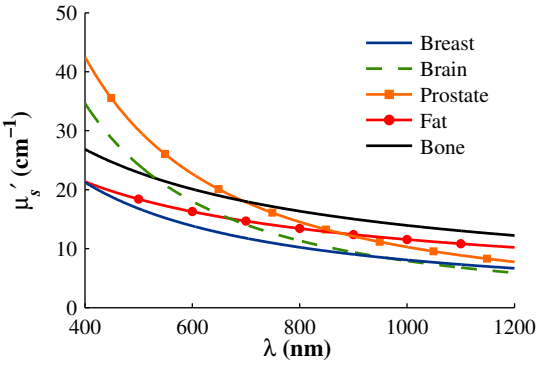

Figure 2·3: The approximate reduced scattering coefficient of breast, brain, prostate, fat, and bone calculated using Eq. 2.6 with values from Jacques (2013).

after the heating event. For the purposes of AO guidance of HIFU, we are interested in primary thermal injuries which produce immediately detectable structural and functional abnormalities in cells and tissues. In order (from low to high temperature), these primary thermal effects are the thermal dissociation (melting) of phospholipid cellular membranes, intracellular protein denaturation, and extracellular stromal protein denaturation (Thomsen and Pearce, 2011). It should be noted that at higher temperatures (approaching 100°C and up), water vaporization, tissue caramelization and carbonization, and tissue ablation will occur, but these temperatures are associated with boiling and cavitation which prevent the use of AO guidance, and are generally a sign of over treatment.

As cellular membranes melt, cell organelles collapse, and proteins denature, the optical properties of tissues change. Specifically, the chemical structure of chromophores change, while proteins are reduced from highly organized structures into small, amorphous granules, resulting in an increase in μ_s' and μ_a of the host tissue (Jacques and Gaeeni, 1989; Essenpreis, 1992; Çilesiz and Welch, 1993; Germer et al., 1998; Nilsson et al., 1998; Ritz et al., 2001; Yaroslavsky et al., 2002; Black and Barton, 2004; Ben-David et al., 2008). These optical changes are generally assumed to be linearly

proportional to the volume fraction of damaged cells within the tissue (Kim et al., 1996), and they have been shown to correlate well with the death of breast cancer cells (Nandlall et al., 2010).

The primary thermal mechanisms resulting in optical property changes are generally treated as first-order kinetic processes and have previously been modeled by the Arrhenius equation (Jacques et al., 1991; Yang et al., 1991; Agah et al., 1996; Skinner et al., 2000). Kinetic models for irreversible thermal damage in tissues employ a dimensionless thermal damage parameter, Ω, which represents the natural log of the ratio of the original concentration of undamaged cells, $c\,(0)$, to the remaining undamaged cells after heating, $c\,(t_f)$ (Pearce, 2009):

$$\Omega\,(t_f) \equiv \ln\left(\frac{c\,(0)}{c\,(t_f)}\right). \tag{2.7}$$

Given by the Arrenhius equation, Ω is described by:

$$\Omega\,(t_f) = \int_0^{t_f} A \exp\left(\frac{-E_a}{RT\,(t)}\right)\,\mathrm{d}t, \tag{2.8}$$

where the "pre-exponential factor" A is a measure of the effective collision frequency between reacting molecules in bimolecular reactions, E_a is an activation energy barrier, R is the gas constant, T is the temperature, and t_f is the heating time in seconds.

As discussed in Section 1.1.3, the primary thermal metric for predicting thermal damage during HIFU is thermal dose, as defined by Eq. 2.9:

$$t_{43} = \int_{t=0}^{t_{\text{final}}} R^{43-T(t)}\mathrm{d}t, \tag{2.9}$$

where $T(t)$ is temperature as a function of time and the "thermal damage isodose constant", R, is taken as 0.5 above 43°C and 0.25 below 43°C (Chung et al., 1999). The thermal dose model relates the exposure time at any temperature to an equivalent

exposure time at a reference temperature – here 43°C – in order to calculate the probability of tissue damage or death. Using this model, the surgeon employs an empirically-determined dose threshold, normally 240 min (Meshorer et al., 1983), to demarcate the lesion boundary as shown in Fig. 1·3. Therefore, for the purposes of HIFU it would be convenient if optical property changes could be expressed as a function of thermal dose rather than as an Arrhenius model. While the thermal dose model is mathematically closely related to Arrhenius models, a direct relationship between thermal dose and optical property changes has never been demonstrated. Given the measured thermal dose that a tissue has been exposed to, t_{43}, the thermal damage parameter can alternatively be expressed as:

$$\Omega\left(t_{43}\right) = \frac{t_{43}}{\tau_{43}}, \tag{2.10}$$

where τ_{43} (min) is the thermal damage time constant for heating at 43°C, defined as the time required for a healthy population of n cells to decline to a population of n/e. Using Eq. 2.10, the volume fraction of remaining undamaged cells after an exposure to a thermal dose of t_{43} can be calculated as:

$$\frac{c\left(t_{43}\right)}{c(0)} = \exp\left(-\frac{t_{43}}{\tau_{43}}\right). \tag{2.11}$$

Here it is assumed that optical properties are linearly proportional to the fraction of damaged cells, so that:

$$\mu = \mu_0 c_0 + \mu_d c_d, \tag{2.12}$$

where μ_0 and μ_d are the original and damaged values of the optical property, and c_0 and c_d are the concentrations of healthy and damaged cells. Therefore, a given optical property μ can be expressed as a function of the thermal dose to which it has

been exposed using:

$$\mu\left(t_{43}\right) = \mu_0 + \left(\Delta\mu\right)_{\max}\left(1 - \exp\left(-\frac{t_{43}}{\tau_{43}}\right)\right), \tag{2.13}$$

where $\left(\Delta\mu\right)_{\max} = \mu_d - \mu_0$ is the difference in the value of said optical property in damaged and healthy tissue.

Overall, little experimental data exists to describe the magnitude of thermally induced optical property changes, or to support the kinetics that theoretically govern them. In sections 2.2 and 2.3, the process of how optical properties are measured is described and in section 2.4 data is presented which describes thermal dose dependent optical property changes in chicken breast. However, in order to understand how optical property measurements are made, a general understanding of modeling light propagation in tissue is required. A brief introduction to this topic is presented in the following section.

2.2 Diffuse Light Transport and the Extraction of Optical Properties

2.2.1 The Forward Problem

Light propagation through any medium with known optical properties can be rigorously described using Maxwell's electromagnetic theory (Maxwell, 1865). However, the full solution for electromagnetic propagation in multiply scattering media is too complex for practical use. Alternatively, the multiple scattering problem can be simplified by ignoring the wave characteristics of light, such as polarization and interference, and instead focusing on the flow of energy through the medium (Ishimaru, 1978), essentially recasting the wave propagation problem as a much simpler radiative transport problem. In this case, the flow of optical energy through turbid media is

described by the radiative transfer equation (RTE):

$$\frac{1}{c}\frac{\partial L\left(\vec{r},\hat{s},t\right)}{\partial t} = -\hat{s}\cdot\nabla L\left(\vec{r},\hat{s},t\right) - \mu_t L\left(\vec{r},\hat{s},t\right) + \mu_s \int_{4\pi} L\left(\vec{r},\hat{s},t\right) p\left(\hat{s}'\cdot\hat{s}\right)\,\mathrm{d}\Omega' + S\left(\vec{r},\hat{s},t\right), \tag{2.14}$$

where c is the speed of light, $L\left(\vec{r},\hat{s},t\right)$ is the radiance[1] at the point r and time t flowing in direction $\hat{s}$, $\mu_t = \mu_a + \mu_s$ is the total attenuation coefficient, $p\left(\hat{s}'\cdot\hat{s}\right)$ is the scattering phase function, and $S\left(\vec{r},\hat{s},t\right)$ is the source term which describes injection of light into the point r at time t in direction $\hat{s}$. The RTE can be solved analytically by decomposing it into spherical harmonics and describing it as a diffusion equation (Farrell et al., 1992; Kienle and Patterson, 1997; Contini et al., 1997). However, approximations are required in order to derive the diffusion equation (such as an effective homogeneous medium), and the solution is limited to specific geometries. Moreover, the validity of the solution is restricted to conditions in which the observation point is more than one or two transport mean free paths[2] from a source, limiting the accuracy of the solution to distances greater than 1 or 2 mm from a source in typical tissues (Jacques and Pogue, 2008). Alternatively, the RTE may be solved with fewer limitations by using numerical approaches, such as the adding-doubling method (Prahl, 1995), or stochastic approaches such as the Monte Carlo method (Wang et al., 1995a). Overall, Monte Carlo methods offer the most accurate and most flexible solutions to the RTE – allowing for both time-dependent and steady-state calculations inside of optically inhomogeneous and arbitrarily complex media – but they are time consuming as many photons must be simulated to achieve accurate fluence distributions. The adding–doubling method is faster than Monte Carlo methods, but it is generally only appropriate for calculating total transmittance or reflectance from a tissue, and

[1] Radiance $\left(W/m^2\cdot sr\right)$ is a physical quantity that represents the intensity of light. It is defined as power per unit solid angle per unit projected area.

[2] The transport mean free path $l_t' = 1/(\mu_a + \mu_s')$.

it requires the medium to be approximated as a semi-infinite layer with homogeneous optical properties.

2.2.2 The Inverse Problem

In order to determine the optical properties of a material given the light distribution within it or, more commonly, at its boundaries, the RTE must be solved in an inverse manner. However, no direct inverse solution to the RTE exists. Instead, optical properties are usually obtained by repeatedly solving the RTE until the solution matches the measured light distributions. The most commonly employed approach for doing this is the inverse adding–doubling (IAD) method (Prahl et al., 1993). The IAD guesses the optical properties of the sample, then iteratively performs a numerical solution to the RTE using the adding–doubling method (Prahl, 1995) until the solution converges to measured values of reflection and transmission. Given measurements of total transmittance and total reflectance – normally made with a single or double integrating sphere setup (Pickering et al., 1993) – and collimated transmission, the IAD is able to obtain a unique solution for the material's μ_s, μ_a, and g coefficients. In many cases, collimated transmission measurements are unavailable as they are experimentally difficult to make. In these situations, the IAD uses an assumed value of g to calculate a unique solution for the material's μ_s' and μ_a coefficients.

The IAD is an accurate solution of the RTE for all optical properties, optical depths, and phase functions but a number of restrictions apply to the algorithm. Specifically, the light distribution is independent of time, samples have homogeneous optical properties, sample geometry is an infinite plane-parallel slab, boundaries are smooth, internal reflectance is governed by Fresnel's law, and polarization effects are ignored. Because of these restrictions, the IAD is limited to use with *ex vivo* tissues. Despite its constraints, the IAD has a number of positive features and open-source software is readily available to perform IAD calculations (Prahl, 2013). In addition

to being well supported and vigorously validated, the software is fast and accurate, it works for any combination of optical properties, it takes into account all of the interactions of a sample sandwiched between glass slides (which are used to ensure smooth boundaries), and it incorporates the effects of integrating spheres and light lost from the sides of samples during measurements.

2.3 Optical Property Measurement Materials and Methods

Now that theoretical models for photon migration in diffusive media have been presented and a method for extracting optical properties from experimental measurements has been established, experiments are presented which were performed to characterize optical property changes as a function of thermal damage. Excised tissues were heated, their bulk optical properties were inferred as a function of temperature history, and results were compared with the measured thermal dose in each sample.

2.3.1 Summary Overview

Experiments were performed to measure thermally induced optical property changes of *ex vivo* chicken breast tissues between 500–1100 nm (Adams et al., 2014). The objective of the experiments was to quantify the optical properties of undamaged and thermally necrosed tissues, and to examine the effectiveness of the thermal dose model in accurately predicting thermally induced optical property changes. The absorption coefficient, μ_a, and the reduced scattering coefficient, μ_s', of samples were measured as a function of thermal dose over the range 50-70°C. Additionally, the maximum observable changes in μ_a and μ_s' were measured as a function of temperature in the range 50-90°C. Results show that the standard thermal dose model used in the majority of HIFU treatments is insufficient for modeling thermally induced optical property changes. However, it was found by modifying the isodose constant it is possible to capture optical changes well. Additionally, results are presented that show

a temperature dependence on changes in the properties, with an apparent threshold effect occurring between 65–70°C.

2.3.2 Sample Preparation

All samples employed in this study were *ex vivo* chicken breast tissues purchased from a local store on the same day as the experiments. Chicken breast was chosen because of its apparently high optical contrast between normal and thermally damaged tissue, and its widespread use in HIFU and diffuse imaging studies (Pogue and Patterson, 2006). Moreover, characterizing the dynamics of thermally induced optical property changes of chicken breast allows the comparison of the modeling studies presented in Chapter 4 to the experimental AO guided HIFU data from Lai et al. (2011). Using a procedure similar to that employed by Çilesiz and Welch (1993), samples of approximately 2-mm thickness were cut with a handheld manual dermatome and then trimmed to approximately 25×50 mm. The 2-mm thickness was chosen to ensure an even and repeatable dermatome cut, and to allow a sufficient amount of light to transmit through the sample. The samples were moistened with saline, then mounted in holders constructed of two microscope slides, separated by 2-mm thick spacers and sealed with epoxy on each end. The saline also helped minimize the presence of air bubbles between the slides and the tissue. A schematic of a mounted sample is shown in Fig. 2·4.

2.3.3 Optical Measurements and Property Extractions

Integrating Sphere Measurements

Optical properties were determined from integrating sphere measurements of total reflectance and total transmittance made between 500–1100 nm, at 1 nm data intervals with a spectral bandwidth of 5 nm in the visible spectrum and 10-20 nm in the NIR, using a UV-Vis-NIR spectrophotometer (Cary 5000, Agilent, CA, USA) and

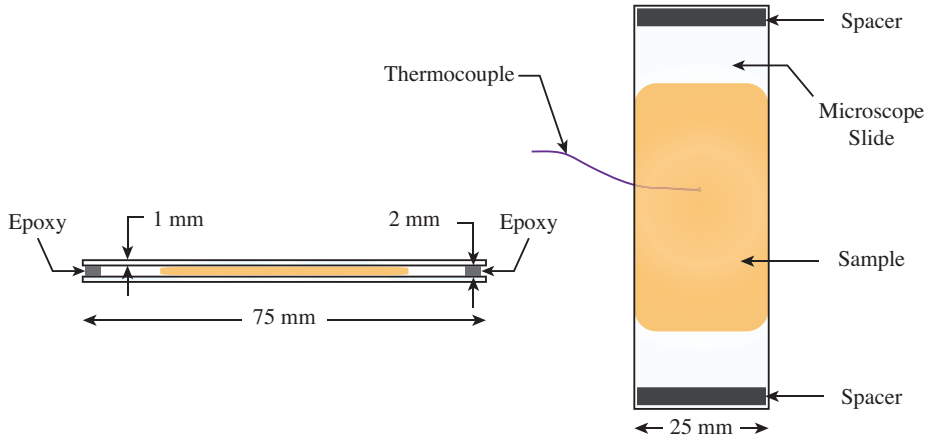

Figure 2·4: Side view (left) and top view (right) of the sample and holder geometry. Samples were mounted between two microscope slides, separated by 2-mm thick spacers. The holders were sealed with epoxy at each end. During saline bath exposures, a thermocouple was inserted into the tissue, slightly off center.

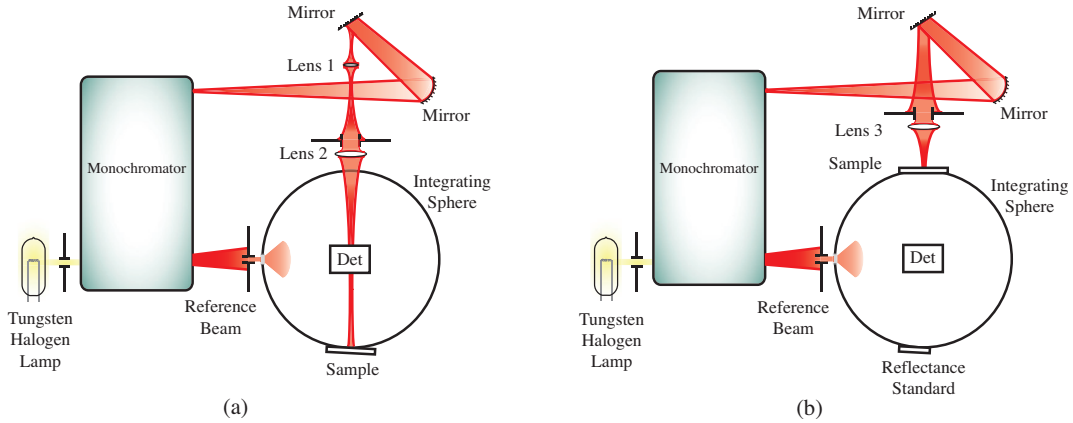

Figure 2·5: Schematic of the modified spectrophotometer and integrating sphere in reflectance (a) and transmittance (b) configurations. An f = 15 mm lens (Lens 1) and an f = 50 mm lens (Lens 2) were used to reduce the beam size at the reflection port, while an f = 35 mm lens (Lens 3) was used to reduce the beam size at the transmission port.

an internal Diffuse Reflectance Accessory (DRA) (DRA 2500, Agilent). The internal DRA was modified as shown in Fig. 2·5 in order to increase the port-to-beam-size ratio and prevent the overestimation of absorption due to light being lost through the sides of the sample (Torres et al., 1994). The DRA's lens system was removed, and a custom lens assembly was inserted which allowed for the use of different lenses for transmittance and reflectance measurements. In reflectance mode, a 15-mm and a 50-mm focal length lens were used to reduce the beam diameter to approximately 2 mm at the reflection port, while in transmittance mode a single 35 mm lens was used, resulting in a 2-mm diameter beam at the transmission port. The 50 mm and 35 mm lenses were fit with 10-mm diameter circular apertures to block stray light and to ensure that the beam was approximately circular. Custom mounts were also designed, constructed, and attached to the sides of the integrating sphere to allow for a repeatable placement of the sample holders and to ensure that the samples were held flush against the side of the sphere. Finally, the reference beam port was fit with a 2-mm diameter circular aperture to reduce its power to a similar level as the signal beam. Reducing the reference beam power lowered the required dynamic range of the detectors and allowed for more accurate measurements with higher SNR. These modifications are shown in Fig. 2·6.

The instrument was controlled and data was acquired using the Cary WinUV software (Agilent). The instrument settings were chosen to be a fixed bandwidth of 5 nm in the visible, a fixed source energy of 180 in the NIR, a full slit aperture, a grating changeover at 800 nm, and a detector changeover at 880 nm. During transmittance measurements, averaging times of 0.15 s/nm and 0.2 s/nm were used in the visible and the NIR, respectively, while averaging times of 0.2 s/nm and 0.4 s/nm were used for reflectance measurements. The spectral bandwidth and energy level were chosen to optimize the balance between the power of the light reaching the sample and the

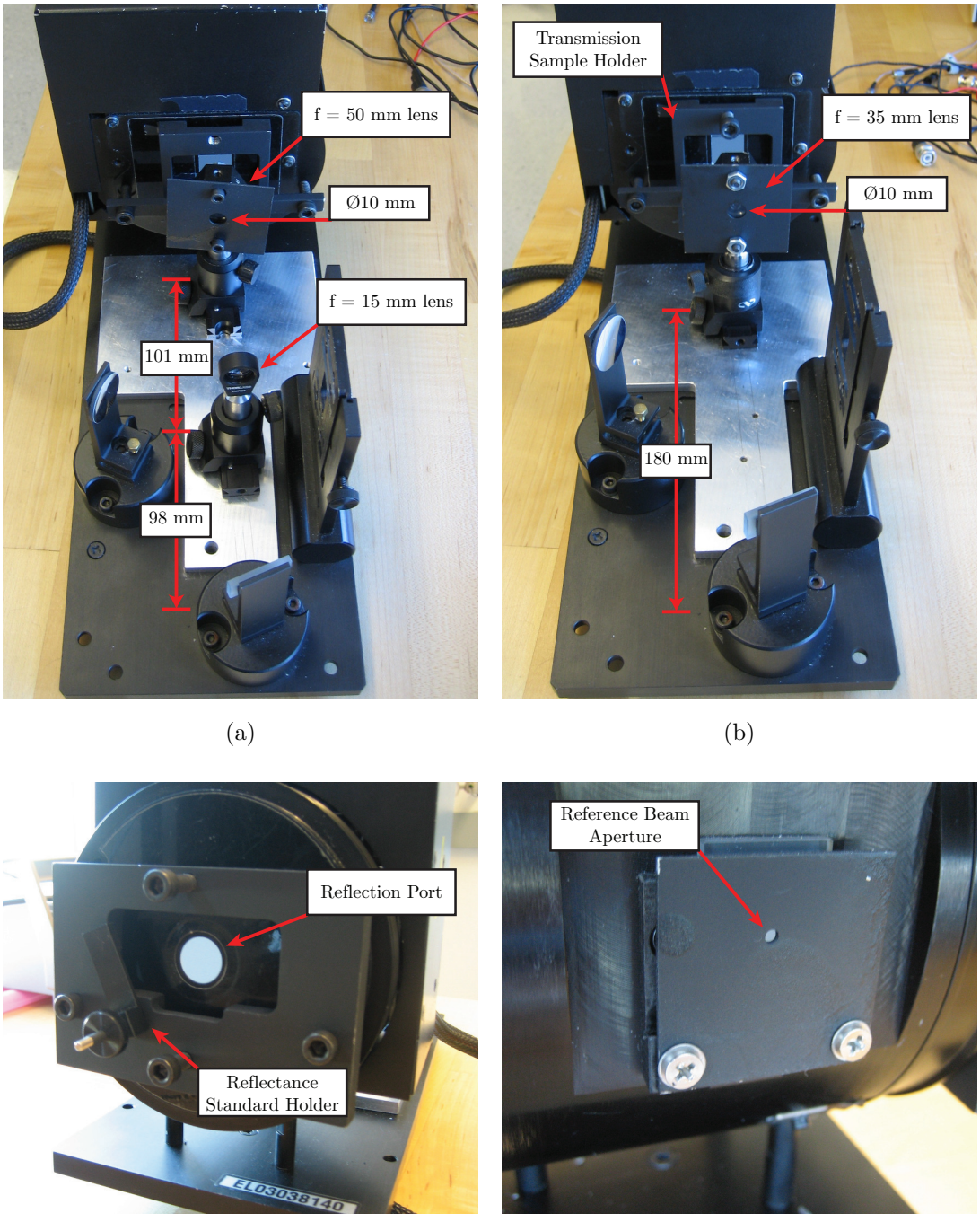

(a) (b)

(c) (d)

Figure 2·6: (a) Lens configuration for reflectance measurements. (b) Lens configuration for transmittance measurements. (c) The reflectance port and sample holder. (d) The reference beam aperture.

accuracy of the light's wavelength, and the averaging times were chosen to obtain reasonable SNR. Baseline transmission measurements were performed with an empty transmission port, while baseline reflectance measurements were made with a 99% reflectance standard supplied with the DRA.

IAD Calculations

The IAD algorithm was used to calculate μ_a and μ_s' from measurements of total transmittance, total reflectance, and the thickness of the samples. The software to perform the calculations was downloaded from the Oregon Medical Laser Center website (Prahl, 2013). For all measurements the refractive index of the microscope slides was assumed to be 1.52, the refractive index of the tissue was assumed to be 1.4, and the anisotropy factor of the tissue was assumed to be 0.97 (Sun and Wang, 2010). Preliminary collimated transmission measurements made at 633 nm and 1064 nm indicated that the anisotropy factor of the chicken breast did not change significantly after heating, but reliable measurements were not able to be performed for each sample due to the time required to acquire data with reasonable SNR. Therefore, it was assumed that the anisotropy factor of the chicken breast did not change significantly after heating, but small changes in g have little effect on computed values of μ_s'. All IAD calculations were performed using the dual beam spectrophotometer option. An example of a typical IAD input file and the command line syntax for executing the software are shown in Appendix A.

Validation

To validate the integrating sphere measurements and IAD calculations, the optical properties of three optical phantoms were measured. The 1.67-mm thick phantoms were composed of polystyrene spheres (0.746-μm diameter, Polysciences, PA, USA) suspended in water at three different particle number densities. Polystyrene spheres

are useful for building optical phantoms because their scattering properties are well described by Mie theory. Additionally, they are non-absorbing so the absorption properties of the phantom are dictated by the suspension medium. In this case, the absorption of the phantoms was that of water, but india ink or another absorber can be added if additional absorption is desired (Royston et al., 1996). The particle densities of the phantoms were determined by making collimated transmission measurements at 633 nm, where absorption due to water can be ignored, and calculating the extinction cross-section of the spheres using Mie theory. The scattering coefficient was then determined for each phantom based on its computed particle number density. The procedure used followed that of Royston et al. (1996).

Measurements of collimated transmission, τ_c, through a sample were made using the experimental setup shown in Fig. 2·7. Samples were illuminated with a 632.8 nm, 15 mW HeNe laser (05-LHP-991, Melles Griot, CA, USA) and the intensity of the unscattered light was detected with a Silicon photodetector (DET10A, Thorlabs, NJ, USA). When necessary, the power of the laser was adjusted with a calibrated and adjustable ND filter wheel (Thorlabs) in order to bring the measured intensity within the dynamic range of the detector. Signals were acquired using a data acquisition (DAQ) board (Compuscope 14200, 14-bit resolution, 200 MS/s, GaGe, IL, USA) and a computer using MATLAB (Mathworks, MA, USA). The sample was placed a large distance ($\sim$4 ft) from the detector in order to minimize the collection of scattered light.

The relationship between the collimated transmission coefficient, τ_c, and the particle number densities, N (particles/cm^3), of the phantoms can be expressed as:

$$\tau_c \equiv \frac{I_p}{I_0} = \exp\left(-N \cdot C_{\text{ext}} \cdot L\right), \tag{2.15}$$

where I_p is the unscattered intensity transmitted through the phantom, I_0 is the

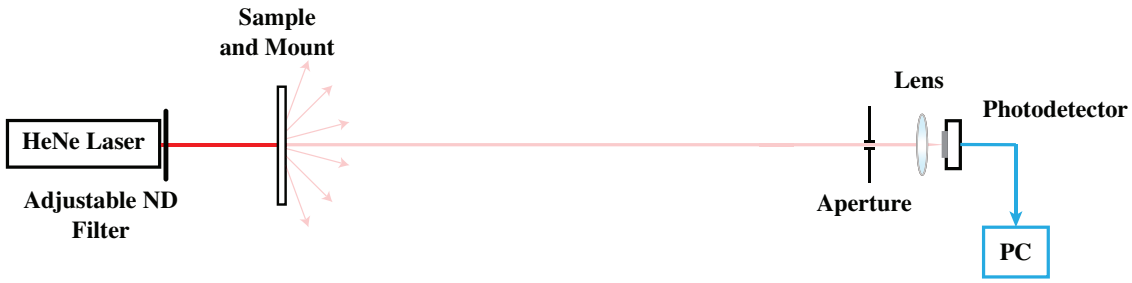

Figure 2·7: Setup used for measuring collimated transmission through a sample.

unscattered intensity transmitted through the sample holder when filled with water, L is the optical path length of the sample, and the extinction cross-section, C_{ext}, equals the scattering cross-section of the polystyrene sphere, C_{s}, because absorption is negligible. The scattering cross-section of each 0.746-μm diameter polystyrene sphere was found to be 0.69 μm^2 using a web-based Mie scattering calculator (Prahl, 2012b). The refractive index of the water was assumed to be 1.33, while the real refractive index of the polystyrene was assumed to be 1.583 and the imaginary refractive index was assumed to be 0 (Ma et al., 2003). The calculated particle number densities, volume concentrations, and μ_s at 633 nm of the three phantoms are shown in Table 2.1. The volume concentration was determined by multiplying N by the volume of one sphere and dividing by the total volume of the phantom. Given N, the scattering coefficient of the phantoms could be calculated at any wavelength as:

$$\mu_s(\lambda) = N \cdot C_{\text{s}}(\lambda), \tag{2.16}$$

where $C_{\text{s}}(\lambda)$ was again calculated with a Mie scattering calculator using wavelength dependent values for the refractive index of the spheres (Ma et al., 2003).

Once the optical properties of the phantoms were determined, total transmittance and reflectance were measured with the spectrophotometer and integrating sphere setup, and the measured optical properties were calculated using the IAD program.

Phantom Number	N (particles/cm^3)	Vc (%)	μ_s(633nm) (cm^{-1})
1	3.57×10^9	0.15	18.0
2	5.29×10^9	0.21	24.7
3	6.45×10^9	0.31	36.3

Table 2.1: The calculated particle number density N, the volume concentration Vc, and the scattering coefficient μ_s at 633 nm for each validation phantom.

For the phantoms, g was known at each wavelength from Mie calculations, so μ_s is measured instead of μ_s'. A comparison between predicted and measured scattering and absorption coefficients of the 0.21% concentration phantom are shown in Fig. 2·8. The agreement between predicted and measured values was better than 15% for all scattering measurements and better than 21% for all absorption measurements greater than 0.01 cm^{-1}. The agreement between predicted and measured values was equally good for the other two phantoms. It should be noted that when absorption is less than 0.05 cm^{-1}, the system predicts unrealistically low absorption coefficients, as shown in Fig. 2·8(b) at wavelengths smaller than 850 nm.

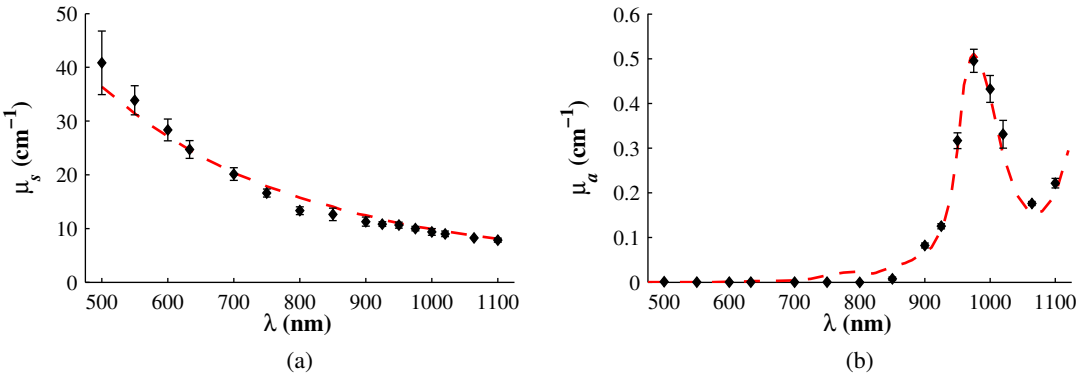

Figure 2·8: Validation of scattering (a) and absorption coefficient measurements (b) using a polystyrene sphere suspension (0.21% concentration). Data points are measured values, while the dashed lines represent values predicted by Mie theory and water absorption.

2.3.4 Thermal Damage Accumulation

Thermal damage was induced by exposing samples directly to a constant temperature bath (PSP-DX6, Cole-Parmer, IL, USA) filled with 0.1% phosphate buffered saline (Cole-Parmer). The temperature in the tissue was measured by means of an exposed junction wire thermocouple (250-μm tip diameter, Type E, Omega, Stamford, CT) that was inserted into each sample. The thermocouple was positioned at a distance approximately 5 mm from the center of the sample so that it did not interfere with the optical beam and affect the optical property measurements, but far enough from the edge of the tissue ($\sim$12 mm) that the temperature was an accurate measurement of the optical measurement region. To reduce noise from the thermocouple, its output was sampled via an 8-channel terminal block (TBX-1328, National Instruments, TX, USA) connected to an SCXI analog signal conditioner (SCXI-1120, National Instruments) which provided a 4 Hz low-pass filter, a 60 dB pre-amplifier, and an electronic cold junction compensation. The SCXI output was digitized by a DAQ board (AT-MIO-16E-1, 12-bit resolution, National Instruments) at 2 kHz and stored in computer memory using MATLAB. From the temperature measurements, the thermal dose was calculated five times per second using Eq. 2.9. During experiments, the isodose constant, R, was set to 0.25 below 43°C and 0.5 above 43°C. Preliminary studies showed that thermal dose was approximately uniform throughout the entire optical measurement region.

During experiments, measured optical properties, μ_a and μ_s', were fit as a function of measured thermal dose using:

$$\frac{\mu}{\mu_0} = 1 + \frac{(\Delta\mu)_{\max}}{\mu_0}\left(1 - \exp\left(-\frac{t_{43}}{\tau_{43}}\right)\right), \tag{2.17}$$

where the fitting parameters were τ_{43} and $(\Delta\mu)_{\max}/\mu_0$. Equation 2.17 is mathematically equivalent to Eq 2.13, but it is non-dimensionalized. Curve fitting was

accomplished by employing the trust-region-reflective algorithm for least squares of nonlinear parameters in the MATLAB curve fitting toolbox.

2.4 Measurements of Thermally Induced Optical Property Changes

2.4.1 Temperature Dependent Changes

As a tissue sample is exposed to a high and constant temperature, its optical properties initially change quickly, but then approach a steady-state condition. In the first set of experiments, samples were immersed in 50°C, 60°C, 70°C, 80°C, and 90°C saline baths – temperatures typically reached during HIFU exposures. The optical properties of five samples were measured at 1 – 20 minute intervals during exposure and steady state was defined as subsequent changes in less than 2%. Total immersion times varied from 5 – 200 minutes.

Figure 2·9(a) shows μ_s' as a function of wavelength, from 500–1100 nm, for the five temperatures. It can be seen that the reduced scattering coefficient decreases smoothly with wavelength and the data at 50°C and 60°C appear to cluster together, while the data at 70°C, 80°C, and 90°C also cluster together. In Fig. 2·9(b) the temperature dependence at two wavelengths, 550 nm and 975 nm – which correspond to peaks in the absorption spectra – also demonstrates a statistically significant (Student t-test, 95% confidence) jump in μ_s' between 60°C and 70°C. Both observations suggest that a threshold effect in the reduced scattering coefficient changes exists between 60°C and 70°C. Figure 2·10 shows the same data for μ_a. Here two peaks can be seen; one at 550 nm which is attributed to deoxyhaemoglobin and a second at 975 due to water. There is no evidence for a similar threshold for absorption.

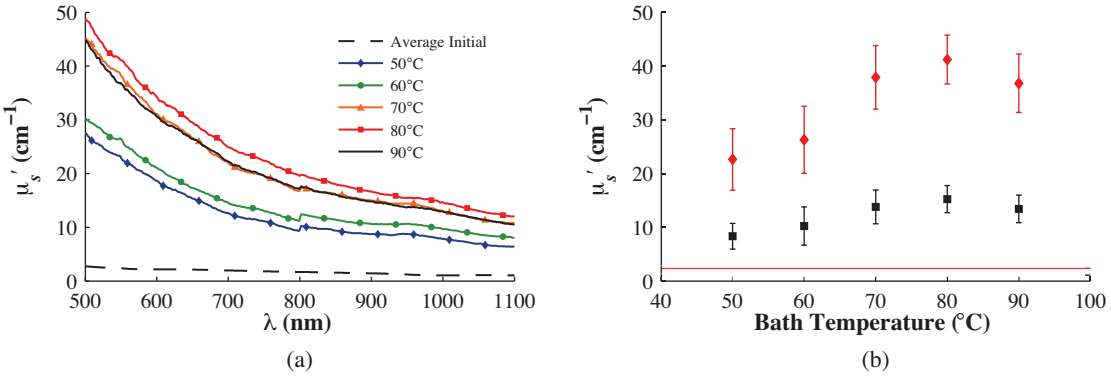

Figure 2·9: (a) Mean value of the steady state μ_s' of five samples as a function of temperature before (dashed line) and after bathing at 50°C (blue), 60°C (green), 70°C (orange), 80°C (red), and 90°C (black). Initial measurements (dashed line) were performed at room temperature. Although not apparent on this scale, initial measurements have a similar wavelength dependence to measurements after bathing. (b) Mean value of the steady state μ_s' of five samples measured at 550 nm (red diamonds) and 975 nm (black squares) with error bars representing one standard deviation. Solid lines represent average initial values; one standard deviation was represented with shading but cannot be seen on this scale.

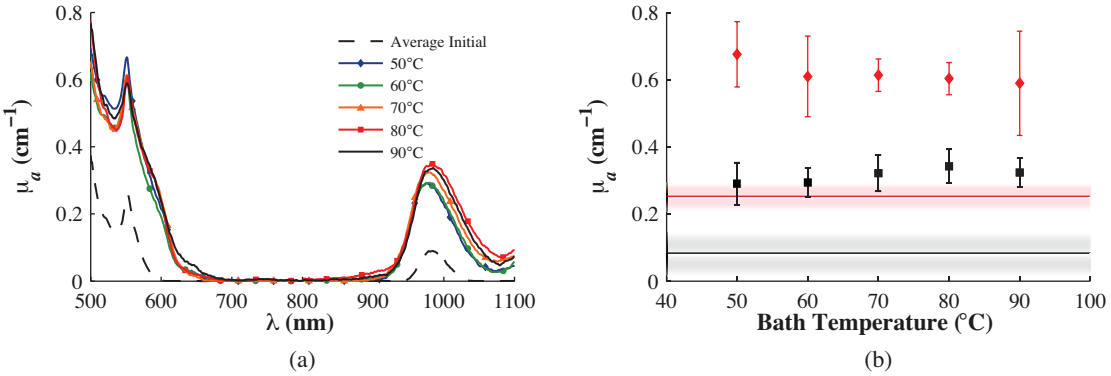

Figure 2·10: (a) Mean value of the steady state μ_a of five samples as a function of temperature before (dashed line) and after bathing at 50°C (blue), 60°C (green), 70°C (orange), 80°C (red), and 90°C (black). Initial measurements (dashed line) were performed at room temperature. (b) Mean value of the steady state μ_a of five samples measured at 550 nm (red diamonds) and 975 nm (black squares) where solid lines represent average initial values. Error bars and shading represent one standard deviation.

2.4.2 Thermal Dose Dependent Changes

In the second set of experiments, samples were immersed in saline at 50°C, 55°C, 60°C, and 70°C. Each sample had a thermocouple inserted into it so that $T(t)$ could be measured and thermal dose calculated. Optical properties were measured as a function of thermal dose. By using baths of different temperatures, the rate at which the dose is accumulated will vary as the heating rates are dependent on temperature difference. For tissue immersed at 50°C, the samples were removed from the saline bath at $t_{43} = 2500 \pm 5$ min increments, brought to room temperature, and the optical properties were measured. For 55°C the intervals were 1000 ± 9 min, at 60°C $(50 \pm 0.27) \times 10^3$ min, and at 70°C $(56.8 \pm 1.9) \times 10^3$ min. We note that samples immersed in the 50°C, 55°C, and 60°C saline all reached the bath temperatures over the range of dose reported here. However, samples in the 70°C bath only reached an average maximum temperature of 65°C as above this temperature the thermal dose accumulates very quickly.

Figures 2·11 and 2·12 show the changes in μ_s' and μ_a as a function of thermal dose. The data was fit according to Eq. 2.17, and the calculated fitting parameters for changes in μ_s' and μ_a are shown in Tables 2.2 and 2.3 respectively. Thermal changes in μ_s' are shown at the absorption peaks of 550 nm (deoxyhaemoglobin) and 975 nm (water). Only two wavelengths are shown due to the smooth nature of μ_s' as a function of wavelength. For absorption, which had a more complex spectra, data are also shown at 500 nm, where absorption is dominated by beta-carotene, and at 576 nm, where it is dominated by oxygenated haemoglobin (Prahl, 2012a).

The parameters in Table 2.2 show that the normalized change in the reduced scattering coefficient, $\Delta\mu_s'/\mu_{s_0}'$, was relatively independent of the bath temperature (9.6 at 550 nm and 7.6 at 975 nm). However, the time constant τ_{43} varied by a factor of 20 for the different bath temperatures. This indicates that the evolution of scattering

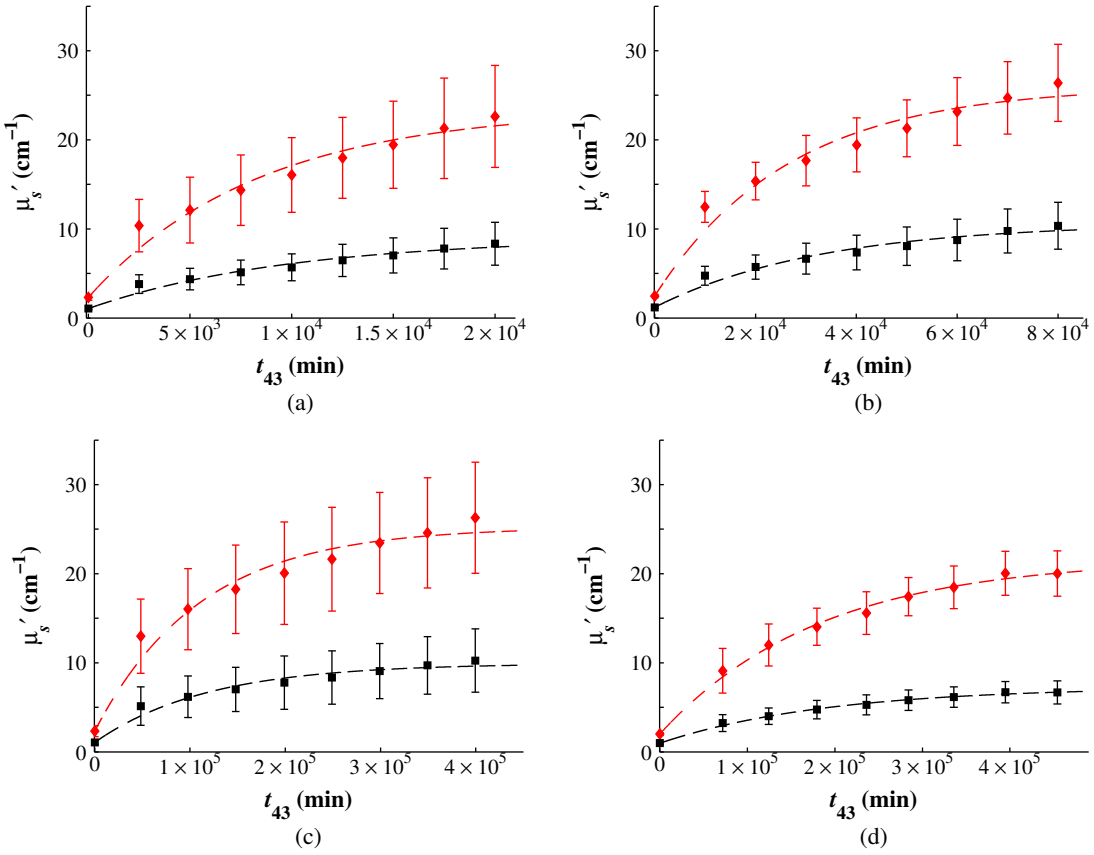

Figure 2·11: Scattering as a function of thermal dose accumulated while samples are immersed in 50°C (a), 55°C (b), 60°C (c) and 70°C (d) saline baths. Red diamonds represent μ_s' at 550 nm, and black squares represent μ_s' at 975 nm. Data points represent averages from five samples, with the error bars corresponding to one standard deviation. The dashed lines are best fits using the parameters in Table 2.2.

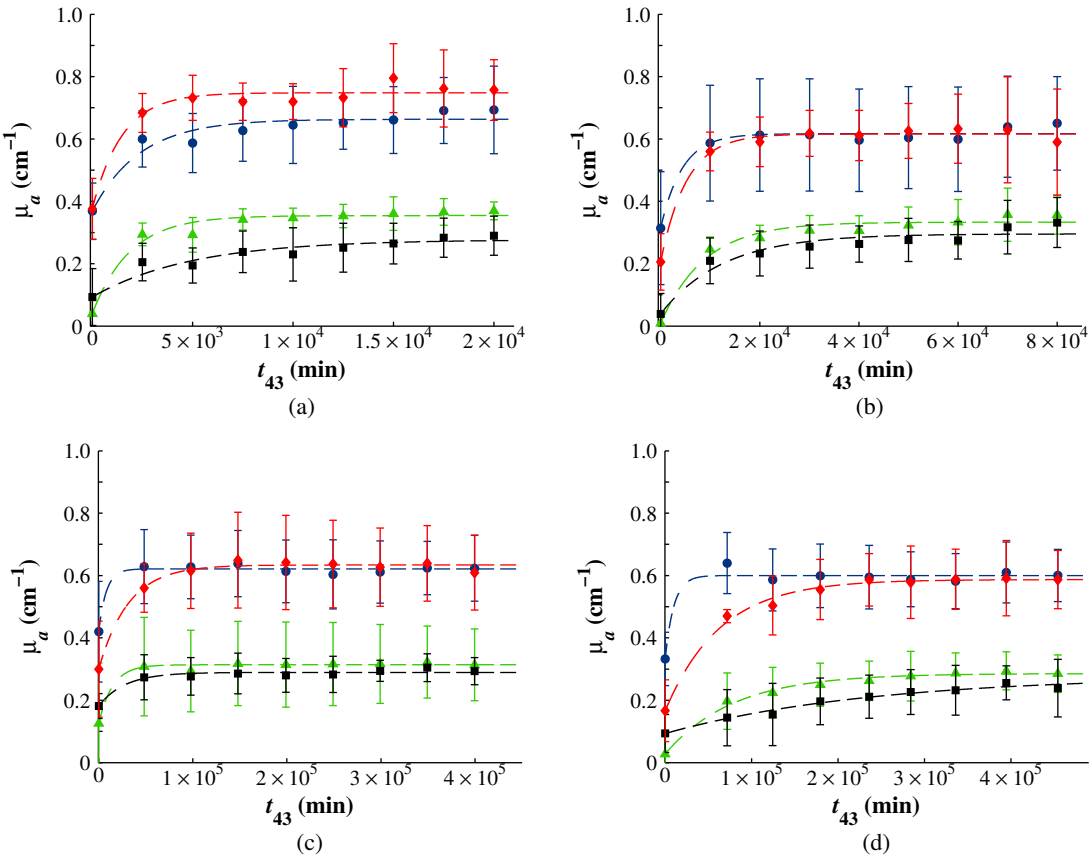

Figure 2·12: Absorption as a function of thermal dose accumulated while samples are immersed in 50°C (a), 55°C (b), 60°C (c) and 70°C (d) saline baths. Red diamonds represent μ_a at 500 nm, blue circles represent μ_a at 550 nm, green triangles represent μ_a at 576 nm, and black squares represent μ_a at 975 nm. Data points represent averages from five samples, with the error bars corresponding to one standard deviation. The dashed lines are best fits using the parameters in Table 2.3.

Saline Bath Temperature (°C)	550 nm		975 nm	
	τ_{43} (min$\times 10^3$)	$\Delta\mu'_s/\mu'_{s_0}$	τ_{43} (min$\times 10^3$)	$\Delta\mu'_s/\mu'_{s_0}$
50	8.35	9.21	9.94	7.59
55	26.7	9.60	33.0	7.93
60	111	9.84	118	8.44
70	183	9.84	191	6.48

Table 2.2: Parameters calculated from fitting equation 2.17 to the thermal dose dependent reduced scattering coefficient data measured at 550 and 975 nm, as shown in Fig. 2·11.

Saline Bath Temperature (°C)	τ_{43} (min$\times 10^3$)	$\Delta\mu_a/\mu'_{a_0}$	τ_{43} (min$\times 10^3$)	$\Delta\mu_a/\mu'_{a_0}$
	500 nm		550 nm	
50	2.38	0.800	1.49	0.991
55	4.35	0.967	5.23	2
60	7.97	0.479	31.6	1.11
70	9.99	0.804	63.5	2.53
	576 nm		975 nm	
50	1.88	7.94	1.98	4.96
55	8.92	36.8	12.7	6.58
60	1.47	1.49	2.79	0.595
70	79.0	9.29	238	1.98

Table 2.3: Parameters calculated from fitting equation 2.17 to the thermal dose dependent absorption coefficient data measured at 500, 550, 576 and 975 nm, as shown in Fig. 2·12.

was rate dependent – although the final value was relatively rate independent. This is because none of the samples reached the temperature threshold shown in Fig. 2·9. For the absorption parameters in Table 2.3, the variation in the parameters makes it difficult to come to similar conclusions.

2.5 Discussion

The results from this study demonstrate that the nominal parameters in the standard thermal dose model used for the majority of HIFU studies are insufficient to describe thermal changes in μ_s' and μ_a of *ex vivo* chicken breast between 500 and 1100 nm. This is perhaps not surprising as the coefficients were developed to describe cell death for relatively slow heating rates. As shown in Tables 2.2 and 2.3, the time constant τ_{43} is strongly dependent on the bath temperature employed in the experiment which suggests a dependence on the heating rate of the tissue. Additionally, the best fit values for τ_{43} are significantly different for scattering and absorption. The absorption coefficient reaches a steady state much more quickly than the reduced scattering coefficient.

Although the standard thermal dose model appears to be insufficient for describing thermal changes in μ_s' and μ_a, the isodose constant used to calculate the thermal dose can be adjusted to achieve a more consistent measurement of τ_{43} across the different bath temperatures. By varying R above 43°C and recalculating the thermal dose for every exposure, the least-squares error between the model and the measured data was found to occur when $R = 0.63$ above 43°C. Using this adjusted isodose constant, data was refit to Eq. 2.17. The values for τ_{43} are shown in Tables 2.4 and 2.5 for μ_s' and μ_a respectively. For μ_s', it can be seen that τ_{43} varies by less than 40% over the temperatures and wavelengths studied here, compared to a more than 20 fold variation seen in Table 2.2. For μ_a, the values of τ_{43} were not constant. However, the

Saline Bath Temperature (°C)	550 nm		975 nm	
	τ_{43} (min$\times 10^3$)	$\Delta\mu'_s/\mu'_{s_0}$	τ_{43} (min$\times 10^3$)	$\Delta\mu'_s/\mu'_{s_0}$
50	1.81	9.47	2.16	7.86
55	1.76	9.62	2.18	7.96
60	2.69	9.90	2.85	8.50
70	2.08	9.44	2.18	6.21

Table 2.4: Parameters calculated from refitting the thermal dose dependent μ'_s data using an adjusted isodose constant $R = 0.63$ above 43°C.

Saline Bath Temperature (°C)	τ_{43} (min$\times 10^3$)	$\Delta\mu_a/\mu'_{a_0}$	τ_{43} (min$\times 10^3$)	$\Delta\mu_a/\mu'_{a_0}$
	500 nm		550 nm	
50	0.537	0.806	0.331	0.993
55	0.289	0.967	0.348	2.00
60	0.050	0.479	0.770	1.12
70	0.030	0.804	0.632	2.49
	576 nm		975 nm	
50	0.421	7.97	0.101	2.02
55	0.594	36.8	0.843	6.59
60	0.366	1.49	0.693	0.596
70	0.809	9.09	2.75	1.89

Table 2.5: Parameters calculated from refitting the thermal dose dependent μ_a data using an adjusted isodose constant $R = 0.63$ above 43°C.

variation was still significantly less than the more than 100-fold variation seen in table 2.3. It should be noted that the time scales for changes in μ_a are an order of magnitude less than those for μ_s'. Although a detailed explanation eludes us, we speculate that absorption changes occur on a faster time-scale because they are dominated by the rupture of cell membranes and collapse of cell organelles, which are relatively low temperature effects and cause hyperchromasia in a pathology examination (Thomsen and Pearce, 2011). While the rupture of cell membranes and collapse of cell organelles also affect the scattering properties of a tissue, thermally induced changes in scattering are dominated by protein denaturation, which occurs at higher temperatures.

These data suggest that the thermal dose model can capture changes in optical properties, at least for scattering, but that the nominal parameters employed in the literature are not appropriate for the case studied here. Because R appears as the base in a power law expression which is then integrated, the thermal dose is very sensitive to the choice of R. We speculate that the choice of R is dependent, at the very least, on tissue type, rate of heating, and the property of interest. It is clear that more work needs to be done to determine R values appropriate to HIFU exposures.

In addition, the model for describing changes in μ_s' and μ_a will also depend on temperature. Looking at the steady state values of μ_s' as a function of bath temperature (Fig. 2·9), there appears to be a threshold effect somewhere between 60°C and 70°C. In Fig. 2·11, this threshold effect was not evident where the tissue reached an average maximum temperature of 65°C, and so we conclude that the threshold is in the range of 65–70°C. We hypothesize that this temperature threshold is related to the coagulation of one of the proteins present in the chicken breast. Nandlall et al. (2010) observed a similar threshold in polyacrylamide hydrogels containing bovine serum albumin (BSA) and attributed it to the aggregation of proteins due to the conversion of α-helices into intermolecular β-sheets. Similar temperature thresholds

have also been previously observed in myocardial and epidermis tissue (Jacques and Gaeeni, 1989; Thomsen et al., 1993). It should be noted that these temperature threshold effects were not present in the data for μ_a. Additionally, we note that the mean μ_s' at 90°C appears lower than that at 80°C, but there is no statistically significant difference. We expect that this is due to sample-to-sample variation, however it's possible that this is a real effect as a similar trend was reported by Jacques and Gaeeni (1989).

Overall, changes in μ_s' are significantly more marked and more consistent than changes in μ_a. This reveals that changes in scattering are more sensitive than changes in absorption to thermally induced effects, and so scattering may be a better property for monitoring thermal therapies. Additionally, since changes in μ_s' occur over a longer thermal dose scale and exhibit certain threshold effects, they are easier to monitor and to relate to biologically relevant events. However, this study was unable to identify any consistent differences between thermal changes in different tissue chromophores, which may provide important information for monitoring thermal therapies *in vivo*.

2.6 Summary

In this chapter the fundamental concepts of light-tissue interactions were presented, the optical properties used to characterize them were defined, and thermally dependent changes in optical properties were introduced. The basics of diffuse light transport, and methods to extract optical properties from experimental measurements were described. Experiments which were performed to measure thermally induced changes in the optical properties of *ex vivo* chicken breast over wavelengths from 500 nm to 1100 nm were presented. Results showed that the nominal parameters in the standard thermal dose model do not describe the changes in optical properties, but by changing the isodose constant and including a temperature threshold, it is possible to

develop a reasonable model. The data suggest that the optical scattering coefficient is more sensitive to thermal effects than optical absorption. In the Chapter 3, a model which makes use of these experimental results will be presented to describe the AO guidance of HIFU.

Chapter 3

Modeling Theory and Methodology

In accordance with the specific aims presented in Chapter 1, much of the work reported in this thesis was dedicated to developing a comprehensive model to describe the AO guidance of HIFU. Developing such a model requires simulating many physical processes, including calculations of: acoustic pressure and intensity, temperature changes due to the interaction of ultrasound with tissue, thermally induced optical property changes, light propagation in tissue, ultrasound induced phase modulations of diffuse light, and finally AO signal detection. Each of these sub-models must fit together into a single multi-physics AO guided HIFU model, as shown in Fig. 3·1. This chapter presents the theory relevant to each component of the model, describes the computational methods that have been employed, and discusses the implementation of the model. All of the code discussed in this section can be found on the Boston University Digital Common Library (Adams, 2014).

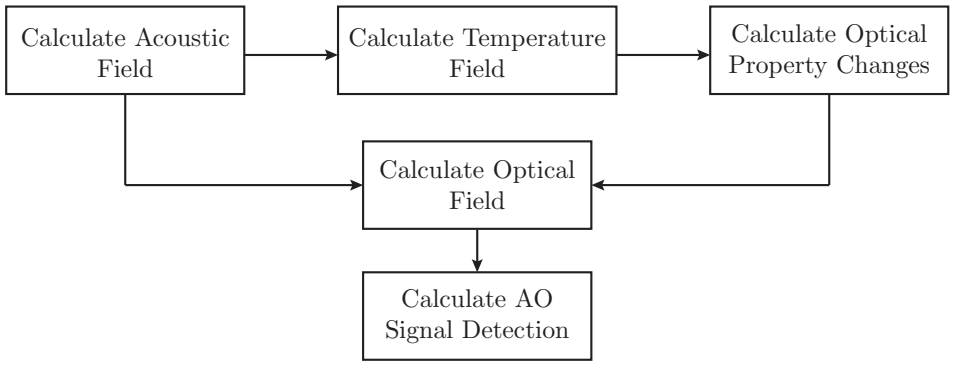

Figure 3·1: The workflow of the full AO guided HIFU model.

3.1 The Acoustic Field

3.1.1 Angular Spectrum Theory

In order to calculate ultrasound induced tissue heating and diffuse light modulations, an accurate representation of the HIFU source's acoustic field is required. In this work, acoustic pressure, particle velocity, and intensity were calculated in three-dimensions using the angular spectrum method (Stepanishen and Benjamin, 1982; Goodman, 2005). The angular spectrum method is a convenient, accurate, and computationally efficient model for predicting diffractive wave propagation from a single plane into any other parallel plane. The method expands an arbitrarily complex wave front into a series of plane waves, propagates each plane wave individually to a parallel plane, and then uses an inverse Fourier transform to revert the waves back to a complex wave front. Although the angular spectrum solution has many positive features, the form implemented in this work is restricted to a linear solution of the wave equation. Because it is a linear model, it is not suitable for very high pressures. However, in the range of pressures that are suitable for the AO guidance of non-cavitating HIFU lesion formation, nonlinear effects are assumed to be small and are thus ignored. The basics of the angular spectrum technique will be presented here in the form they were implemented, and the reader is referred to Goodman (2005) for further details.

Let the pressure $p(x, y, z, t)$ be a monochromatic time harmonic wave with a temporal behavior of $e^{-i\omega_a t}$, where ω_a is the wave's angular frequency. The source is assumed to be positioned at $z = 0$ and directed along the $+z$ axis. The pressure in the source plane can be described in the frequency domain by applying a Fourier Transform, which will be defined here as:

$$P(x, y, \omega_a) = \int_{-\infty}^{\infty} p(x, y, t) \mathrm{e}^{i\omega_a t} \, \mathrm{d}t. \tag{3.1}$$

$\mathscr{F}$ and $\mathscr{F}^{-1}$ will be used to indicate forward and inverse transforms respectively. Given $P(x, y, \omega_a)$ at the source plane, the angular spectrum of the source plane is defined as its two-dimensional spatial Fourier Transform with respect to x and y:

$$\tilde{P}(k_x, k_y, \omega_a) = \int_{-\infty}^{\infty}\int_{-\infty}^{\infty} P(x, y, \omega_a) \mathrm{e}^{i(k_x x + k_y y)} \,\mathrm{d}x \,\mathrm{d}y. \tag{3.2}$$

By solving the two-dimensional spatial Fourier Transform of the Helmholtz equation, it can be shown that the solution for the angular spectrum $\tilde{P}(k_x, k_y, z, \omega_a)$ at any plane z is given by:

$$\tilde{P}(k_x, k_y, z, \omega_a) = \tilde{P}(k_x, k_y, \omega_a) \mathrm{e}^{i(k_z z - \omega_a t)}, \tag{3.3}$$

where $k_z = \sqrt{k^2 - k_x^2 - k_y^2}$ is the z component of the wave vector and $k = \frac{\omega_a}{c_0} + i\alpha(\omega_a)$, where c_0 is the speed of sound in the medium and α_a is the acoustic attenuation coefficient of the medium. Given this solution, one can employ an inverse Fourier Transform to find the pressure field in x and y at any z location.

Given a pressure field obtained using the angular spectrum method, the particle velocity and the time averaged intensity fields can be solved for in the following manner (Blackstock, 2000). First, the particle velocity field $U(x, y, z, \omega_a)$ can be calculated from the pressure field using:

$$U(x, y, z, \omega_a) = -\frac{\nabla P}{i\omega_a \rho_0}, \tag{3.4}$$

where ρ_0 is the density of the medium. Then, using the time varying pressure and particle velocity fields, the time averaged intensity field is calculated as:

$$I_{\mathrm{av}}(x, y, z) = \frac{1}{2} \mathrm{Re}(pu^*), \tag{3.5}$$

where * denotes a complex conjugate. This approach yields an accurate solution of

the intensity and does not rely on a plane-wave assumption which overestimates the intensity of the HIFU source. It also yields the directional vector of the particle velocity field, $\hat{u}(x, y, z, t)$, which is later used for AO calculations.

3.1.2 Numerical Implementation

An angular spectrum solution for the pressure and intensity fields produced by a single element, spherically-focused HIFU source with a 70-mm aperture, a 20-mm diameter central hole, and a 62.4-mm focal length at its 1.1 MHz central frequency (model H-102, Sonic Concepts, WA) was implemented in MATLAB. An initial pressure source condition of $p_0 = 1$ at the face of the transducer was used. In order to specify the source condition of the focused source in a single plane, it was defined at the mouth plane of the transducer in k-space as (Wu and Stepinski, 1999):

$$\tilde{P}(k_x, k_y) = \mathscr{F}\left(P(x, y)\mathrm{e}^{ikdr}\right)\frac{k}{k_z}, \tag{3.6}$$

where dr is the distance between the face of the transducer and the mouth plane along the line of focus. The hole in the center of the H-102 transducer was accounted for by employing Babinet's principle and subtracting the solution for a transducer of the same size and curvature as the hole (Jiménez and Hita, 2001).

For all of the simulations performed in this work, a grid spacing of 100 μm was used and the calculation domain was extended to 5 times the radius of the source in x and y. The calculation domain was large in order to minimize the effect of mirror sources in the angular spectrum solution. The 100-μm grid spacing is smaller than what is required to obtain an accurate solution, but it was chosen to be compatible with the fine grid spacing required for the AO Monte Carlo simulations described in Section 3.5. In all of the simulations performed for this work, the source was placed in water and propagation was considered from water into tissue. In order to account

for the boundary between water and tissue, a pressure transmission coefficient was calculated as:

$$T = \frac{2Z_{0,t}}{Z_{0,t} + Z_{0,w}} \tag{3.7}$$

where $Z_{0,t}$ and $Z_{0,w}$ are the specific acoustic impedances of the tissue and the water respectively. Angular transmissive and refractive effects were assumed to be negligible. For propagation from water into chicken breast, this resulted in an error of $< 1\%$ in the worst case scenario.

3.1.3 Validation

In order to validate the angular spectrum code, the axial and radial pressure distributions were compared to an analytical solution of the Rayleigh integral for a focused transducer whose radius is large compared to the depth of its concave surface and the acoustic wavelength (O'Neil, 1949). Again, the hole in the center of the transducer was accounted for by employing Babinet's principle. A comparison between the analytic solution and the angular spectrum solution for the axial and radial pressure amplitude distributions in water from the H-102 source is shown in Fig. 3·2(a) and (b) respectively. Figure 3·2(c) and (d) show the axial-plane distributions of the pressure and the intensity fields. The radial distance is defined as the transverse distance from the focus in the focal-plane of the transducer, and the axial distance is defined as the distance measured from the face of the center of the transducer. The pressure fields are normalized to the source pressure, and the intensity values shown are for a source pressure of 1 Pa. The acoustic properties used in this simulation are summarized in Table 3.1.

The angular spectrum solution is most accurate in the focal region of the transducer, achieving a maximum error of $\sim$1.5% and a root-mean-square error $\ll$1% within the full-width half maximum (FWHM) of the focus. Discrepancies are ob-

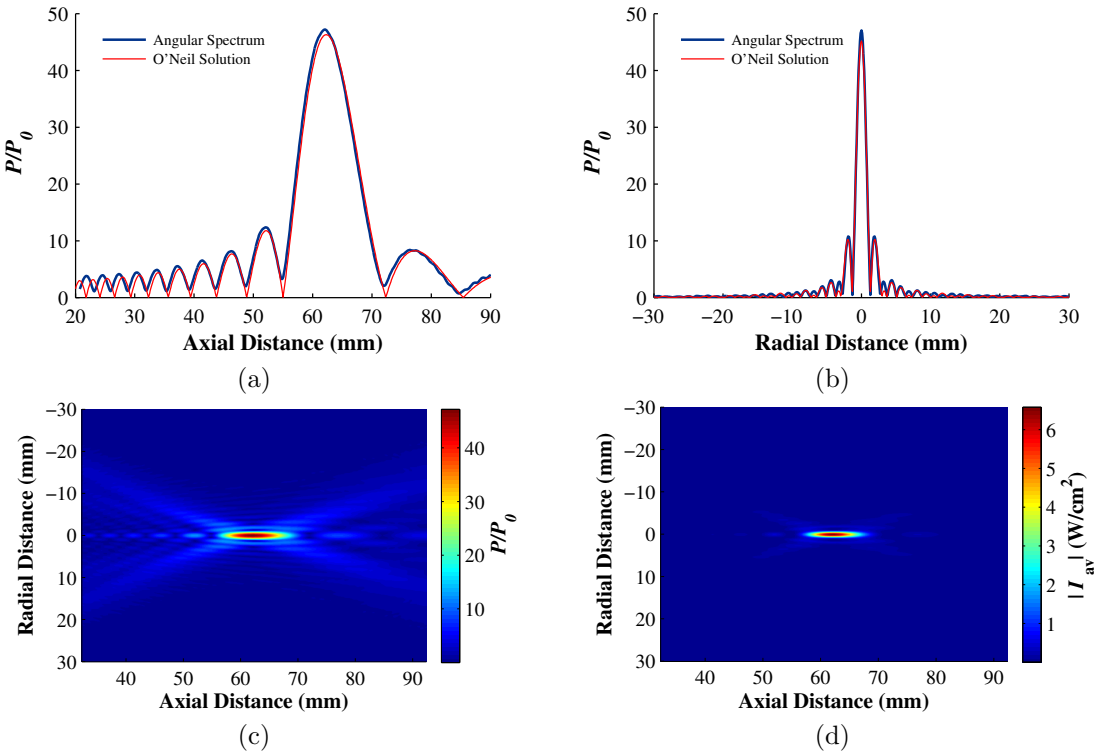

Figure 3·2: The axial (a) and radial (b) pressure amplitude distributions for an H-102 transducer in water calculated using the angular spectrum code and O'Neil's analytical solutions. The radial distribution is at the focal plane of the source. (c) The axial-plane pressure distribution calculated with the angular spectrum code. (d) The axial-plane intensity distribution calculated with the angular spectrum code for a source pressure of 1 Pa.

Property	Value
ρ_0 (kg/m^3)	998
c_a (m/s)	1481
α (Np/m·MHz)	0.025

Table 3.1: The acoustic properties of water used in the angular spectrum simulation. ρ_0 is the equilibrium density, c_a is the speed of sound, and α is the attenuation coefficient.

served in the structure of the axial pressure fluctuations in the pre-focal region (particularly very close to the transducer face) and the second radial side lobes in the focal plane. Additionally, ripples caused by mirror sources in the angular spectrum solution are observed in the far field. As previously mentioned, the 100-μm grid spacing used here is smaller than what is required to obtain an accurate solution. The axial and radial root-mean-square errors between the angular spectrum solution and the analytical solution are shown as a function of grid spacing in Fig. 3·3, where the error is represented as a percentage of the focal pressure. Although the grid spacing doesn't have a major impact on the accuracy of the pressure solution, a large grid spacing has a large effect on the accuracy of the numerical gradient performed in Eq. 3.4, and thus a large effect on the calculated velocity and intensity fields.

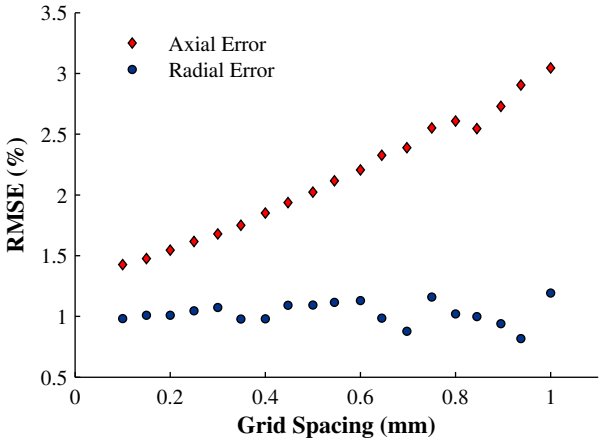

Figure 3·3: The root-mean-square error of the angular spectrum solution with respect to the analytical solution for the axial and radial pressure amplitude distributions. The error was calculated within ±30 mm of the focus and is plotted as a percentage of the focal pressure amplitude.

3.2 The Temperature Field

3.2.1 Tissue Heating Theory

For the purposes of modeling AO guided HIFU, we are interested in how energy from the HIFU source is absorbed into tissue and converted to heat, and how the heat conducts through the tissue. The methods employed for this work are described in this section, but the reader is referred to Edson (2001) and Yang (2003) for more complete reviews of models used to calculate temperature rises due to the absorption of ultrasound.

The absorption of ultrasound as it propagates through tissue results in heat transfer to the tissue. For a plane time harmonic wave, the ultrasonic power deposition per unit volume is (Pierce, 1989):

$$q_{\mathrm{HIFU}} = 2\alpha_a |I_{\mathrm{av}}|, \tag{3.8}$$

where I_{av} is the time averaged intensity vector and α_a is the acoustic absorption coefficient. Given the heat deposited into the tissue by the HIFU field, the temperature field, T, can be calculated using Pennes bioheat transfer equation (Pennes, 1948), with q_{HIFU} incorporated into the equation as an extra heat source term (ter Haar, 2004):

$$\rho_t C_t \frac{\partial T}{\partial t} = K_t \nabla^2 T - W_b C_b \left(T - T_b\right) + q_m + 2\alpha_a |I_{\mathrm{av}}|. \tag{3.9}$$

Here, ρ_t, C_t, and K_t are the equilibrium density, heat capacity, and thermal conductivity of the tissue respectively. The second term on the right hand side of Eq. 3.9 is the perfusion cooling term, where W_b, C_b, and T_b are the blood perfusion coefficient, heat capacity, and ambient temperature of the blood respectively. The third term on the right hand side is a source term to account for heat generated during metabolic processes in the body, represented by the power density of metabolic heat generation,

q_m. The Pennes model provides an accurate and flexible three-dimensional solution to the temperature field given the time averaged acoustic intensity field (Eq. 3.5), however it is computationally intensive to solve.

3.2.2 Numerical Implementation

The temperature field was determined by solving the bioheat transfer equation using a three-dimensional finite-difference time-domain (FDTD) method implemented in MATLAB. The FDTD approach allows a partial differential equation to be solved using discrete time steps over a discrete spatial grid. Equation 3.9 is discretized to second order-accuracy in space and time using Eqs. 3.10, where (i, j, k) refers to the voxel position. Δx, Δy, Δz are the spatial grid spacings, and n refers to a time step of duration Δt.

$$\begin{aligned}
\frac{\partial^2 T}{\partial x^2} &= \frac{1}{\Delta x^2}\left(T_{i+1,j,k} - 2T_{i,j,k} + T_{i-1,j,k}\right), \\
\frac{\partial^2 T}{\partial y^2} &= \frac{1}{\Delta y^2}\left(T_{i,j+1,k} - 2T_{i,j,k} + T_{i,j-1,k}\right), \\
\frac{\partial^2 T}{\partial z^2} &= \frac{1}{\Delta z^2}\left(T_{i,j,k+1} - 2T_{i,j,k} + T_{i,j,k-1}\right), \\
\frac{\partial T}{\partial t} &= \frac{T_{n+1} - T_n}{\Delta t}.
\end{aligned} \tag{3.10}$$

Once discretized, Eq. 3.9 was solved using an alternating direction modification to the Crank–Nicolson method (Ames, 1992). T_{n+1} was solved for in three steps. First, the x derivative was evaluated at $n + \frac{1}{2}$, and a first approximation T^*_{n+1} was obtained using the first step of Eq. 3.11. Next, the evaluation of the y derivative was moved ahead by means of the second step of Eq. 3.11 and a second approximation T^{**}_{n+1} was obtained. Finally, the z derivative was moved ahead using the third step of Eq. 3.11 to obtain the true value of T_{n+1}. This approach yields a solution which is locally second-order correct in space and time and which is unconditionally stable,

regardless of the spatial or temporal grid spacing. The equations are shown below, where the entire right hand side of Eq. 3.9 is given as a net source term, q_{net}, and the spatial derivatives are written in their continuous form to save space.

$$\begin{aligned}
\rho_t C_t \frac{T^*_{n+1} - T_n}{\Delta t} &= K_t \left(\frac{1}{2} \frac{\partial^2 \left(T^*_{n+1} + T_n \right)}{\partial x^2} + \frac{\partial^2 T_n}{\partial y^2} + \frac{\partial^2 T_n}{\partial z^2} \right) + q_{\text{net}} \\
\rho_t C_t \frac{T^{**}_{n+1} - T_n}{\Delta t} &= K_t \left(\frac{1}{2} \frac{\partial^2 \left(T^*_{n+1} + T_n \right)}{\partial x^2} + \frac{1}{2} \frac{\partial^2 \left(T^{**}_{n+1} + T_n \right)}{\partial y^2} + \frac{\partial^2 T_n}{\partial z^2} \right) + q_{\text{net}} \\
\rho_t C_t \frac{T_{n+1} - T_n}{\Delta t} &= K_t \left(\frac{1}{2} \frac{\partial^2 \left(T^*_{n+1} + T_n \right)}{\partial x^2} + \frac{1}{2} \frac{\partial^2 \left(T^{**}_{n+1} + T_n \right)}{\partial y^2} + \frac{1}{2} \frac{\partial^2 \left(T_{n+1} + T_n \right)}{\partial z^2} \right) + q_{\text{net}}
\end{aligned} \tag{3.11}$$

For all of the thermal simulations performed in this work, a grid spacing of 100 μm and a time step of 100 ms were used. In order to improve the code's computational efficiency within the MATLAB environment, the solution utilized matrix operations. Although this solution was shown to improve computational times, it restricted the geometry of the simulation volume to a cube. A cubic tissue volume was sufficient for the studies performed in this work, but the solution can be modified to a set of parallelized loops in order to accommodate an arbitrarily shaped geometry if necessary. The 100-μm grid spacing iss again smaller than what is required to obtain an accurate solution, but it was chosen to be compatible with the fine grid spacing required for the AO Monte Carlo simulations.

Most of the simulations performed in this work were chosen to mimic the experimental conditions presented in Lai et al. (2011), where the tissue was *ex vivo*. Thus, the source and sink terms due to metabolic heat generation and blood perfusion were set to zero. As an initial condition, the temperature within the tissue was set to 21 °C – the average temperature of the water during experiments. An insulating boundary condition was chosen as the simulated tissue was typically surrounded by a plastic

holder, but the boundary conditions have little impact on the solution due to the sharp thermal gradients present during HIFU.

3.2.3 Validation

The bioheat transfer equation code was validated by comparison to an analytical solution of the focal temperature rise caused by a heat source extending infinitely along the z axis with a Gaussian radial profile (Parker, 1983, 1985). To create the source, the intensity distribution of the HIFU source was calculated for a target peak focal pressure of 6 MPa using the angular spectrum code described in Section 3.1, with propagation from water into a 40-mm thick chicken breast. As with all of the acoustic solutions in this work, nonlinear effects were ignored. For all of the peak pressures stated throughout this work, a "target" peak pressure refers to the peak focal pressure calibrated in water (the actual peak pressure may be lower inside of the tissue due to attenuation). Next, a gaussian curve in the form of Eq. 3.12 was fit to the radial intensity distribution of the HIFU source using the MATLAB curve-fitting toolbox.

$$I\left(r\right) = I_0 \exp(-r^2/\beta), \tag{3.12}$$

where I_0 and β are the fitting coefficients. The analytic solution to the focal temperature for a source of this form is given by (Parker, 1985):

$$T\left(t\right) = \frac{2\alpha_a I_0}{\rho_0 c_v}\left(\frac{\beta}{4\kappa}\right)\ln\left(1+\frac{4\kappa t}{\beta}\right), \tag{3.13}$$

where $\kappa = K/\rho_0 c_v$ is the thermal diffusivity of the medium.

While calculating the temperature rise with the bioheat transfer code, metabolic heat generation and cooling due to perfusion were not considered. The acoustic properties of water are given above in Table 3.1, while the acoustic and thermal properties of chicken breast that were used are summarized in Table 3.2. The root-mean-square

error between the focal temperature rise calculated by the bioheat transfer equation code and the Parker analytical solution are shown for a 60 s heating time as a function of grid spacing and time step in Fig. 3·4(a) and (b) respectively. Figure 3·4(c) shows the calculated focal temperature rises as a function of time for a grid spacing of 100 μm and a time step of 100 ms, and (d) shows the error between the two solutions. As shown in Fig. 3·4(a) and (b), the grid spacing has a large effect on the accuracy of the solution, but the time step has almost no effect. As shown in Fig 3·4(c), the bioheat transfer equation code over-predicts the focal temperature rise by $\sim$1.2 °C for a heating time of 60 s. This is an acceptable amount of error considering the long heating time and the large temperature focal temperature rise calculated. As shown in Fig 3·4(d), the relative error asymptotes around 1.5%, so the absolute error is smaller when the temperatures are lower.

Property	Value	Property	Value
c_a (m/s)	1585	ρ_t (kg/m^3)	1040
α (Np/m·MHz)	$0.5 f_0^{1.1}$	α_a (Np/m)	0.78α
C_t (J/kg·C)	3210	K_t (W/m·C)	0.4683

Table 3.2: The acoustic and thermal properties of chicken breast used in all of the angular spectrum and bioheat transfer simulations. c_a is the speed of sound, ρ_t is the equilibrium density, α is the attenuation coefficient, α_a is the absorption coefficient, C_t is the specific heat, and K_t is the thermal conductivity. Acoustic properties were taken from (Draudt, 2012) and thermal properties were taken from (Huang and Liu, 2009).

3.3 Thermally Induced Optical Property Changes

The theory relevant to thermally induced optical property changes is detailed in Chapter 2, therefore only the numerical implementation will be discussed here. It is worth noting that we assume that optical property changes are induced only by

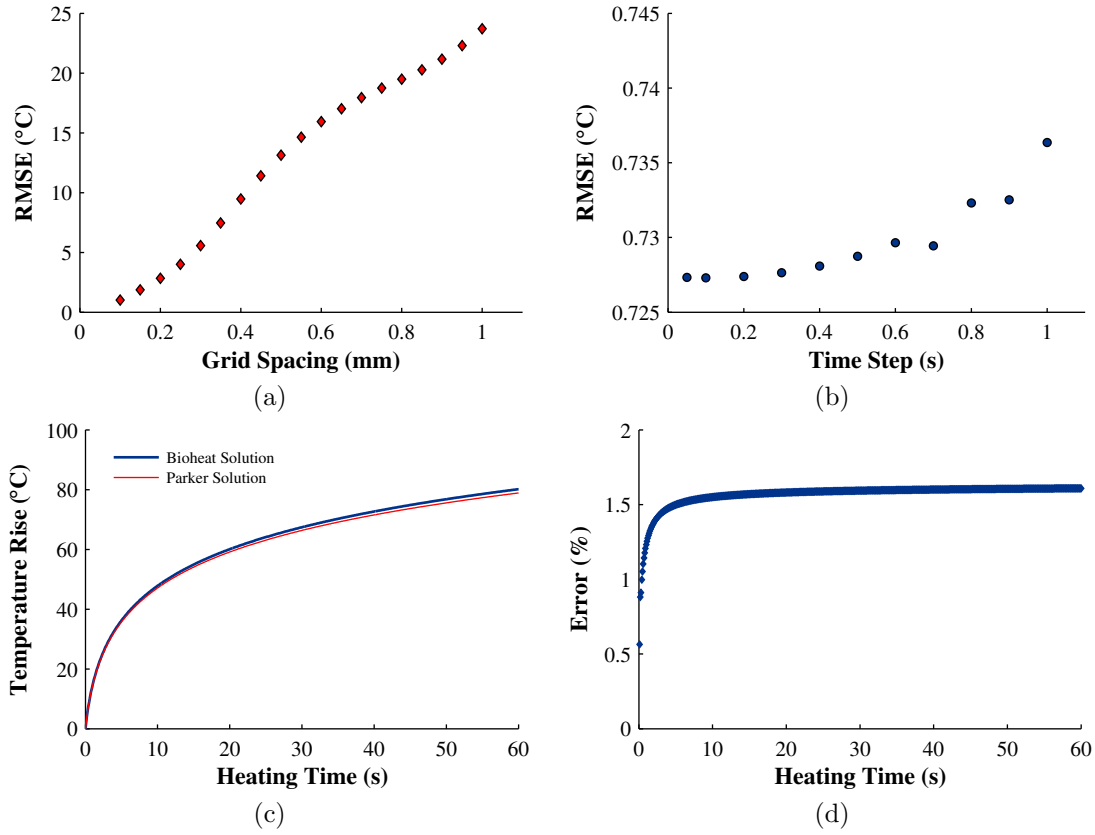

Figure 3·4: Validation of the focal temperature rise over 60 s calculated with the bioheat transfer code by comparison to Parker's analytical solution for a heat source extending infinitely along the z axis with a Gaussian radial profile. The root-mean-square error of the solution is shown as a function of grid spacing (a) and time step (b). (c) The temporal dependence of the two solutions for a grid spacing of 100 μm and a time step of 100 ms. (d) The error between the two solutions for the grid spacing and time step shown in (c).

heating, and not by mechanical effects. Given a simulation voxel with an average temperature of T_{avg} during the time step Δt, the thermal dose accumulated during Δt ws calculated as:

$$\Delta t_{43} = R^{43-T_{\text{avg}}} \Delta t, \tag{3.14}$$

where Δt is expressed in minutes. The isodose constant R was taken as 0.25 for $T_{\text{avg}} < 43°\text{C}$ and 0.63 for $T_{\text{avg}} > 43°\text{C}$ based on the measurements reported in Chapter 2 (Adams et al., 2014). At the end of the simulation time step, Δt_{43} was calculated for each voxel within the computational domain and added to the voxel's thermal dose before the time step.

Given the total thermal dose, t_{43}, in a voxel after each time step, the optical reduced scattering, μ_s', and absorption, μ_a, coefficients were both calculated using:

$$\mu = \mu_0 + (\Delta\mu)_{\max} \left(1 - \exp\left(-\frac{t_{43}}{\tau_{43}}\right)\right), \tag{3.15}$$

where μ_0 is the initial value of the coefficient, $(\Delta\mu)_{\max}$ is the maximum observable change in the coefficient, and τ_{43} is the thermal dose constant that governs the rate at which the property changes. As discussed in Section 2.4.1, $(\Delta\mu_s')_{\max}$ is temperature dependent. Therefore, the maximum temperature calculated for each voxel was also provided as an input to the function by the bioheat transfer equation code. A MATLAB function then generated the optical properties on a grid which could be imported into the optical code. Figure 3·5 shows μ_s' (a) and μ_a (b) in the axial plane of the chicken breast after an exposure of a target peak pressure of 6 MPa for 60 s, followed by 30 s of cooling. The resulting thermal dose after the exposure is shown in Fig. 3·5(c). The optical properties used for the calculations were derived from experimental data at 1064 nm (see Section 2.4), and are shown in Table 3.3.

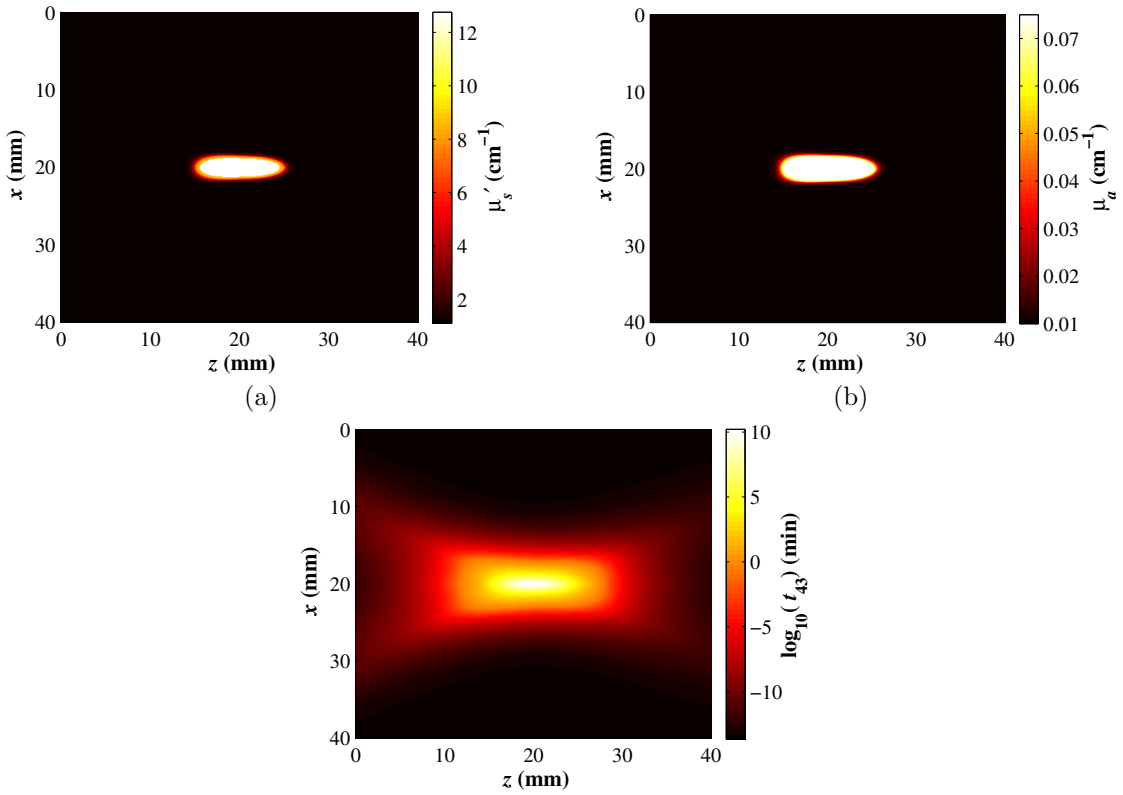

Figure 3·5: Calculated μ_s' (a) and μ_a (b) at 1064 nm in the axial plane of a chicken breast heated for 60 s with a target peak pressure of 6 MPa, followed by 30 s of cooling. (c) The resulting thermal dose after the exposure shown on a log scale.

Property	Scattering	Absorption
μ_0 (cm^{-1})	1.1	0.01
$(\Delta\mu)_{\max}$ (cm^{-1})	7.535 if $T_{\max} < 70$°C 11.66 if $T_{\max} > 70$°C	0.065
τ_{43} (min)	2214	598

Table 3.3: The optical properties of chicken breast at 1064 nm used in all simulations. Values are based on experimental data (Adams et al., 2014).

3.4 The Optical Field

3.4.1 Light Transport Theory

In order to properly model AO sensing as a mechanism for HIFU guidance, the propagation of light through tissue must be accurately modeled. The theory pertaining to light-tissue interactions and diffuse light transport in biological tissue is detailed in Chapter 2. As discussed, light transport in turbid media is described by the radiative transfer equation (Eq. 2.14). For the purposes of this work, the RTE is solved numerically using the Monte Carlo method (Wang et al., 1995a). Originally implemented to solve the diffusion of neutrons in fissionable materials (Metropolis, 1987), the Monte Carlo method has since seen widespread use for many other applications in which analytical solutions cannot be directly calculated, but can be broken up into subprocesses that are each characterized by a known probability distribution. By randomly and repeatedly sampling from these distributions, an accurate solution is obtained as the number of repetitions approaches infinity.

When applied to diffuse light transport, the Monte Carlo method offers the most accurate and flexible solutions to the RTE (Rubinstein and Kroese, 2007). However, the method is limited by its computational expense. Millions or billions of photon "packets" must be simulated in order to obtain an accurate solution of the optical field for a given tissue and illumination geometry. A photon packet is a group of photons that propagates through a unique optical path with a "weight", which represents the amount of energy present in the packet. In what follows, the terms photon and photon packet are used interchangeably. In order to enhance computational efficiency and reduce computation times, parallelization algorithms are often employed to simulate hundreds or thousands of photon packets simultaneously. One such algorithm that has seen widespread use in the optics community is Monte Carlo eXtreme (MCX) (Fang and Boas, 2009). MCX is an open-source (Fang, 2009), graphics processing

unit (GPU) accelerated Monte Carlo algorithm that is able to perform time resolved simulations in an arbitrarily complex tissue volume with heterogeneous optical properties. MCX was used as a basis for all of the AO code developed for this thesis, and its algorithm and implementation will be presented in the following section.

3.4.2 Monte Carlo Implementation

The important details of the MCX algorithm will be presented in this section, but the reader is referred to Fang and Boas (2009) for a full description. Implemented in the CUDA programming language, MCX uses a GPU to simultaneously propagate thousands[1] of photon packets through a tissue volume with circular detectors at the tissue boundaries. Once the specified number of photon packets have been propagated, the results from the individual photon packets (expressed as raw probabilities) are coherently summed and normalized to obtain a statistical representation of the fluence rate within the tissue. When a photon packet reaches a detector, its information – the number of scattering events it's experienced and the total path length it's traveled in each medium type[2] within the tissue – is saved. The workflow of each individual photon packet is summarized in Fig. 3·6, where the steps at which a probability distribution is randomly sampled are shown with rounded red boxes.

The Workflow of Each Photon Packet

The source condition for each MCX simulation is a unity pencil beam[3] with a specified location $\vec{r}$ and direction $\hat{s}$. Each photon emanating from the source has an initial packet weight of 1. Once launched, the code calculates the free path, l_s, of the photon in direction $\hat{s}$ before encountering its first scattering event. Each free path is

[1] The number of photon packets simulated simultaneously is dependent upon the number of threads available on the GPU.
[2] A medium type refers to one or more voxels with a unique set of optical properties.
[3] A pencil beam is an infinitely narrow source with a specified direction.

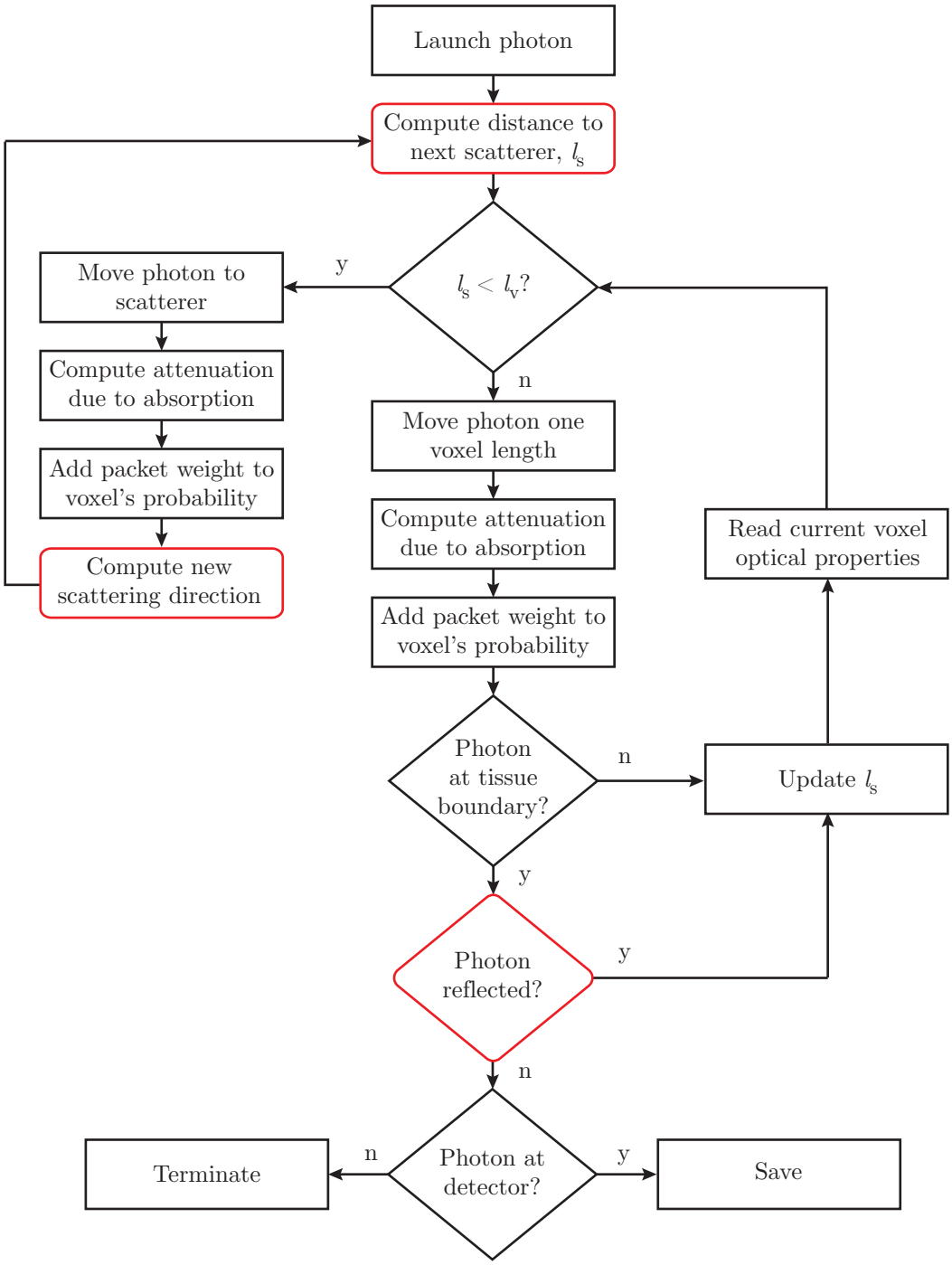

Figure 3·6: The workflow of a single photon packet in the Monte Carlo light transport model. Millions of photon packets must be simulated to yield an accurate solution of the optical field. The rounded red boxes indicate steps at which a probability distribution is randomly sampled.

a randomly chosen value taken from probability density function with an exponential distribution, and it is calculated using:

$$l_{\mathrm{s}} = \frac{-\ln \xi}{\mu_s}, \tag{3.16}$$

where ξ is a random number distributed between 0 and 1. All random numbers are generated using a logistic-lattice algorithm (Phatak and Rao, 1995; Wagner, 1992) with a lattice size of 5. The code attempts to move the photon one voxel length l_{v}, along $\hat{s}$. If $l_{\mathrm{v}} < l_{\mathrm{s}}$, l_{s} is adjusted at the voxel boundary according to the optical properties of the voxel it is entering. If $l_{\mathrm{s}} < l_{\mathrm{v}}$, the photon is stopped at the end of its trajectory. Once stopped at the voxel boundary or at the scatterer, the packet weight is reduced by the absorption coefficient along the step according to Eq. 2.1 and it is added to the current voxel's raw probability, P_{raw}. If the user is performing a time resolved simulation, the probability is binned based on a time gate. A new scattering direction vector is calculated using a Henyey-Greenstein phase function (Henyey and Greenstein, 1941). As discussed in Section 2.1.2, the azimuthal angle Ψ is randomly distributed between 0 and 2π. Therefore,

$$\Psi = 2\pi\xi, \tag{3.17}$$

and the zenith angle θ is calculated using:

$$\cos\theta = \frac{1}{2g}\left[1 + g^2 - \left(\frac{1-g^2}{1-g+2g\xi}\right)^2\right]. \tag{3.18}$$

If a photon packet traveling in the direction $\hat{\Omega}$ is scattered at an angle (θ, Ψ), its new direction $\hat{\Omega}'$ is given by (Wang and Wu, 2012):

$$\hat{\Omega}'_x = \frac{\sin\theta(\hat{\Omega}_x\hat{\Omega}_z\cos\Psi - \hat{\Omega}_y\sin\Psi)}{\sqrt{1-\hat{\Omega}_z^2}} + \hat{\Omega}_x\cos\theta,$$

$$\hat{\Omega}'_y = \frac{\sin\theta(\hat{\Omega}_y\hat{\Omega}_z\cos\Psi + \hat{\Omega}_x\sin\Psi)}{\sqrt{1-\hat{\Omega}_z^2}} + \hat{\Omega}_y\cos\theta,$$

$$\hat{\Omega}'_z = -\sqrt{1-\hat{\Omega}_z^2}\sin\theta\cos\Psi + \hat{\Omega}_z\cos\theta. \tag{3.19}$$

If the photon direction is very close to the z-axis, the following formulas are used instead:

$$\hat{\Omega}'_x = \sin\theta\cos\Psi,$$

$$\hat{\Omega}'_y = \sin\theta\sin\Psi,$$

$$\hat{\Omega}'_z = \mathrm{sgn}(\hat{\Omega}_z)\cos\theta, \tag{3.20}$$

where sgn is the sign function.

A photon packet propagates through the tissue volume until it reaches a boundary between two media with different refractive indices. Upon reaching such a boundary, the probability of a photon being internally reflected is determined by the Fresnel reflection coefficient $R(\theta_i)$:

$$R(\theta_i) = \frac{1}{2}\left[\frac{\sin^2(\theta_i-\theta_t)}{\sin^2(\theta_i+\theta_t)} + \frac{\tan^2(\theta_i-\theta_t)}{\tan^2(\theta_i+\theta_t)}\right], \tag{3.21}$$

where $\theta_i = \cos^{-1}\hat{\Omega}_{x,y,z}$ is the angle of incidence on the x, y, or z boundary and θ_t is determined by Snell's law:

$$n_i\sin\theta_i = n_t\sin\theta_t. \tag{3.22}$$

After calculating the probability of internal reflection, a random number is generated

and if $\xi < R(\theta_i)$ the photon is reflected and the appropriate x, y, or z component of its directional vector is flipped. Otherwise, the photon exits the current voxel. If the photon exits the computational volume and is incident upon a detector, its weight and its total number of scattering events are saved.

The Simulation Output

As previously discussed, the result from each Monte Carlo simulation is the raw probability, P_{raw} (unitless), accumulated in each voxel[4]. Therefore, at the conclusion at each simulation, P_{raw} must be converted into a physical quantity via a normalization procedure. The specifics of the photon normalization procedure are beyond the scope of this discussion, but the details can be found in literature (Boas et al., 2002; Fang and Boas, 2009). By default, the output of MCX is the time-resolved particle flux distribution, $F(r, t_i)$ ($1/\text{mm}^2 \cdot s$), for a unitary source of infinitely narrow pulse width. For the purposes of this work, we are interested in the fluence rate distribution, $\Phi(r)$ (W/mm^2), produced by a CW source of power S_0. In order to convert the particle flux within each time gate to a CW fluence rate distribution, $F(r, t_i)$ was multiplied by the time gate length, $\Delta t_{g,i}$ and summed:

$$\Phi(r) = S_0 \sum_i F(r, t_i) \Delta t_{g,i} \tag{3.23}$$

3.4.3 Validation

Although Monte Carlo algorithms are considered to be more accurate than any analytical diffuse light transport model, it is still necessary to validate them to ensure they don't contain any numerical errors or unwanted biases. As discussed in Section 2.2, the most common analytical solution to the radiative transfer equation (RTE) is known as the diffusion approximation (Farrell et al., 1992; Kienle and Patterson,

[4] The simulation also outputs the information collected by each detector, which is already in physical units.

1997; Contini et al., 1997). MCX has been vigorously validated against the diffusion approximation (Fang and Boas, 2009), but an additional comparison is presented here to confirm the accuracy of the code implemented in this work.

The diffusion approximation solution to the RTE for a homogeneous semi-infinite medium for a 1 W CW point source of light located at r_s and measured at r_d is given by:

$$\Phi(r_s, r_d) = \frac{1}{4\pi D}\left[\frac{\exp(-\sqrt{3\mu_s'\mu_a}\,|r_s - r_d|)}{|r_s - r_d|} - \frac{\exp(-\sqrt{3\mu_s'\mu_a}\,|r_{s,i} - r_d|)}{|r_{s,i} - r_d|}\right], \qquad (3.24)$$

where $D = 1/3\mu_s'\mu_a$ is the diffusion constant. The semi-infinite boundary condition is satisfied by using the method of images with an extrapolated boundary condition (Haskell et al., 1994). Figure 3·7 shows a comparison between Eq. 3.24 and the MCX solution for the fluence rate inside of an approximately semi-infinite medium with the optical properties of breast tissue at 1064 nm (Koelzer et al., 1995), which are shown in Table 3.4. The semi-infinite medium condition was approximated by simulating 100 million photons in a 60x60x60 mm^3 volume. The source was positioned at $(x, y, z) = (30, 30, 0)$ mm and was directed along the z-axis. Figure 3·7 shows the fluence rate distributions calculated along the (30, 30, z) (a) and (x, 30, 30) (c) axes, which correspond to the the source propagation axis and the transverse axis at

Property	Value
λ (nm)	1064
μ_a (cm^{-1})	0.097
μ_s (cm^{-1})	7.57
g	0.9
n_0	1.4

Table 3.4: The optical properties of breast used in the MCX validation simulation. n_0 is the equilibrium refractive index of the tissue.

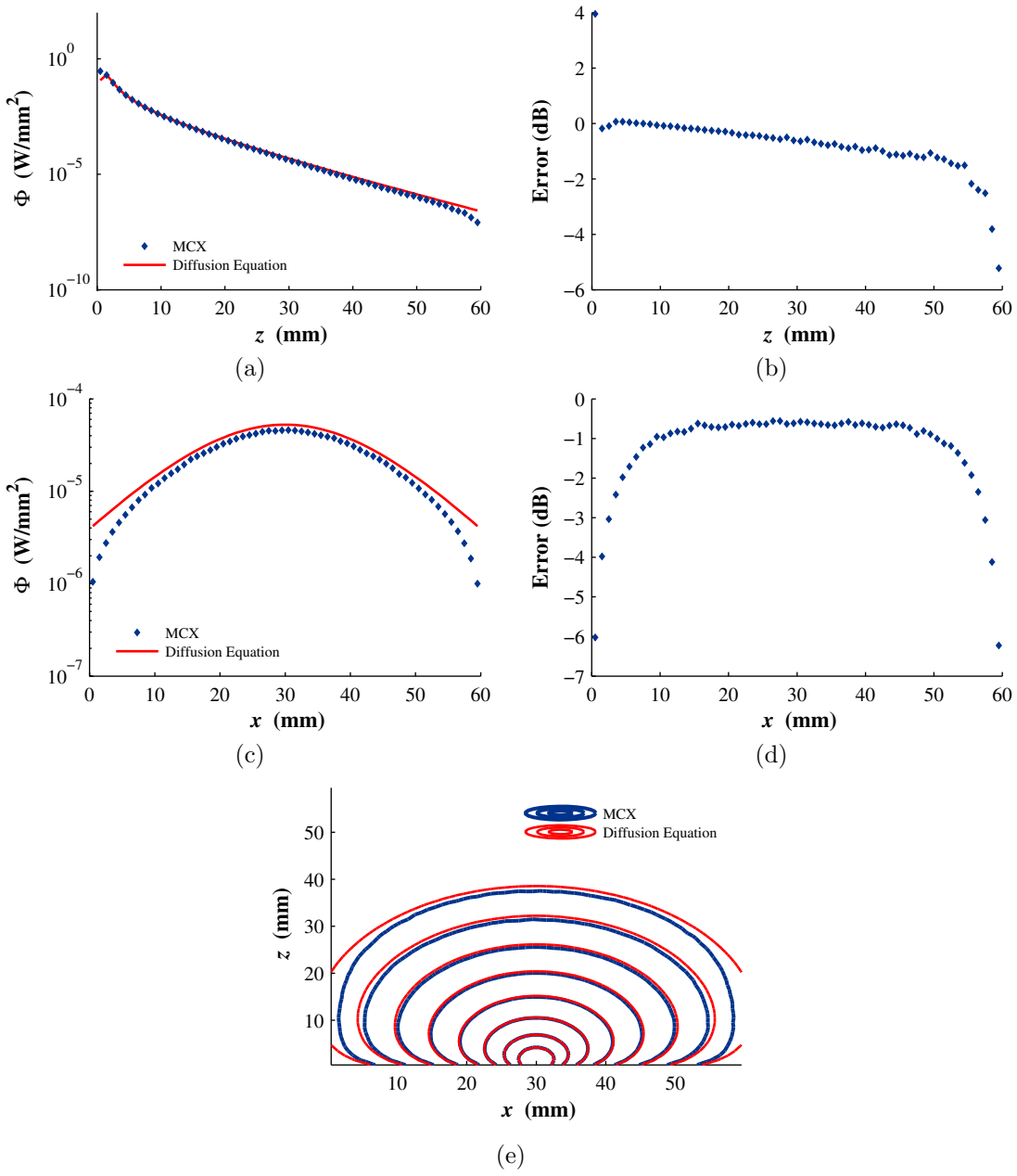

Figure 3·7: Validation of the CW fluence rate distribution calculated by MCX for a tissue with the optical properties of breast at 1064 nm by comparison to the diffusion approximation solution. Fluence rates are shown along the (30, 30, z) (a) and (x, 30, 30) (c) axes, and the error between the MCX and diffusion approximation solutions at these locations are shown in (b) and (d). (e) A contour plot (10 dB spacing) of the two solutions in the source plane.

the half-depth of the tissue respectively. The error between the MCX solution and the diffusion approximation solutions along these axes are shown in (b) and (d). A contour plot (10 dB spacing) is shown for the two solutions in the source plane (e). The error between the two solutions is small for all positions that aren't near the source or the boundaries, where the MCX medium is no longer semi-infinite and the diffusion approximation isn't valid.

3.5 The Acousto-Optic Effect

3.5.1 Theory

For the purposes of modeling AO sensing for HIFU guidance, the phase modulations imparted on diffuse coherent light by the CW HIFU field must be calculated, and how these phase modulations are detected in an actual physical experiment must be modeled. This section will present the theory and implementation relevant to calculating AO phase modulations, and the detection of these phase modulations will be presented in Section 3.6. As discussed in Section 1.2.1, there are two primary mechanisms responsible for the ultrasound induced phase modulations imparted on diffuse light (Wang, 2001b,a). Although a third mechanism also exists – the perturbation of the medium's optical absorption and scattering properties due to the compression and rarefaction of the tissue (Mahan et al., 1998) – it is very weak and will thus be ignored in this work. These two primary mechanisms, which require the light to be temporally coherent throughout its propagation, will be discussed further here. The theory presented here assumes the mean free path of a photon is much greater than the optical wavelength, the ultrasound induced refractive index perturbations are small enough to be linearly proportional to the pressure amplitude, and the ultrasound induced displacement of the scatterers are much less than the optical wavelength (Sakadžić and Wang, 2005). The latter two assumptions impose upper

limits on the allowable acoustic pressure amplitude, as discussed below.

An acoustic field generates a strain which alters the refractive index of the medium in which propagates (Raman and Nagendra Nath, 1935; Wang, 2001b). This phenomenon is known as the elasto-optic effect, and assuming the perturbation of the dielectric permittivity due to the acoustic pressure $p(\vec{r},t)$ is small, the modulated refractive index of an insonified material is given by:

$$\Delta n(\vec{r},t) = n_0 \frac{\partial n}{\partial p} p(\vec{r},t), \tag{3.25}$$

where $\frac{\partial n}{\partial p}$ is the adiabatic piezo-optic coefficient of the material. As a result of the modulated refractive index, the optical phase between two consecutive scattering events is also modulated. Considering a plane electromagnetic wave with wavenumber k_0 propagating between two points $\vec{r}_{i-1}$ and $\vec{r}_i$ within an insonified medium, the phase variation (from that of an optically homogeneous medium) along this path is given by:

$$\phi_{n,i}(\vec{r}_{i-1},\vec{r}_i,t) = k_0 n_0 \frac{\partial n}{\partial p} \int_{\vec{r}_{i-1}}^{\vec{r}_i} p(\vec{r},t)\,\mathrm{d}\vec{r}, \tag{3.26}$$

where k_0 is the optical wave number.

In addition to the phase modulations generated by ultrasound induced refractive index perturbations, the displacements of optical scatterers in an insonified medium modulate the path lengths of the multiply scattered light that propagates through it (Leutz and Maret, 1995; Wang, 2001b). Assuming that optical scatterers follow the movement of the background medium in amplitude, phase, and direction, the periodic displacement of optical scatterers from their rest positions induced by the propagation of a monochromatic acoustic wave is described by:

$$\vec{\xi}_s(\vec{r},t) = \hat{\Omega}_a \int u(\vec{r},t)\,\mathrm{d}t, \tag{3.27}$$

where $\hat{\Omega}_a$ is the acoustic propagation direction (given by the directional vector of the particle velocity). Given this particle displacement, the phase variation at the i'th scattering event is given by:

$$\phi_{d,i}(\vec{r},t) = k_0 n_0 \hat{\Omega}_a \cdot (\hat{\Omega}_{inc} - \hat{\Omega}_{sc}) \int u(\vec{r},t)\,\mathrm{d}t, \tag{3.28}$$

where $\hat{\Omega}_{inc}$ and $\hat{\Omega}_{sc}$ are the incident and scattered photon directions, respectively.

The total ultrasound induced phase modulation over a single optical path involving N free paths and $N-1$ scattering events is a summation of the perturbations expressed in Eqs. 3.26 and 3.28, and it is given by:

$$\phi_{\mathrm{us}}(t) = \sum_{i=1}^{N-1} \phi_d(\vec{r}_i,t) + \sum_{i=1}^{N} \phi_n(\vec{r}_{i-1},\vec{r}_i,t), \tag{3.29}$$

where i is a single scattering event, $\vec{r}_0$ is the source location, and $\vec{r}_N$ is the detector location. Assuming that the medium is insonified by a monochromatic acoustic field with a temporal behavior described by $\mathrm{e}^{-i\omega_a t}$, $\phi_{\mathrm{us}}(t)$ may be expressed as (Blonigen et al., 2005; Sakadžić and Wang, 2006b; Powell and Leung, 2012):

$$\phi_{\mathrm{us}}(t) = \mathrm{Re}\left\{|\phi_{\mathrm{us}}| \exp(-i[\omega_a t + \varphi_{\mathrm{us}}])\right\}, \tag{3.30}$$

where $|\phi_{\mathrm{us}}|$ and φ_{us} are the magnitude and phase angle of ϕ_{us} respectively. Thus, when considering an optical wave propagating along an optical path s within a diffusive and insonified medium, the electric field of the wave, $E_s(\vec{r},t)$ takes the form:

$$E_s(\vec{r},t) = a_s(\vec{r}) \exp(-i[\omega_0 t + \phi_{m,s}(\vec{r},t) + \phi_{\mathrm{us},s}(\vec{r},t)]), \tag{3.31}$$

where a_s is the amplitude of the electric field and $\phi_{m,s}$ is some random phase due to the multiple scattering process (which may randomly fluctuate due to effects such as Brownian motion).

The power of the modulated and unmodulated light in each optical path is given by the power spectrum of $E_s(\vec{r},t)$. According to the Wiener-Khinchin theorem (Goodman, 1985), the power spectrum of a wide-sense stationary electric field is given by the Fourier transform of its temporal autocorrelation function, $G(\tau)$:

$$G(\tau) = \left| \int_{-\infty}^{\infty} E(\vec{r},t)E^*(\vec{r},t-\tau)\,\mathrm{d}t \right|. \tag{3.32}$$

Neglecting Brownian motion and other temporal fluctuations in $\phi_{m,s}$, assuming that the mean free path between scatterers is much greater than the optical wavelength, and assuming that the ultrasound induced scatterer displacements are small, the autocorrelation function of a single optical path is given by (Sakadžić and Wang, 2006b):

$$G_s(\tau) = \frac{\omega_a}{2\pi} \int_0^{2\pi/\omega_a} a_s^2 \exp(i|\phi_{\mathrm{us},s}|\{\cos(\omega_a t + \varphi_{\mathrm{us},s}) - \cos[\omega_a(t+\tau) + \varphi_{\mathrm{us},s}]\}). \tag{3.33}$$

By expanding the exponentiated cosine function into a series of Bessel functions via the Jacobi-Angers identity (Abramowitz and Stegun, 1972), the integral in Eq. 3.33 can be evaluated, yielding the expression:

$$G_s(\tau) = a_s^2 \left[J_0^2(|\phi_{\mathrm{us},s}|) + \sum_{m=1}^{\infty} 2J_m^2(|\phi_{\mathrm{us},s}|)\cos(m\omega_a\tau) \right], \tag{3.34}$$

where J_m is a Bessel function of the first kind of order m. Therefore, the power spectrum of each optical path will consist of a strong unmodulated component at ω_0 proportional to $J_0^2(|\phi_{\mathrm{us}}|)$, and numerous modulated sidebands shifted by multiples of ω_a, where the power of the m'th sideband is proportional to $2J_m^2(|\phi_{\mathrm{us}}|)$.

3.5.2 Numerical Implementation

Acousto-optic calculations were implemented by modifying the Monte Carlo algorithm, MCX, presented in Section 3.4.2. The modifications were implemented in a procedure similar to that employed by Sakadžić and Wang (2006b), and they will be described here. At the initialization of a Monte Carlo simulation, each voxel was assigned a four-element array: $[p_0\hat{\Omega}_{a,x}, p_0\hat{\Omega}_{a,y}, p_0\hat{\Omega}_{a,z}, \phi_a]$, where ϕ_a is the acoustic phase constant within the voxel, and the average propagation direction within the voxel, $\hat{\Omega}_a = \vec{k}_a/k_a$, was derived from the particle velocity field. The array describing the acoustic field was loaded onto the global memory of the GPU. The acoustic field from the angular spectrum solution was expressed in each voxel as:

$$p\,(t) = p_0 \cos(\omega_a t + \phi_a). \tag{3.35}$$

For each photon packet step of length l_i within a given voxel, the phase increment accumulated by the packet due to the modulation of the refractive index, $\Delta\phi_{n,i}$, was calculated using Eq. 3.26 as:

$$\Delta\phi_{n,i}(t) = \frac{k_0 n_0 l_i \eta}{\rho_0 c_a^2} p(t), \tag{3.36}$$

where $\eta = \frac{\partial n}{\partial p}\rho_0 c_a^2$ is known as the elasto-optic coefficient of the tissue. Alternatively, Eq. 3.36 may be expressed as:

$$\Delta\phi_{n,i}(t) = p_{n,\cos,i}\cos(\omega_a t) + p_{d,\sin,i}\sin(\omega_a t), \tag{3.37}$$

where:

$$\begin{aligned} p_{n,\cos,i} &= \frac{k_0 n_0 l_i \eta}{\rho_0 c_a^2} p_0 \cos(\phi_a), \\ p_{n,\sin,i} &= -\frac{k_0 n_0 l_i \eta}{\rho_0 c_a^2} p_0 \sin(\phi_a). \end{aligned} \tag{3.38}$$

Similarly, for each scattering event j, the phase increment accumulated by the packet due to the ultrasound induced scatterer displacement, $\Delta\phi_{d,j}$, was calculated using Eq. 3.28 as:

$$\Delta\phi_{d,j}(t) = \frac{k_0 n_0}{k_a \rho_0 c_a^2} \hat{\Omega}_a \cdot (\hat{\Omega}_{inc} - \hat{\Omega}_{sc}) \int p(t)\, \mathrm{d}t. \tag{3.39}$$

Alternatively, Eq. 3.39 may be expressed as:

$$\Delta\phi_{d,j}(t) = p_{d,\cos,j} \cos(\omega_a t) + p_{d,\sin,j} \sin(\omega_a t), \tag{3.40}$$

where:

$$\begin{aligned} p_{d,\cos,j} &= \frac{k_0 n_0}{k_a \rho_0 c_a^2} \hat{\Omega}_a \cdot (\hat{\Omega}_{inc} - \hat{\Omega}_{sc}) p_0 \sin(\phi_a), \\ p_{d,\sin,j} &= \frac{k_0 n_0}{k_a \rho_0 c_a^2} \hat{\Omega}_a \cdot (\hat{\Omega}_{inc} - \hat{\Omega}_{sc}) p_0 \cos(\phi_a). \end{aligned} \tag{3.41}$$

At each step, the total ultrasound induced phase shift, $\phi_{\mathrm{us}}(t)$, of the photon packet was calculated using Eq. 3.29:

$$\phi_{\mathrm{us}}(t) = \left[\sum_i p_{n,\cos,i} + \sum_j p_{d,\cos,j} \right] \cos(\omega_a t) + \left[\sum_i p_{n,\sin,i} + \sum_j p_{d,\sin,j} \right] \sin(\omega_a t), \tag{3.42}$$

and it can be expressed in the form of Eq. 3.30, where $|\phi_{\mathrm{us}}|$ and φ_{us} are calculated using:

$$\begin{aligned} |\phi_{\mathrm{us}}| \cos(\varphi_{\mathrm{us}}) &= \sum_i p_{n,\cos,i} + \sum_j p_{d,\cos,j}, \\ |\phi_{\mathrm{us}}| \sin(\varphi_{\mathrm{us}}) &= -\sum_i p_{n,\sin,i} - \sum_j p_{d,\sin,j}. \end{aligned} \tag{3.43}$$

At each scattering event, the power spectrum of the modulated optical path was calculated using the Fourier transform of Eq. 3.34. Assuming that contributions from higher order sidebands are negligible, a portion of the packet weight, $J_0^2(|\phi_s|)W_s$, was

added to the voxel's unmodulated light probability, $P_{\text{raw},0}$, and a portion $2J_1^2(|\phi_s|)W_s$ was added to the voxel's modulated light probability $P_{\text{raw},1}$, (Sakadžić and Wang, 2006b) where J_n is a Bessel function of the n'th order. At the completion of the simulation, the raw probability fields of the modulated and unmodulated light were normalized using the same procedure referenced in Section 3.4.2, yielding the unmodulated, Φ_0, and modulated, Φ_1, fluence rates within the medium.

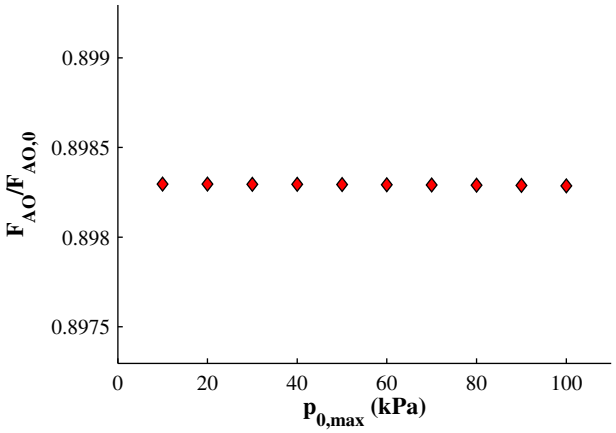

Figure 3·8: The ratio of the AO signal with and without a ∼30 mm^3 lesion in chicken breast illuminated with a 1064 nm source and insonified with 1.1 MHz HIFU at variable peak pressures.

In this implementation, a number of assumptions were used. First, it was assumed that the ultrasound induced phase modulations are small. This limits the acoustic pressures used in the AO simulations to ∼100 kPa (Sakadžić and Wang, 2006b). However, we often are only interested in the ratio of the AO signal with and without a lesion, $F_{\text{AO}}/F_{\text{AO},0}$, where F_{AO} is the AO radiant flux as defined below in Eq. 3.46. As shown in Fig. 3·8, where $F_{\text{AO}}/F_{\text{AO},0}$ is plotted as a function of peak pressure amplitude for a ∼30 mm^3 lesion, $F_{\text{AO}}/F_{\text{AO},0}$ is approximately independent of pressure. Additionally, it was assumed that the acoustic field is monochromatic and can accurately be described within a voxel using Eq. 3.35, which imposes an upper limit on the voxel size to ∼100 μm for a 1.1 MHz acoustic frequency. Next,

it was assumed that the displacement of the optical scatterers follow the background medium in phase, amplitude, and direction. Finally, it was assumed that because of the small ultrasound induced phase modulations, the contributions to the power spectrum from higher order sidebands are negligible.

3.5.3 Validation

The mathematics and physics associated with developing acousto-optic models are very complex, therefore few analytical formulations are available to validate the AO Monte Carlo model with. Nevertheless, a temporal correlation diffusion equation exists which can be used to calculate the power spectrum of light modulated by a nonuniform ultrasound field in an optically scattering and absorbing medium (Sakadžić and Wang, 2006a). Using a solution to this equation, the AO Monte Carlo algorithm was validated by comparison to an analytical solution for the modulation depth, MD $= \Phi_1/\Phi_0$, within an optically homogeneous and diffusive semi-infinite slab of width 20 mm, insonified by a 3.175 mm radius cylinder of plane wave ultrasound. In order to mimic the configuration used for the solution presented by Sakadžić and Wang (2006a), the simulation was performed in a cuboid medium of dimensions 20x100x40 mm^3, with a voxel size of 100 μm. The dimensions of the medium were chosen to minimize boundary effects. As shown in Fig. 3·9(a), the medium was illuminated at $(x, y, z) = (0, 10, 0)$ mm with a 532 nm pencil beam launching 500 million photons in $+x$, and the acoustic and optical properties of the medium are given in Table 3.5.

The modulation depth was evaluated along the y axis in both the reflection ($x = 0$ mm) and transmission ($x = 20$ mm) planes ($z = 0$ mm for all cases). As shown in Fig. 3·9(b), excellent agreement was found between the AO MCX code and the analytical solution. The large discrepancy near the source ($y = 10$ mm) is due to a diffusion approximation used when deriving the analytical solution. At all other evaluated locations, the error between the Monte Carlo code and the analytical solution is less

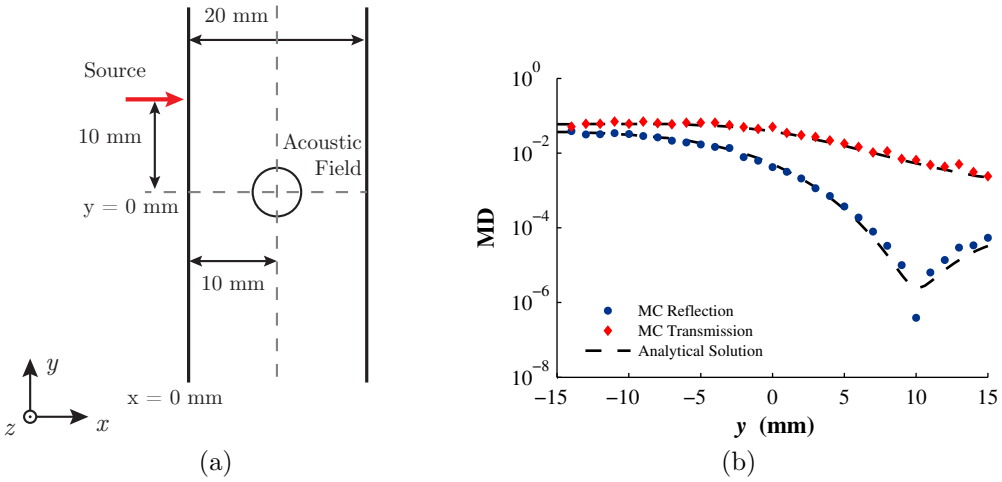

Figure 3·9: Validation of the AO MCX code by comparison to the modulation depth, MD, inside of an optically homogenous medium insonified by a 3.175 mm radius cylinder of plane wave ultrasound. (a) A cross-section ($z = 0$) of the computational domain used to validate the AO MCX code. The properties of the medium are given in Table 3.5. The cylinder of ultrasound propagates in the $+z$ direction, and the optical source location and direction is indicated by the red arrow. (b) Comparison of the MD along the y-axis in the reflection, $x = 0$ mm, (blue circles) and transmission, $x = 20$ mm, (red diamonds) planes.

than 2 dB.

3.6 Acousto-Optic Signal Detection

As discussed in Section 1.2.2, photorefractive holography using a GaAs crystal is the only AO detection method that has been used for HIFU guidance to date. Thus, all of the simulations performed in this work use a photorefractive crystal (PRC) detection model. The principles of PRC-based detection were introduced in Section 1.2.2, and the theory pertaining to the two-wave mixing that occurs within the PRC will be discussed further here. For a more complete description of PRC-based AO detection, the reader is referred to Sui (2006) and Lai (2010).

Property	Value	Property	Value
c_a (m/s)	1480	ρ_0 (kg/m^3)	1000
f_0 (MHz)	1.1	p_0 (kPa)	100
λ_0 (nm)	532	n_0	1.33
μ_s (cm^{-1})	10	μ_a (cm^{-1})	0.1
g	0.001	η	0.32

Table 3.5: The acoustic and optical properties of the medium used to validate the AO MCX code. The properties were chosen to match the analytical solution presented in (Sakadžić and Wang, 2006a).

3.6.1 PRC Theory

When light exits the tissue at a boundary, the signal beam is gathered by a diffuse light collection system and it forms a speckle pattern at the face of a PRC. As discussed in Section 1.2.2, the interference pattern between the spatially incoherent signal beam and a coherent reference beam creates a hologram within the PRC in the form of a refractive index grating. The time required to form this grating is referred to as the PRC response time (Millerd et al., 1998) and is ∼20 ms for a GaAs crystal (Lai, 2010). The grating is able to adapt itself to any variations in the signal beam that occur on a slower time scale than its response time. In the absence of ultrasound modulation, a portion of the reference beam diffracts from the refractive index grating into the direction of the signal beam. The efficiency of the reference beam diffraction is described by the two-wave mixing (TWM) gain of the crystal, $\gamma = \gamma' + i\gamma''$, and the existence of an imaginary component of γ means that the reference beam may be uniformly shifted in phase with respect to the signal beam. For the purposes of AO guidance, the PRC is normally configured such that γ is purely real. Thus, the diffracted reference beam and the signal beam are perfectly in phase and thus interfere constructively, yielding a maximum optical intensity at the output of the PRC, which we will refer to as an "enhanced" signal beam.

In the presence of ultrasound induced modulations, the refractive index grating cannot adapt to the quickly changing signal beam, and thus an intensity change is observed in the enhanced signal beam. The intensity of the enhanced signal beam in the presence of ultrasound induced modulations is a summation of the contributions from each optical path, and is given by (Delaye et al., 1995; Blonigen et al., 2005):

$$I_{SE}(t) = \exp(-\alpha_c L_c) \sum_s a_s^2 [|\exp(\gamma L_c)|^2 + 2\,\mathrm{Re}([\exp(\gamma L_c) - 1] \times [\exp(i\phi_{\mathrm{US},s}(t)) - 1])], \tag{3.44}$$

where α_c is the absorption coefficient of the crystal and L_c is the optical path length of the crystal. It can be seen by inspection that the random phase term, $\phi_{m,s}$ in Eq. 3.31, responsible for the spatial incoherence of the signal beam has vanished. By applying a Bessel series expansion to the last term in Eq. 3.44 and retaining only the lowest order terms, the expression for the enhanced signal beam can be broken into three components:

$$\begin{aligned} I_{SE}^{N} &= \exp(-\alpha_c L_c) \exp(2\gamma' L_c) \sum_s a_s^2, \\ I_{SE}^{AC} &= 4 \exp(-\alpha_c L_c) \exp(\gamma' L_c) \sin(\gamma'' L_c) \sum_s a_s^2 J_1(|\phi_{\mathrm{US},s}|) \cos(\omega_a t + \varphi_{\mathrm{US},s}), \\ I_{SE}^{DC} &= 2 \exp(-\alpha_c L_c)(\exp(\gamma' L_c) \cos(\gamma'' L_c) - 1) \sum_s a_s^2 (J_0(|\phi_{\mathrm{US},s}|) - 1). \end{aligned} \tag{3.45}$$

The first component of the signal, I_{SE}^{N} is a DC offset signal that contains no information about phase modulations, but it is the dominant source of noise in the signal. The second component I_{SE}^{AC} is an AC signal whose amplitude is proportional to both $|\phi_{\mathrm{US},s}|$ and $\varphi_{\mathrm{US},s}$. Since $\varphi_{\mathrm{US},s}$ varies randomly from 0 to 2π between different optical paths, the AC contributions from different paths do not add coherently. Additionally, when γ is purely real, $I_{SE}^{AC} = 0$. The final component I_{SE}^{DC} is a DC signal, which is

proportional only to $|\phi_{\mathrm{US},s}|$. Therefore, the contributions from each optical path add coherently to produce this signal. This is the signal that is used for AO sensing, and we will heretofore refer to the radiant flux of I_{SE}^{DC} at the photodetector as the "AO signal", F_{AO}, defined by:

$$F_{\mathrm{AO}} = I_{SE}^{DC} A_{\mathrm{det}}, \tag{3.46}$$

where A_{det} is the active area of the photodetector.

3.6.2 Numerical Implementation

To simulate the PRC-based detection of AO signals in the AO MCX code, circular detectors of radius r and efficiency η_{det} (see Section 3.6.3 below) were placed directly on the boundaries of the tissues. When a photon packet reached a detector, its packet weight, W_s, and its phase modulation terms, $|\phi_{\mathrm{US},s}|$ and $\varphi_{\mathrm{US},s}$ were recorded. At the completion of each AO MCX simulation, the detected AO signal was calculated in a post-processing manner using MATLAB. First, the total radiant flux, F_t, to reach each detector was calculated as:

$$F_t = S_0 \sum_s W_s, \tag{3.47}$$

where S_0 is the simulated source power and s corresponds to a single photon packet. The total radiant flux to reach the detector was then scaled by η_{det} to account for the diffuse light collection system, and the detected AO signal, F_{AO} was calculated as:

$$F_{\mathrm{AO}} = 2\eta_{\mathrm{det}} S_0 \exp(-\alpha_c L_c) \left(\exp(\gamma' L_c)\cos(\gamma'' L_c) - 1\right) \sum_s W_s (J_0(|\phi_{\mathrm{US},s}|) - 1). \tag{3.48}$$

3.6.3 Light Collection Efficiency of the Simulation Detectors

The efficiency of a diffuse light collection system is governed by the theory of étendue, which specifies the geometric capability of the system to transmit and accept light

(Chaves, 2008). For a conical beam normal to a source or detector of area A, étendue, G_0, can be expressed as a product of the component's area, A, and the projected solid angle at which light is transmitted or received, Ω:

$$G_0 = A\Omega. \tag{3.49}$$

At the surface of the tissue, the angle at which light can be transmitted through the tissue is limited by the critical angle, θ_c. At angles greater than θ_c, measured with respect to the axis normal to the tissue boundary, light is internally reflected within the tissue. For a tissue submerged in water, θ_c is calculated as:

$$\theta_c = \arcsin\left(\frac{n_{\text{water}}}{n_{\text{air}}}\right). \tag{3.50}$$

Therefore, given an AO MCX detector of area A_{det} placed on the boundary of the tissue, the étendue at which light is transmitted through this detector can be calculated as:

$$G_{\text{det}} = A_{\text{det}}\pi \sin^2\theta_c. \tag{3.51}$$

The efficiency of a system is constrained by its component with the smallest étendue. In the PRC-based detector, the PRC itself is the constraining component in the system. Therefore, the solid angle at which light is accepted from the surface of the tissue, Ω_a, over an area A_{det} is constrained by the étendue of the PRC, G_{PRC}. Given G_{PRC}, Ω_a is calculated as:

$$\Omega_a = \frac{G_{\text{PRC}}}{A_{\text{det}}}. \tag{3.52}$$

The PRC modeled in this system accepts light over an area of 49 mm^2, and accepts light over a projected solid angle of 0.16, which is constrained by the angle between the signal and reference beam. This results in an étendue of 7.8 mm^2.

Given the solid angles over which light is transmitted from the tissue, and the solid angle at which the light is accepted over an area of A_{det}, the light collection efficiency of a simulated detector can be calculated as the ratio of the two solid angles:

$$\eta_{\text{det}} = \frac{\Omega_a}{\pi \sin^2 \theta_c}. \tag{3.53}$$

Therefore, for an MCX detector with a 20 mm radius placed on the surface of the tissue, $\eta_{\text{det}} = 0.004$.

3.7 Integration of the Models

3.7.1 An Example Script

Although each of the models described in Sections 3.1 – 3.6 were written as separate MATLAB functions or CUDA binaries, they were implemented in a way that they could be integrated together in a single MATLAB script to model the AO guidance of HIFU. An example of such a script is presented in Appendix B, where a 40x40x40 mm^3 cube of chicken breast tissue is illuminated with a 1064 nm light source and exposed to a target peak pressure of 6 MPa for 120 s, and F_{AO} was calculated every 5 s (using a peak pressure of 100 kPa). Figure 3·10(a,c) shows the distribution of Φ_0 and Fig. 3·10(b,d) shows the distribution of Φ_1 before (3·10(a,b)) and after (3·10(c,d)) the exposure given in this script. 100 million photon packets are used for each AO simulation.

Additionally, Fig. 3·11 shows the AO signal (a) and the lesion volume (b) as a function of HIFU exposure time, as well as the percent change in the AO signal as a function of lesion volume (c). The noise shown in Fig. 3·11(a) was calculated based on the SNR of the signal – a function of I_{AO}^N – and the method used for calculating it will be presented in Chapter 5. Although the HIFU exposure parameters (pressure amplitude, tissue thickness) are significantly different, by comparing Fig. 3·11(a) and

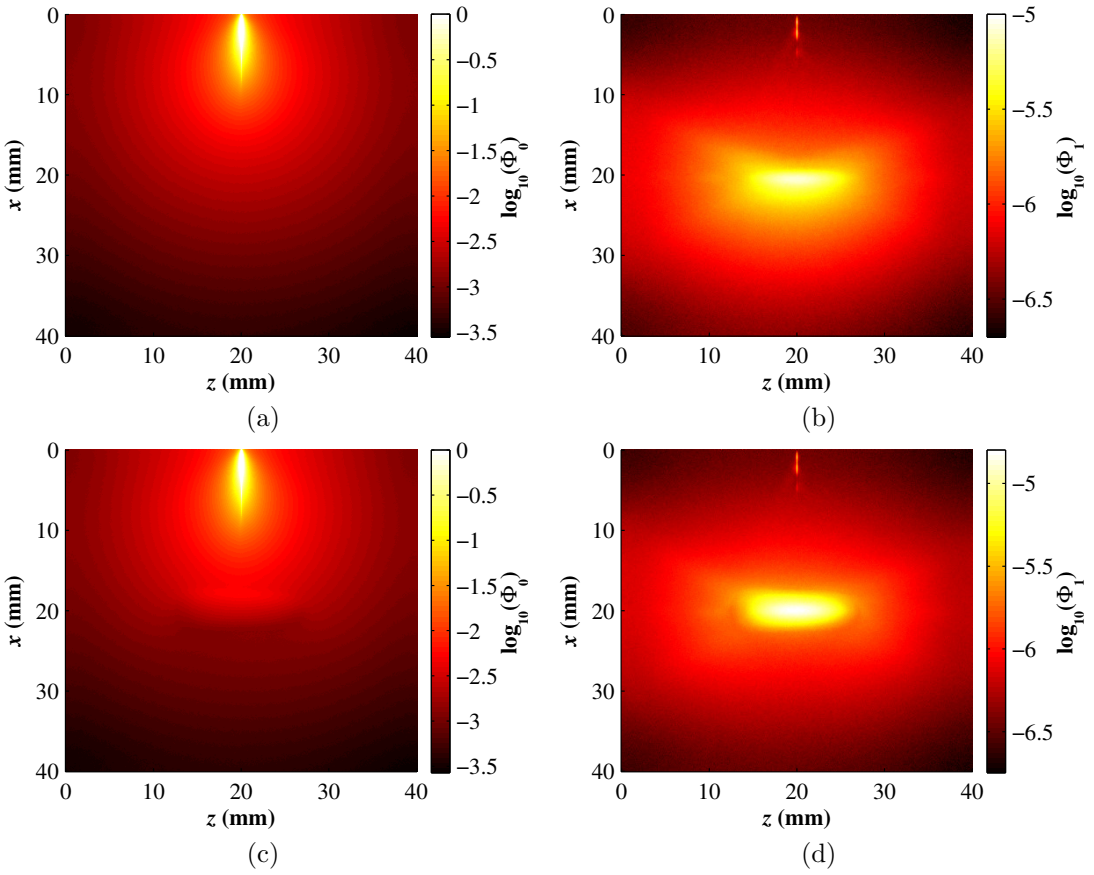

Figure 3·10: Unmodulated (a, c) and modulated (b, d) fluence rate distributions inside of unlesioned (a, b) and lesioned (c, d) chicken breast illuminated at 1064 nm nm and insonified with a peak pressure of 100 kPa at 1.1 MHz. The lesion was created by an exposure of a 6 MPa target peak pressure for 120 s. The physical properties of the medium can be found in Appendix B. 1 billion photons were used in this simulation to achieve smoother fluence rate distributions.

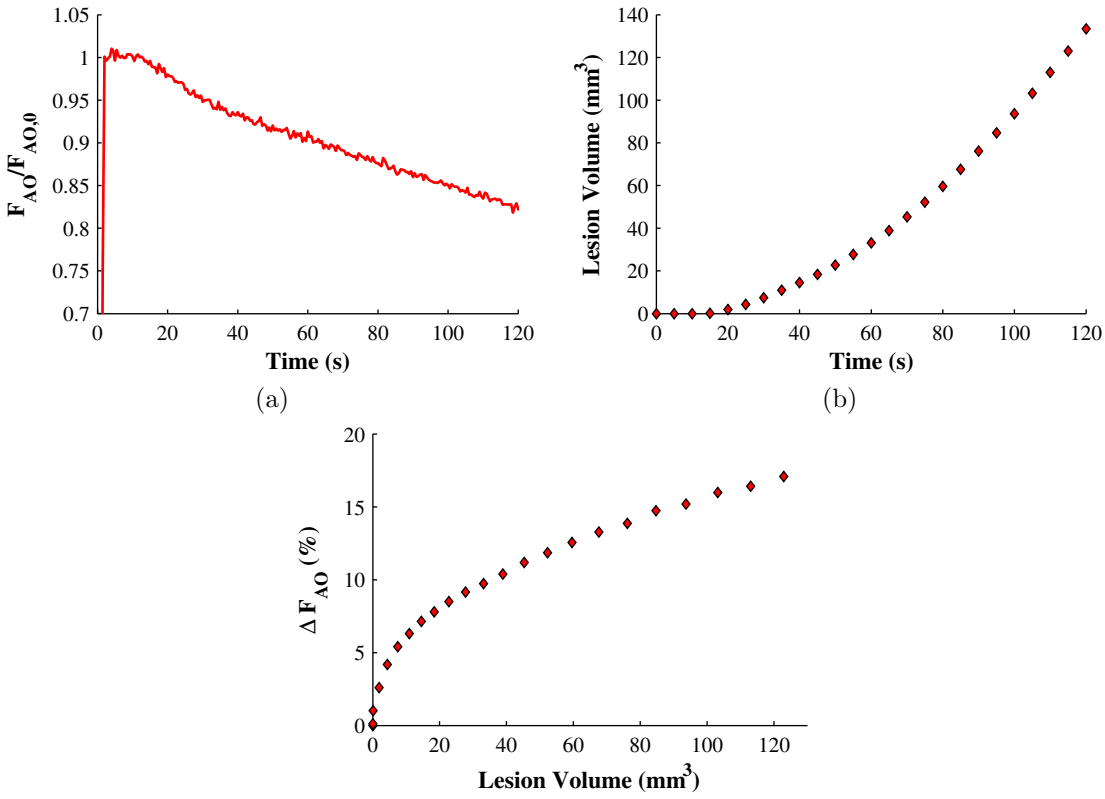

Figure 3·11: An example of the signals that are obtained from the integrated AO guided HIFU model. The chicken was exposed to a 6 MPa target peak pressure for 120 s, and the AO signal was calculated every 5 s, assuming an acoustic pressure amplitude of 100 kPa. (a) Normalized F_{AO} as a function of time with added noise based on the predicted SNR. (b) Lesion volume as a function of time. (c) Magnitude of the percentage change in F_{AO} as a function of lesion volume.

Fig. 1·8(b) we can see that the simulated signal closely matches the profile and the noise level of the signals measured during experiments. A more detailed comparison between the model and experimental data is presented in Chapter 4.

3.7.2 Restrictions and Hardware Requirements

When using each of the sub-models integrated into a single script, a number of restrictions and assumptions are placed upon the simulation. Each of these restrictions

and assumptions have been discussed in previous sections, but they are summarized here.

- The calculation of the acoustic field is linear. This limits the pressure amplitude used to calculate heating to regimes where non-linear propagation effects are not substantial. The acoustic field is also required to be monochromatic for the AO simulations.

- The thermal model requires the volume to be cubic. If the user wishes to perform an optical or AO simulation on a non-cubic medium, the medium may be truncated following the thermal simulation.

- Optical property changes are due only to heating, and not to any mechanical effects, such as those associated with cavitation or boiling.

- The AO model requires the voxel size, $l_v \ll \lambda_a$. Therefore, a grid spacing of 100 μm was used for every simulation in this work.

- The mean free scattering path, $l_s \gg \lambda_0$. For breast tissue, whose optical properties are presented in Table 3.4, $l_s = 1.3$ mm.

- The displacement of optical scatterers follow the displacement of the background medium in amplitude, phase, and direction.

- The ultrasound induced phase modulations are very small so that Eqs. 3.26 and 3.34 are valid. In order to safely avoid breaking this assumption, the peak pressure amplitude of all AO simulations was limited to 100 kPa.

- Polarization dependent effects are negligible in the AO MCX simulation, so that there is no interaction between photon packets.

Like all of the simulations presented in this thesis, the example presented here was executed on the Boston University engineering grid. Because of the fine grid spacing required by the AO code, a large amount of memory was required to perform the simulations. Typically, scripts such as the example shown in Appendix B were executed on a grid node with 32 GB of available RAM, and the AO code was executed on a Tesla C2070 graphics card (Nvidia, CA, USA) with 6 GB of available memory. It is recommended that a graphics card with at least 6 GB of available memory is used for all AO MCX simulations.

3.8 Summary

This chapter presented the relevant theory for every component of the AO guided HIFU model, and described the implementation and validation of each of the sub-models. All of the sub-models can be integrated into a single MATLAB script, and an example of such a script is given in Appendix B. The assumptions and the restrictions imposed upon the model were described throughout the chapter, but they are summarized in Section 3.7.2. In Chapter 4, the model is used to investigate important design considerations for an AO guided HIFU system, and a strategy is developed for the treatment of large volumes. In Chapter 5, the model is used to investigate the feasibility of AO guided HIFU in a clinical environment by evaluating its ability to guide the treatment of large volumes and by calculating expected SNRs in multiple organs.

Chapter 4

Design of an Optimized AO-Guided HIFU System

4.1 Overview

One of the specific aims of this work is to use the model presented in Chapter 3 to design an optimized AO guided HIFU system. Doing so involves investigating the effect of many different parameters, such as the illumination/detection geometry, the illumination wavelength, and the detection aperture size. Specifically, the objective is to design a system that maximizes the signal contrast of a lesion, while maintaing a reasonable SNR so that guidance can be performed in real time. Once the design parameters of the system are optimized, it is important to characterize how the AO system's signal changes as a lesion grows in volume – as this change in signal can be used as a predictor for lesion volume during HIFU guidance. Moreover, it is vital to understand how robust the signal is to changes in factors such as tissue thickness, lesion optical contrast, and lesion position. Knowing this will allow the user to make better predictions of lesion volume during HIFU treatments, and it will also determine the uncertainty of these predictions. In this chapter a model for an optimized AO guided HIFU system is presented, the robustness of its signal to changes in tissue and lesion properties is evaluated, a comparison is made between the AO signal and the purely optical signal – characterized by changes in total optical intensity. Moreover, this study is used as a vehicle for generating simulation results for comparison with

the experimental data from Lai et al. (2011), and possible causes of discrepancies between simulation and experimental results are discussed.

Unless otherwise stated, the simulation medium for all of the results presented in this chapter was a 40x40x40 mm^3 cube of chicken breast with a grid spacing of 100 μm immersed in water. For every case, the acoustic field was calculated for the HIFU source described in Section 3.1. The acoustic properties of the water are given in Table 3.1, the acoustic and thermal properties of the chicken breast are given in Table 3.2, and the optical properties of the chicken breast and lesion are given in Table 3.3. A time step of 100 ms was used for all thermal calculations. In every case, the tissue was insonified along the $+z$-axis and the pressure field co-registered with the lesion. Unless otherwise stated, the tissue was illuminated with a 1064 nm pencil beam positioned at the center of the $x = 0$ plane and launching 100 million photons directed in $+x$ (as shown by S_2 in Fig. 4·1(a)), and a 20-mm radius detection aperture was placed in the center of the tissue boundary at the maximum x dimension (as shown by D_4 in Fig. 4·1(a)). The 1064 nm optical wavelength was chosen to match the experimental arrangement of Lai et al. (2011), and the effect of the optical wavelength on the AO signal is discussed in Section 4.2.3. The detector properties used for each simulation are listed in Table 4.1.

Property	Value	Property	Value
η_{det}	0.004	A_d (cm^2)	0.2
α_c (cm^{-1})	1.8	γ' (cm^{-1})	0.5
L_c (cm)	0.7	γ'' (cm^{-1})	0

Table 4.1: The properties of the photorefractive crystal based detection system. The values were chosen to match the setup employed in Lai et al. (2011).

For thermal simulations, the focal pressure amplitude was set to 6 MPa so that a lesion the same size as the HIFU focal region could be formed in 60 s. This likely

violates the linear approximation used to calculate the acoustic field, but considering nonlinear effects was beyond the scope of this work. This exposure resulted in a lesion of approximately the same size as the HIFU focus ($\sim$30 mm^3) in the center of the volume, as shown in Fig. 1·4. For each AO simulation, the pressure amplitude was scaled down to a peak pressure of 100 kPa as discussed in Section 3.7 and the AO "signal contrast" of a lesion is evaluated. We define the AO signal contrast, ΔAO, of a lesion as:

$$\Delta\text{AO} = \frac{|F_{\text{AO},l} - F_{\text{AO},0}|}{F_{\text{AO},0}} \times 100\%, \tag{4.1}$$

where $F_{\text{AO},l}$ is the detected AO signal in the presence of a lesion and $F_{\text{AO},0}$ is the detected AO signal in the absence of a lesion. Therefore, the signal contrast is the change (in percentage) in the AO signal from its original value induced by a lesion.

4.2 Investigation of System Design Parameters

Three aspects of the AO system for HIFU lesion detection will be considered: (i) illumination/detection geometry, (ii) detection aperture size, and (iii) optical wavelength. In this section, these parameters are varied with the goal of maximizing the AO signal contrast of a lesion.

4.2.1 Illumination/Detection Geometry

The illumination/detection geometries available for a system will be target dependent. For organs with good optical accessibility, such as breast, many different geometries can be considered. However, other organs, such as liver, kidney, and bone, have limited optical access, e.g. only one or two sides of the organ. In this section we attempt to determine the optimal illumination/detection geometry for organs with good optical access, while also demonstrating the effect of only having access to one or two sides of an organ.

In order to examine the effect of the illumination/detection geometry on AO signal contrast, a 5-mm diameter spherical inclusion with the optical properties of a HIFU lesion is placed in the center of the otherwise homogeneous volume. A spherical inclusion is used here in place of a HIFU lesion to avoid effects caused by the lesion's asymmetry. As shown in Fig. 4·1(a), optical sources at 0° (S_1), 90° (S_2), and 180° (S_3) relative to the HIFU propagation are considered. For each of these sources, the AO signal contrast is evaluated for transmission, reflection, and side detection (D_1 – D_5 in Fig. 4·1). These nine different geometries are described in Table 4.2.

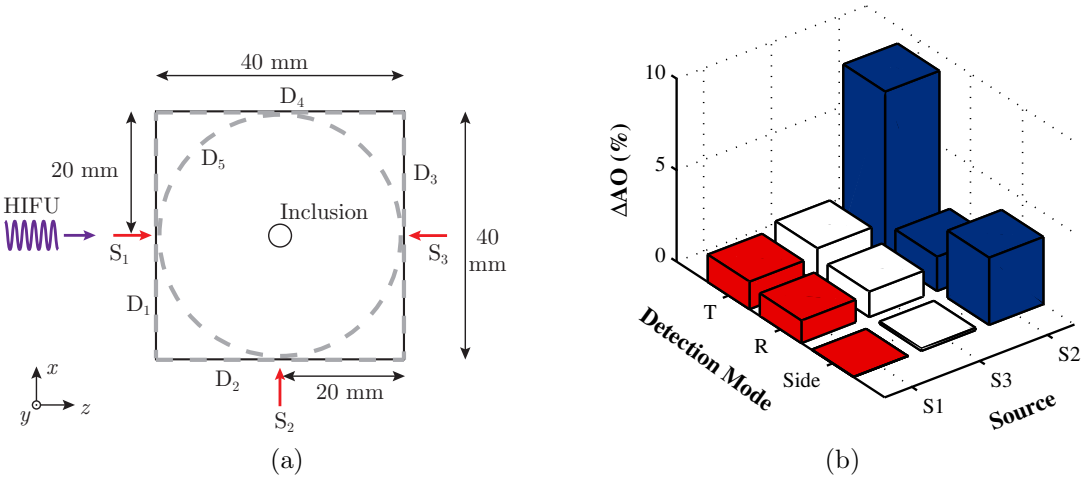

Figure 4·1: (a) A cross-section from the center of the volume showing the 5-mm diameter spherical inclusion. The locations of the five 20-mm radius circular detectors are shown with dashed grey lines and the locations of the three optical sources are shown with red arrows. (b) AO signal contrast of the spherical inclusion for the nine illumination/detection geometries described in Table 4.2. The bulk medium has the optical properties of chicken breast at 1064 nm, while the inclusion has optical properties of a lesion at 1064 nm, as defined in Table 3.3.

Although this geometry is optimal, it may be impractical to implement in some cases because it requires access to three sides of the tissue. While this is possible in organs with good optical accessibility, it may not be possible in others. If there is access to only two sides of the organ, the best contrast is observed when illuminating

Source	R	T	Side
$\mathbf{S}_1$	D_1	D_3	D_5
$\mathbf{S}_2$	D_2	D_4	D_5
$\mathbf{S}_3$	D_3	D_1	D_5

Table 4.2: The source/detector pair used for each geometry used in Fig. 4·1(b). The source and detector locations are depicted in Fig. 4·1(a).

opposite to the HIFU (S_3) and detecting in transmission (D_1). However, this geometry results in a loss of about 80% of the signal contrast when compared to the optimal geometry. Additionally, this geometry only demonstrates a marginally higher AO contrast than the configuration requiring access to only one side of the organ, which possesses significant practical advantages over a two-sided geometry.

4.2.2 Detection Aperture Size

The size of the detection aperture is important as it determines the amount of modulated and unmodulated light that is collected. Here, the effect of detection aperture size was investigated by illuminating the tissue with S_2 in Fig. 4·1(a) and modeling the detector as a disk of various radius in both transmission (D_4) and reflection (D_2) modes. Figure 4·2(a,c) shows the AO signal contrast and Fig. 4·2(b,d) shows the normalized AO signal magnitude of the $\sim$30 mm^3 HIFU lesion (shown in Fig. 3·5) as a function of the detection aperture radius. For transmission mode, it can be seen that using a smaller aperture results in a slightly better contrast – as it minimizes the collection of light that has accumulated phase-shifts outside of the HIFU focus – but it comes at the expense of the signal's magnitude. The magnitude of the AO signal is proportional to the radiant flux of the light collected by the aperture, therefore it is expected that it would decay exponentially with the size of the detection aperture. With a smaller aperture, significantly less light is collected, and as will be discussed

in detail in Chapter 5, the SNR will be adversely affected. Thus, while detecting in transmission it is generally advisable to employ an aperture that is as large as practically possible in order to collect as much transmitted light as possible. For reflection, it can be seen that there is an optimal detector radius for maximizing the AO signal contrast – which is equal to the length of the HIFU lesion along the acoustic propagation axis. However, as with transmission mode, using a larger aperture results in more light being collected and thus a gain in SNR.

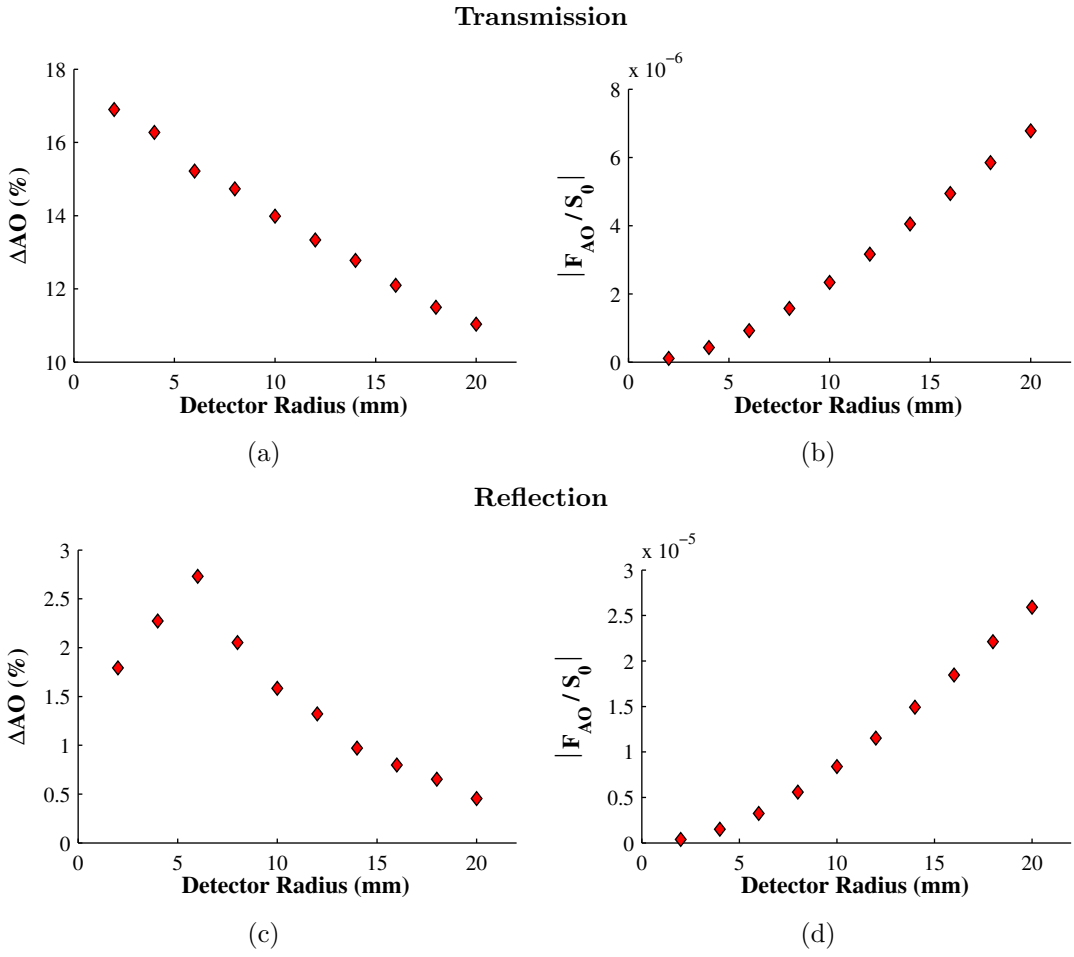

Figure 4·2: The AO signal contrast (a,c) and the detected AO signal normalized by the source power, S_0, (b,d) of a $\sim$30 mm^3 HIFU lesion as a function of the detection aperture radius for transmission (a,b) and reflection (c,d) detection.

4.2.3 Optical Illumination Wavelength

The final parameter considered was the impact of the illumination wavelength on the AO signal. As discussed in Chapters 2 and 3, the optical wavelength dictates how the light interacts with the tissue and the ultrasound. Additionally, the contrast in the optical properties between lesioned and unlesioned tissue is wavelength dependent. In standard diffuse optical imaging (without AO interactions), it is normally preferable to illuminate at an optical wavelength where the transport coefficient, $\mu_t' = \mu_s' + \mu_a$, is lowest (provided the optical contrast is sufficient at this wavelength). When μ_t' is minimized, the penetration depth of the light will be maximized. For an AO system, it is not as obvious that this is the best strategy because the wavelength of the light will also impact the AO phase modulations.

Table 4.3 shows the AO signal magnitude (normalized by S_0) and the signal contrast of the $\sim$30 mm^3 HIFU lesion for a variety of optical wavelengths. These wavelengths were chosen for either their biological relevance (minima or maxima in chromophore absorption spectra) or technical relevance (common laser wavelength). Examining the data, there appears to be a balance between high contrast and low signal level. The highest AO contrast occurs at 500 nm, but this wavelength results in the lowest detected radiant flux. The highest radiant flux is observed at 660 nm, but the AO contrast is second lowest at this point. Optimizing the wavelength therefore depends on the relative importance of flux and AO contrast.

Practically, the selection of the optical wavelength often depends on technical restrictions. For example, the use of a GaAs PRC for detection requires a 1064 nm source. In what follows, we employ 1064 nm because it is the operating wavelength of the GaAs crystal previously employed for the AO guided HIFU experiments (Lai et al., 2011) and it exhibits a good balance between detectable radiant flux and AO contrast. Additionally, it should also be noted that the fact that AO signal magnitudes

$\boldsymbol{\lambda}$ **(nm)**	500	550	576	660	800	940	975	1064
$\boldsymbol{\Delta}$**AO(%)**	25.7	22.6	16.8	9.6	8.18	9.99	16.3	10.9
$\frac{\lvert \boldsymbol{F}_{\mathbf{AO}} \rvert}{\boldsymbol{S}_0} \times \mathbf{10^{-6}}$	0.15	0.70	7.77	13.5	9.89	7.99	3.89	6.77

Table 4.3: The detected AO signal magnitude and the AO signal contrast of the ∼30 mm^3 lesion as a function of illumination wavelength. The optical wavelengths were chosen based on their biological or technical relevance. The optical properties of the bulk tissue and the lesion are given by the data presented in Chapter 2.

vary with the illumination wavelength means that multi-wavelength functional AO imaging or sensing is possible. Although not explored in this work, the potential of the technique has been investigated by Kim et al. (2007), and it is possible that it could be a potential tool for the functional imaging of HIFU lesions.

4.3 Robustness of the AO Signal

One advantage of a realtime AO guided HIFU system is the ability to use ΔAO as a feedback signal to control the volume of a lesion. In an ideal situation, the feedback signal would depend only on the volume of a lesion, and not other factors such as the location of the lesion, optical contrast, the thickness of the tissue, or the HIFU pressure amplitude used to create it. Unfortunately, this is not the case. In this section, the AO signal change is evaluated as a function of lesion volume for the case of a lesion in the center of a chicken breast tissue with the goal of determining how robust ΔAO is to changes in tissue thickness, lesion optical contrast, and lesion position. Additionally, in characterizing ΔAO as a function of lesion volume, simulations are compared to experimental data (Lai et al., 2011) in order to validate the performance of the model.

4.3.1 Signal Dependence on Lesion Volume and Tissue Thickness

Lai et al. (2011) showed that for the case of a lesion in the center of chicken breast, of thicknesses 15–30 mm, the AO signal contrast of a lesion with a given volume is approximately independent of the tissue thickness and HIFU pressure amplitude. Here, the experimental arrangement is mimicked for tissues of thicknesses 20–30 mm and Fig. 4·3 shows ΔAO as a function of lesion volume for the geometry described in Section 4.1. That is, the tissue is insonified along the z-axis, illumination is along the x-axis, and detection is in transmission mode. Here thickness variation is in the x dimension, and it is equal to the source-detector separation distance. As Fig. 4·3 demonstrates, the simulated signal contrast of a given lesion size is in fact not independent from the tissue thickness. It can be seen that ΔAO increases with lesion volume, but that the magnitude of the change is reduced as tissue thickness increases.

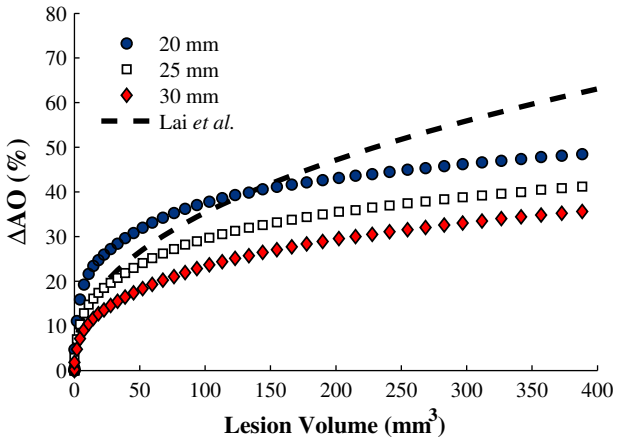

Figure 4·3: The AO signal contrast as a function of lesion volume for tissues of 20 (blue circle), 25 (white box), and 30 (red diamond) mm thicknesses. The dashed black line is a best-fit derived from experimental measurements of samples of thicknesses 15–30 mm (Lai et al., 2011). The simulation geometry and properties are described in Section 4.1. The lesions are computed using a 6 MPa target peak pressure for the acoustic and thermal simulations, but the peak pressure is reduced to 100 kPa for the AO simulations.

Additionally on Fig. 4·3, experimental data from samples of thicknesses 15–30 mm is overlaid. The predictions bracket the experimental data for volumes less than 150 mm^3 and suggest that the model captures the physical process over this range. For larger volumes the simulations predict the response to saturate and suggest less sensitivity to lesion volume, whereas the experimental data continues to increase. One reason for this may be the large difference in pressure amplitudes between the AO model and the experiments. As previously discussed, the assumptions used to calculate phase modulations limit the peak pressure of the model to 100 kPa, while peak pressures of up to 10 MPa were used in experiments. In the model, the pressures outside of the HIFU focus are too low to significantly contribute to each photon packet's total phase shift (except for in some pre and post-focal locations). Alternatively, during experiments the pressure amplitudes outside of the focus may still be quite high and could in fact contribute significantly to the total phase shift of each optical path. This would result in the AO signal being more sensitive to optical changes outside of the HIFU focus, thus inducing a larger ΔAO for larger lesion volumes. Another possible explanation for the discrepancy between the data is that the optical properties of large HIFU lesions – where exposure times are longer and both mechanical stresses and temperatures are likely to be higher – are different than those used in the simulations.

4.3.2 Signal Dependence on Lesion Optical Contrast

Next, the effect of variability in the optical contrast of a lesion is considered. Clearly, lesions are expected to exhibit different optical contrast in different tissues, but there may also be less predictable sources of variability such as lesion location, body temperature, patient age and gender, hydration levels, blood flow, etc. Looking at Fig. 2·11, where μ_s' is plotted as a function of thermal dose for five *ex vivo* chicken breast samples, it can be seen that the standard deviations of the measurements are $\sim$20%

of the average values. It is possible, and perhaps likely, that these standard deviations would be even higher *in vivo*. For this reason, it is very important to know how robust the AO signal is to variability in the optical contrast between lesioned and unlesioned tissue.

Here, the optical contrast of the lesion, C, is defined as:

$$C = \frac{(\Delta\mu)_{\max}}{\mu_0}, \tag{4.2}$$

where $(\Delta\mu)_{\max}$ and μ_0 are defined in Eq. 3.15. In Fig. 4·4, ΔAO is plotted as a function of a given lesion volume is affected as the optical contrast of a lesion is perturbed. The simulated optical contrast is changed by adjusting the absorption and scattering coefficients of the lesion equally, while the optical properties of the unlesioned medium stay fixed. Figure 4·4(a) shows ΔAO as a function of lesion volume for lesions with the average measured contrast at 1064 nm, C_{avg}, (black diamonds), $C_{\text{avg}}\pm25\%$ (blue line), and $C_{\text{avg}}\pm50\%$ (red line), which covers 2.5 standard deviations. The average measured contrast is derived from the data presented in Table 3.3.

Figure 4·4(b) shows ΔAO as a function of the normalized optical contrast of a single $\sim$30 mm^3 lesion. As the data shows, a doubling of the optical contrast of a $\sim$30 mm^3 lesion results in a shift of ΔAO by less than 5%. While this seems like a small shift in response, Fig. 4·4(a) demonstrates that for a $\sim$30 mm^3 lesion with average optical properties, a 25% uncertainty results in a prediction of a lesion volume between $\sim$20-45 mm^3, and a 50% uncertainty results in a prediction of a lesion volume between $\sim$8-75 mm^3. As the lesion volume increases, the uncertainties become even greater. For example, a 25% uncertainty in the optical properties of a 100 mm^3 lesion results in a volume prediction between $\sim$75-145 mm^3, and a 50% uncertainty results in a prediction between $\sim$65-250 mm^3. Thus, if a high level of accuracy is required for predictions of lesion volume, it may be advisable to only use AO guidance for lesion

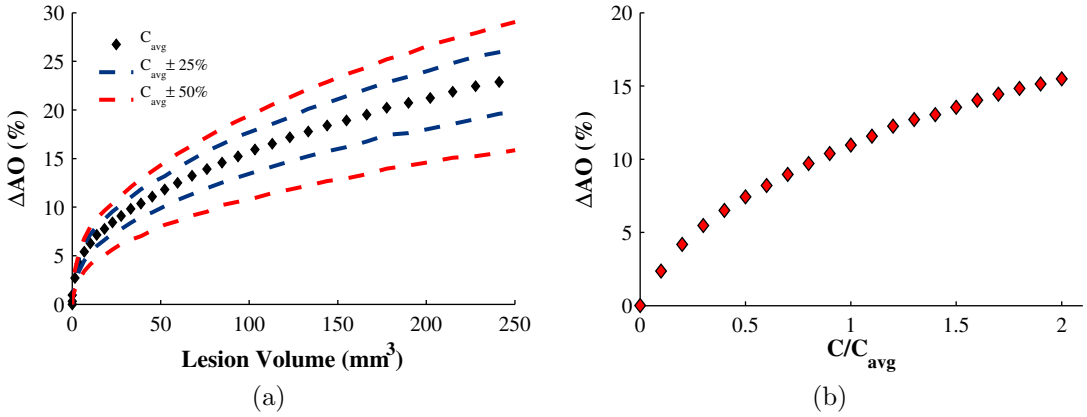

Figure 4·4: (a) AO signal contrast as a function of lesion volume for lesions with C_{avg} (black diamonds), $C_{\text{avg}} \pm 25\%$ (blue line), and $C_{\text{avg}} \pm 50\%$ (red line). (b) AO signal contrast of the $\sim$30 mm^3 lesion in the center of the volume as a function of its normalized optical contrast, C/C_{avg}. The simulation geometry and properties are described in Section 4.1. Absorption and scattering are varied equally to achieve a desired optical contrast.

volumes on the order of the HIFU focus or smaller.

4.3.3 Signal Dependence on Lesion Position

The final lesion parameter affecting the AO signal investigated was the location of the lesion relative to the source and the detector. If ΔAO is not independent of location, a position-based adjustment must be applied to the prediction of lesion volume during HIFU. Figure 4·5 shows the impact of moving the lesion all three directions, the x (optical source), y (lateral), and z (HIFU source), on ΔAO. As the lesion is moved, the acoustic field moves with it so that the acoustic focus is always co-registered with the lesion. As the lesion is moved close to the optical source (along x), the AO detection sensitivity increases proportionally with the light fluence. As the lesion moves away from the center of the volume in y and z, the AO detection sensitivity decreases with the fluence of the light. The difference observed between moving the lesion in z as opposed to moving it in y is due to the lack of symmetry

in the acoustic field along its propagation axis. It should be noted that if a wider beam or multiple sources were used then the lesion position along y and z would have a reduced effect on the signal contrast, but its position along x would remain an important parameter. Nevertheless, the lesion position's effect on the AO signal is significant, but it is something that can be predicted by estimating the fluence in the HIFU focus, and it should be compensated for during AO guided HIFU.

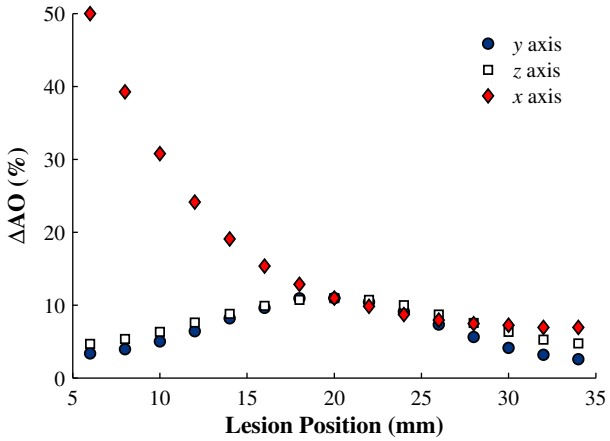

Figure 4·5: AO signal contrast of the ∼30 mm^3 lesion as its position within the volume is changed. The described lesion position is the location of the center of the lesion as it is scanned along the x (red diamonds), y (blue circles), and z (white squares) axes. The x axis is the optical source axis and the z axis is the HIFU propagation axis. The simulation geometry and properties are described in Section 4.1.

4.4 The AO Signal vs. the Optical Signal

Currently employed AO detection methods are technically difficult to implement, and are often the most expensive and limiting components of an AO system. Additionally, because the fluence of modulated light is orders of magnitude less than the fluence of unmodulated light, the AO signals are much smaller than the total optical intensity signals and thus have significantly worse SNR. Because of the technique's limitations, there needs to be just cause to employ AO sensing as opposed to simply using total

intensity changes as a feedback mechanism for HIFU.

In an attempt to address this issue, the change in the AO signal and the change in the total optical intensity signal were evaluated as a function of lesion volume for the case of a chicken breast illuminated and insonified under the exposure conditions described in Section 4.1. Standard optical sensing is defined as measuring total optical intensity changes, calculated based on Eq. 3.47. Figure 4·6 shows the increase in both AO and optical intensity changes as a function of lesion volume and demonstrates the largest benefit of using AO sensing (red diamonds) over standard optical sensing (blue circles) is that the signal is significantly more sensitive to the lesion formation, especially when the lesion is within the HIFU focus ($<\sim$30 mm^3). The higher sensitivity displayed by the AO signal was expected, as the vast majority of the modulated light is generated in the HIFU focus, where the lesion forms.

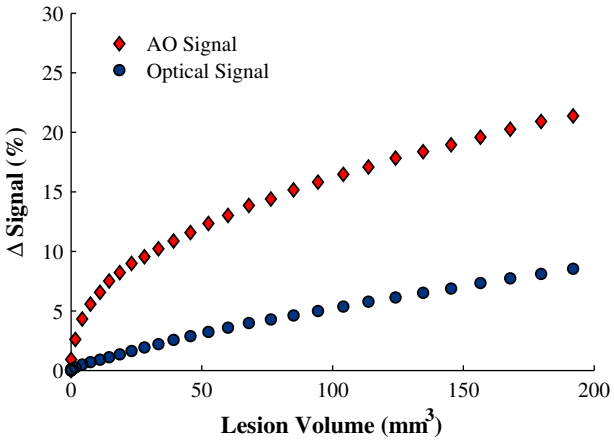

Figure 4·6: A comparison between the AO (red diamonds) and total optical intensity (blue circles) signal changes as a function of lesion volume. The total optical intensity is calculated based on Eq. 3.47. The simulation geometry and properties are described in Section 4.1.

Another important property of the AO signal is that it is very sensitive to optical changes in the HIFU focus (where the lesion is forming), but unlike the optical signal it should not be very sensitive to optical changes outside of the focus. If the optical

properties outside of the focus change during the HIFU exposure – due to changes in blood flow, tissue movement, etc. – the AO signal should not be significantly affected. Conversely, these optical property changes could induce large changes in the measured optical intensity signal – on the order of or larger than the changes induced by lesion formation – which would hamper the ability of a purely optical system to predict lesion volume based on total intensity changes. This effect has previously been modeled and confirmed for the case of an optical absorber moved around a medium for both optical and AO sensing in transmission and reflection detection (Powell and Leung, 2012).

As previously mentioned, the enhanced signal contrast obtained by using AO sensing does not come without a cost. Not only are AO signals technically more difficult to measure, and AO detection methods are expensive to implement, but more importantly the signals have significantly lower SNR than the total optical intensity signals. In Chapter 5, the expected SNR of the AO signals are analyzed in an attempt to address the clinical viability of AO sensing in different organs.

4.5 Summary and Conclusions

In this chapter, a number of different design parameters were investigated with the goal of developing an optimized AO guided HIFU system: illumination/detection geometry, detection aperture size, and optical wavelength selection. It was found that an optimally designed AO guided HIFU system should illuminate the target organ at 90° relative to the HIFU propagation with an optical wavelength which exhibits minimal absorption in tissue, and that signal detection should be performed in transmission mode using a detection aperture that collects as much light as possible. Unfortunately, this requires access to three sides of the target organ. Therefore, the optimal organs for AO guided HIFU are those with good optical accessibility, such as

the breast.

Using this optimally designed system, the AO signal contrast changes was evaluated as a function of lesion volume for tissues of different thicknesses. This study was used as an opportunity to compare the simulation results to the experimental data collected by Lai et al. (2011). It was determined that the modeling results agree very well with experimental data while the lesion is within the HIFU focus ($\leq\sim$30 mm^3). As the lesion grows outside of the HIFU focus, the simulated signal asymptotes while the experimental data continues to increase. The cause of this divergence is likely due to the significantly higher pressures present in experiments.

Next, the robustness of the AO signal contrast to changes in the optical contrast and position of the lesion was examined. It was found that variations in the optical properties of a lesion cause significant uncertainties in the prediction of lesion volume based on ΔAO, and that these uncertainties are greater for larger lesions. Therefore, accurate lesion volume predictions made based on AO sensing can only be made when lesions are small (on the order of the HIFU focus), or optical property variabilites are well known. It was also found that the signal contrast scales with the local light fluence, and that in deploying an AO sensing system for HIFU it would be necessary to account for tissue thickness and lesion location in order to account for this. Finally, it was shown that the AO signal contrast is more sensitive to lesion formation than the optical signal contrast (based on total optical intensity changes), and a discussion was presented which argued why AO sensing is better to use for HIFU guidance than purely optical sensing.

Chapter 5

Clinical Viability of AO Guidance for HIFU

5.1 Overview

The final specific aim of this thesis is to use the model presented in Chapter 3 to assess the clinical viability of an AO guided HIFU system. In order for a HIFU guidance system to be viable in a clinical scenario it must be robust to variations in lesion location and properties, it must be able to guide the ablation of clinically relevant volumes (larger than one single lesion), and it must be able to perform real-time guidance of lesion formation in healthy and cancerous tissues *in vivo*. In Chapter 4 an optimal system design for guiding HIFU using AO sensing was presented, and the robustness of the signal to changes in lesion and tissue properties was evaluated. It was shown that although the system's signal is not completely insensitive to changes in tissue thickness and lesion location, or to variabilities in a lesion's optical contrast, the system should still be able to predict lesion volumes with reasonable accuracy (with the degree of accuracy depending upon the size of the lesion).

In this chapter, the clinical viability of the AO guidance system is further evaluated by assessing its effectiveness in guiding the ablation of large volumes, and the feasibility of performing real-time guidance of single lesion formation is evaluated for multiple tissue types. In doing so, the SNR of the AO signal is calculated in breast, prostate, brain, and liver tissues, and we identify scenarios where this SNR is suf-

ficient to allow HIFU guidance. Finally, the viability of real-time AO guidance for ablating tumors is assessed by simulating the SNR for single lesions created inside of a model breast tumor.

5.2 Guiding the Ablation of Large Volumes

An important characteristic of a HIFU monitoring technology is its ability to guide the treatment of large volumes. In practice, ablating clinically relevant volumes requires the HIFU transducer to be strategically scanned – either continuously, forming one large lesion, or intermittently, forming an array of small lesions (ter Haar, 2012). In this section, the effectiveness of AO sensing for guiding the ablation of large volumes is evaluated by employing the latter approach. As discussed in Section 4.3.3, the change in the AO signal with respect to lesion volume is dependent upon the position that the lesion is created in. Therefore, as the HIFU transducer is scanned, the sensitivity of the AO feedback signal is expected to change with position. However, when creating an array of multiple lesions, it is also critical to determine if pre-existing lesions will even further affect the sensitivity of the AO feedback signal, resulting in the same ΔAO being induced by lesions of variable sizes.

In this simulation, an array of nine lesions was created in a simulation medium with the same geometry and properties described in Section 4.1. The medium was a 40x40x40 mm^3 cube of chicken breast immersed in water, with a grid spacing of 100 μm and a time step of 100 ms used for all thermal simulations. The tissue was illuminated with a 1064 nm pencil beam, positioned at the center of the $x = 0$ plane, launching 100 million photons directed normal to the HIFU propagation in $+x$ (as shown by S_2 in Fig. 4·1(a)), and a 20-mm radius detection aperture was placed in the center of the tissue boundary at the maximum x dimension (as shown by D_4 in Fig. 4·1(a)). The tissue was exposed with a target peak pressure of 6 MPa in water

until ΔAO reached 10%, then the HIFU was turned off, the tissue was allowed to cool for 30 seconds, and the HIFU transducer was moved to the next position. The acoustic and thermal properties of the chicken breast are given in Table 3.2, and the optical properties of the chicken breast and lesion are given in Table 3.3. Although the thermal simulations were performed with 100 ms time steps, the AO feedback was only calculated every 5 seconds in order to maintain a reasonable computational time.

Figure 5·1 shows the resulting treatment volume after creating the lesion arrays starting distal (a) and proximal (b) to the light source, which projects downwards from the "top" of the lesion array. In Fig. 5·1(a) the lesions were created by starting in the lower right and scanning in $-y$ and $-x$ respectively, while in Fig. 5·1(b) they were created by starting in the upper right and scanning in $-y$ and $+x$ respectively. The isosurfaces correspond to the volume where the optical properties of the lesion reached $(\Delta\mu)_{\max}$.

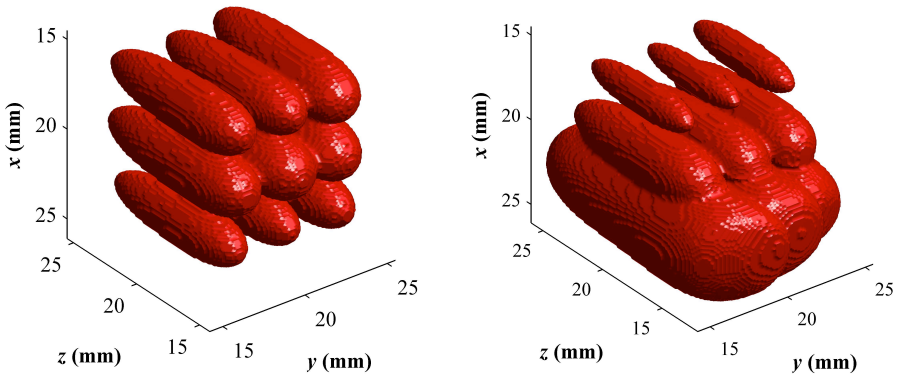

Figure 5·1: Lesions arrays created using ΔAO = 10% as a feedback condition to stop heating. Considering illumination from the "top", the arrays were created beginning distal (a) and proximal (b) to the illumination source.

As Fig. 5·1 demonstrates, there is clearly an optimal strategy to employ while creating lesion arrays to ablate large volumes using AO guidance with transmission

detection. This strategy is to begin creating lesions distal to the source first, and then to move towards it. This strategy can be explained by examining Fig. 5·1(b), where the exposure began proximal to the source. When lesions are first created proximal to the source, the fluence in the focus is higher and the change in the AO signal is more sensitive to lesion volume (as demonstrated in Fig. 4·5). Thus, a smaller lesion is required to produce the same signal change close to the source than elsewhere in the volume. As the treatment moves away from the source, the pre-existing lesions cause a shadowing effect and less light reaches the HIFU focus than otherwise would, resulting in the AO signal being even less sensitive to lesion volume. Thus, as the HIFU treatment volume moves away from the light source the shadowing effect and the increasing distance from the light source compound, and the sensitivity of the AO signal with respect to lesion volume becomes lower, resulting in larger lesion volumes. Alternatively, if the exposure begins distal from the source, there is no shadowing effect when creating the first row of lesions. As the treatment moves closer to the source, the pre-existing lesions cause less modulated light to reach the detector, but this is offset by the increased sensitivity of the AO signal caused by the higher fluence present in the HIFU focus. Therefore, at least in the case of chicken breast, these two effects are balanced and nine lesions of approximately the same volume are created.

Although it should be possible to employ this strategy to ablate large volumes, the results in Fig. 5·1 suggest that AO guidance is sensitive to the optical properties of the surrounding tissue. Not only could the feedback signal be affected by pre-existing lesions, but it could also be affected by nearby optical inhomogeneities in the tissue. Therefore, in practice it may be necessary to image the area surrounding the treatment volume prior to ablating. Quantitative AO imaging (Powell and Leung, 2013b, 2014) has recently been proposed as a method for measuring the optical properties of tissue *in situ*, and could potentially be used prior to AO guided HIFU surgeries in order to

predict the response of ΔAO to lesion volume. Nevertheless, these results demonstrate that AO sensing as the potential to guide the ablation of large volumes with HIFU.

5.3 Signal to Noise Ratio of the AO Guidance System

Although signal robustness and the ability to guide the ablation of large volumes are critical elements of a HIFU guidance technology, perhaps the most essential feature of a system is its ability to perform real-time guidance at depth *in vivo*. For performing real-time AO sensing, the signal-to-noise ratio (SNR) of the system is a critical parameter. The SNR of an optical signal is defined as the ratio of the power of the detected signal, P_{signal}, to the power of the noise present in the signal, P_{noise}:

$$\text{SNR} = \frac{P_{\text{signal}}}{P_{\text{noise}}}. \tag{5.1}$$

In this section, the system characteristics of Lai (2010) are used to predict the SNR of the AO signal used for guiding the formation of single HIFU lesions in different tissues. The PRC-based detection system uses a low-noise and high-gain avalanche photodetector (APD, Model APD50-AD5000-9-TO, Pacific Silicon Sensor, CA, USA), whose 5-mm diameter active area exhibits a pre-amplified responsivity of approximately 1.25×10^5 V/W at 1064 nm with a low noise read-out. The output of the APD is further preamplified, low-pass filtered, and fed into a lock-in amplifier in order to improve the SNR of the system and make real-time sensing possible. In Sections 5.4 and 5.5 this methodology is used to predict the SNR in a variety of biological tissues.

5.3.1 Noise Power Prior to Lock-In Amplification

When light impinges a photodetector, a photocurrent is generated which is linearly proportional to the radiant flux (power) of the light. Simultaneously, variances in this current are generated by noise sources. In the signal produced by a photodetector, the

dominant noise sources are thermal noise and shot noise (Kingston, 1995). Thermal noise, which is independent of the power of the detected light, is caused by both the thermal excitation of photocarriers and the thermal motion of electrons in circuitry. In low-noise, sensitive photodetectors, such as the APD employed by Lai (2010), thermal noise is only important at low radiant fluxes.

Shot noise, which is caused by the discrete particle nature of photons, arises from two different physical processes – fluctuations in power at the output of a laser and the randomness of photon absorption events in a photodetector. However, in practice these two phenomena are indistinguishable in the signal output by a photodetector (Van Der Ziel, 1970). Nevertheless, both of these processes induce a variance in a photocurrent which increases linearly with the power of the detected light. Thus, above a particular threshold in the detected optical power, the noise power of the signal increases linearly with the radiant flux. In this regime, the detection is said to be shot noise limited.

When light with a wavelength of 1064 nm is incident upon the 5-mm diameter active area of the APD, a voltage is generated from the APD pre-amplifier with a responsivity of 1.25×10^5 V/W, where the termination impedance is 50 Ω. The signal is then further preamplified (20 dB) and low-pass filtered (500 kHz, 24 dB/octave) using an active filter (Model 3940, Krohn-Hite, MA, USA). (To perform real-time sensing, the signal is then sent to a lock-in amplifier, as discussed in Section 5.3.3). The noise power of the signal at the output of the active filter, P_{noise}, calculated from the variance its voltage (Lai et al., 2011), is shown in Fig. 5·2 as a function of the incident radiant flux, F_{inc}. As the data shows, the signal is shot noise limited above a radiant flux of ∼6.7 nW. Below this threshold, the system is dominated by thermal noise sources. By applying a linear fit to the shot noise limited data, we can predict the noise power of the detected electrical signal (nW) as a function of an incident

radiant flux (nW) greater than 6.7 nW:

$$P_{\text{noise}} = 92.4 + 0.8(F_{\text{inc}} - 6.7). \tag{5.2}$$

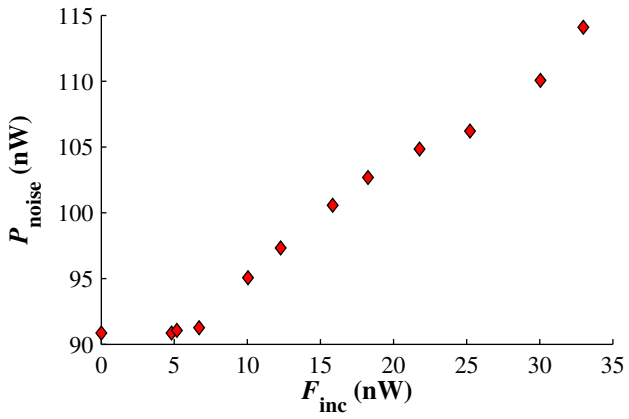

Figure 5·2: The noise power of the signal at the output of the active filter as a function of incident radiant flux.

As previously discussed in Section 3.6.1, the optical intensity at the output of the PRC can be split into multiple components, with an I_{SE}^{N} component responsible for the noise and an I_{SE}^{DC} component responsible for the AO signal. The I_{SE}^{N} component of the signal represents the total intensity of the beam in the absence of ultrasound modulations, and is thus responsible for the total radiant flux incident on the detector. Therefore, for all of the simulations presented in this chapter, the total radiant flux incident on the detector, equal to the product of I_{SE}^{N} and the area of the active area of the APD, A_{det}, is calculated as:

$$F_{\text{inc}} = \eta_{\text{det}} S_0 \exp(-\alpha_c L_c) \exp(2\gamma' L_c) \sum_s W_s. \tag{5.3}$$

Accordingly, the noise power of the detected signal is calculated using Eq. 5.3 as an input into the fit given in Eq. 5.2.

5.3.2 Signal Power and SNR Prior to Lock-In Amplification

For the purposes of AO guided HIFU, the signal that is used as a feedback mechanism to predict lesion volumes is the change in the AO radiant flux, F_{AO}, induced by the formation of a lesion. Given F_{AO} with and without the presence of a lesion, the power of the signal is calculated as:

$$P_{\mathrm{signal}} = \frac{(R_{\mathrm{det}} F_{\mathrm{AO},l} - R_{\mathrm{det}} F_{\mathrm{AO},0})^2}{Z_{\mathrm{load}}}, \tag{5.4}$$

where R_{det} is the responsivity of the APD (1.25×10^5 V/W), Z_{load} is the output impedance of the APD (50 Ω), and the l and 0 subscripts refer to signals calculated with and without the presence of a lesion, respectively. Therefore, SNR of the preamplified and filtered APD signal is calculated as the ratio of Eq. 5.4 and Eq. 5.2.

5.3.3 SNR After Lock-In Amplification

In practice, the SNR at the output of the active filter is far too low to perform real-time AO sensing for any application. In order to improve the SNR and make real-time sensing feasible, a lock-in amplifier is used (Lai et al., 2011). Lock-in amplifiers use a technique known as phase-sensitive detection to isolate a signal component of a very small AC signal at a specific reference frequency embedded in a large amount of wideband noise (Meade, 1983). The output of the lock-in amplifier is a DC signal, whose value is proportional to the RMS value of the AC input signal at the reference frequency, and whose noise level is determined by the bandwidth of the amplifier's low-pass filter. In order to convert the signal produced by F_{AO} into an AC signal, the HIFU is 100% amplitude modulated at 50 Hz, yielding an AC signal which oscillates between F_{inc} and $F_{\mathrm{inc}} + F_{\mathrm{AO}}$ at a frequency of 50 Hz (see Fig. 1·8(a)).

The SNR improvement induced by the lock-in amplifier can be expressed as:

$$\mathrm{SNR}_{\mathrm{out}} = \mathrm{SNR}_{\mathrm{in}} \sqrt{\frac{B_{\mathrm{in}}}{B_{\mathrm{LPF}}}}, \tag{5.5}$$

where B_{in} is the equivalent noise bandwidth of the input signal, and B_{LPF} is the equivalent noise bandwidth of the lock-in amplifier's low-pass filter, calculated based on the integration time constant and filter slope selected by the user. Given the 565 kHz equivalent noise bandwidth of the input signal, and the 30 ms integration time constant and 12 dB/octave roll-off employed by Lai et al. (2011), the lock-in amplifier improves the SNR of the system by ∼25.7 dB.

5.3.4 Pressure Dependence of the SNR

The acoustic pressure amplitude used during HIFU has a significant impact on the AO signal. It has previously been demonstrated that at low pressure amplitudes, the ultrasound induced phase shifts are linearly dependent upon p_0, and thus F_{AO} has a Bessel function dependence on p_0 (Lai et al., 2009). Conversely, the component of the signal which is responsible for noise, F_{inc}, is independent of the acoustic pressure. Therefore, the SNR has an approximately Bessel squared dependence upon the pressure magnitude.

As explained in Sections 3.5 and 3.7.2, the peak acoustic pressure amplitude in all of the AO simulations performed in this dissertation is limited to 100 kPa. However, in reality peak pressure amplitudes of up to 10 MPa may be used during AO guided HIFU (Lai et al., 2011). In order to account for the SNR enhancement generated by high pressure amplitudes, pressure dependent experimental data (Lai et al., 2009) measured in a homogeneous, non-absorbing phantom ($\mu_s' = 7$ cm^{-1}) was fit with an equation of the form:

$$\mathrm{SNR}(\mathrm{p_0}) = \left(\kappa \left[1 - J_0\left(\beta p_0\right)\right]\right)^2, \tag{5.6}$$

where κ and β are fitting coefficients, and p_0 is the peak pressure amplitude. Equation 5.6 is derived from an approximation of the AO signal, which assumes that the net ultrasound induced phase shift is linearly dependent upon the pressure amplitude of the ultrasound field, and that the phase shifts are small enough to be approximated by a Bessel function. As Fig. 5·3 demonstrates, where SNR(p_0)/SNR(100 kPa) is plotted as a function of p_0, this approximation causes a ringing of the fit at high peak pressures. Nevertheless, it supplies an approximate pressure dependence of the AO signal's SNR, which appears to saturate around 2 MPa. At 1.1 MHz, a pressure-based enhancement of 40 dB is predicted, and so this was applied to all of the results presented in this chapter.

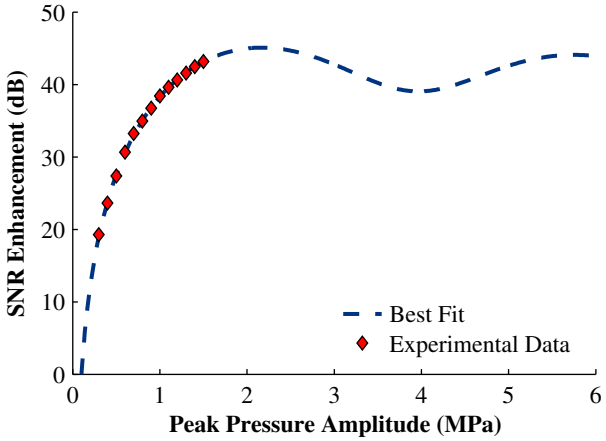

Figure 5·3: Pressure dependence of the AO signal's SNR relative to the SNR at 100 kPa. The experimental data (Lai et al., 2009) is measured in a homogeneous, non-absorbing phantom ($\mu_s' = 7$ cm^{-1}) and is fit with Eq. 5.6.

5.4 Feasibility in Organ Models

In order to investigate the feasibility of AO guided HIFU at different depths in multiple tissues, the SNR of the AO signal was calculated in media with the optical properties of breast, prostate, liver, and brain tissues (white and grey matter). For

each simulation, the medium was a cuboid with dimensions of 40 mm in y and z, and a thickness ranging from 20-60 mm in x. As in Section 5.2, the medium was illuminated in the center of the $x = 0$ plane with a 1064 nm source directed in $+x$ (normal to the HIFU propagation), and unless otherwise stated detection was performed in transmission with a 20-mm radius detection aperture centered in the middle of the maximum x plane. In order to save computational time and avoid uncertainties brought on by variabilities in the thermal properties of different tissues, each HIFU lesion was approximated as an ellipsoid with a 2:1 aspect ratio and a major axis along z, located in the center of in each volume. Thus, by varying the thickness of the tissue both the source-detector separation and the depth at which the lesion was created were varied. For every simulation, the HIFU source was directed along the $+z$ axis, and its focus was aligned with the center of the volume.

All of the optical properties for the tissues were taken from measurements of human tissues (Yaroslavsky et al., 2002; Germer et al., 1998; Newman and Jacques, 1991; Koelzer et al., 1995), however the optical properties of some lesioned tissues were not available in literature. Therefore, while the optical properties of lesioned brain (Yaroslavsky et al., 2002) and liver (Germer et al., 1998) tissues were taken from measurements in human tissue after exposure to heated saline baths, the optical properties of lesioned prostate were based on the contrast of lesioned rat prostate (Skinner et al., 2000). Furthermore, because no measurements of any type of lesioned breast tissue were available in literature, the lesioned breast properties were calculated based on the average contrast exhibited by the other four tissues. All of the optical properties shown in Table 5.1 are approximations of what should be expected *in vivo*, where factors such as hydration level and blood coagulation may play prominent roles. Therefore, the results presented in this section should be taken as qualitative and approximate rather than absolute. The acoustic properties are shown in Table

5.2.

Tissue	Native		Lesioned	
	μ_a (cm^{-1})	μ_s' (cm^{-1})	μ_a (cm^{-1})	μ_s' (cm^{-1})
Breast	0.042	8.4	0.061	20.9
Prostate	0.40	9.3	0.90	37.4
Grey Matter	0.5	5.7	1.1	24.0
White Matter	1.0	32.6	1.1	40.7
Liver	0.5	16.9	0.2	20

Table 5.1: The optical properties at 1064 nm of each of the tissues examined in this chapter, derived from *ex vivo* measurements presented in literature. The refractive index of all tissues was assumed to be 1.4, and the anisotropy coefficient was approximately 0.9 for every tissue.

Tissue	ρ_0 (kg/m^3)	c_a (m/s)	α (Np/m)
Breast	1020	1510	9.50
Prostate	1030	1561	9.88
Grey Matter	1030	1550	10.5
White Matter	1030	1550	10.5
Liver	1060	1595	6.45

Table 5.2: The acoustic properties of each of the tissues examined in this chapter (Duck, 1990; Cobbold, 2007).

Figure 5·4 shows the SNR of the AO signal as a function of lesion volume for a range of thicknesses in each of the tissues. In breast, where absorption is low, thicknesses of 20-60 mm are displayed. For all other tissues, thicknesses of 20-40 mm are shown. As discussed in Section 5.3, the illumination and detection properties used in the simulation were chosen to mimic the system characteristics of Lai (2010), and are shown in Tables 5.3 and 4.1. From the data, it can be seen that real-time AO guidance will not be feasible in liver or white matter brain tissue. In both of these tissues, the native μ_a and μ_s' coefficients are very high. As a result, the light

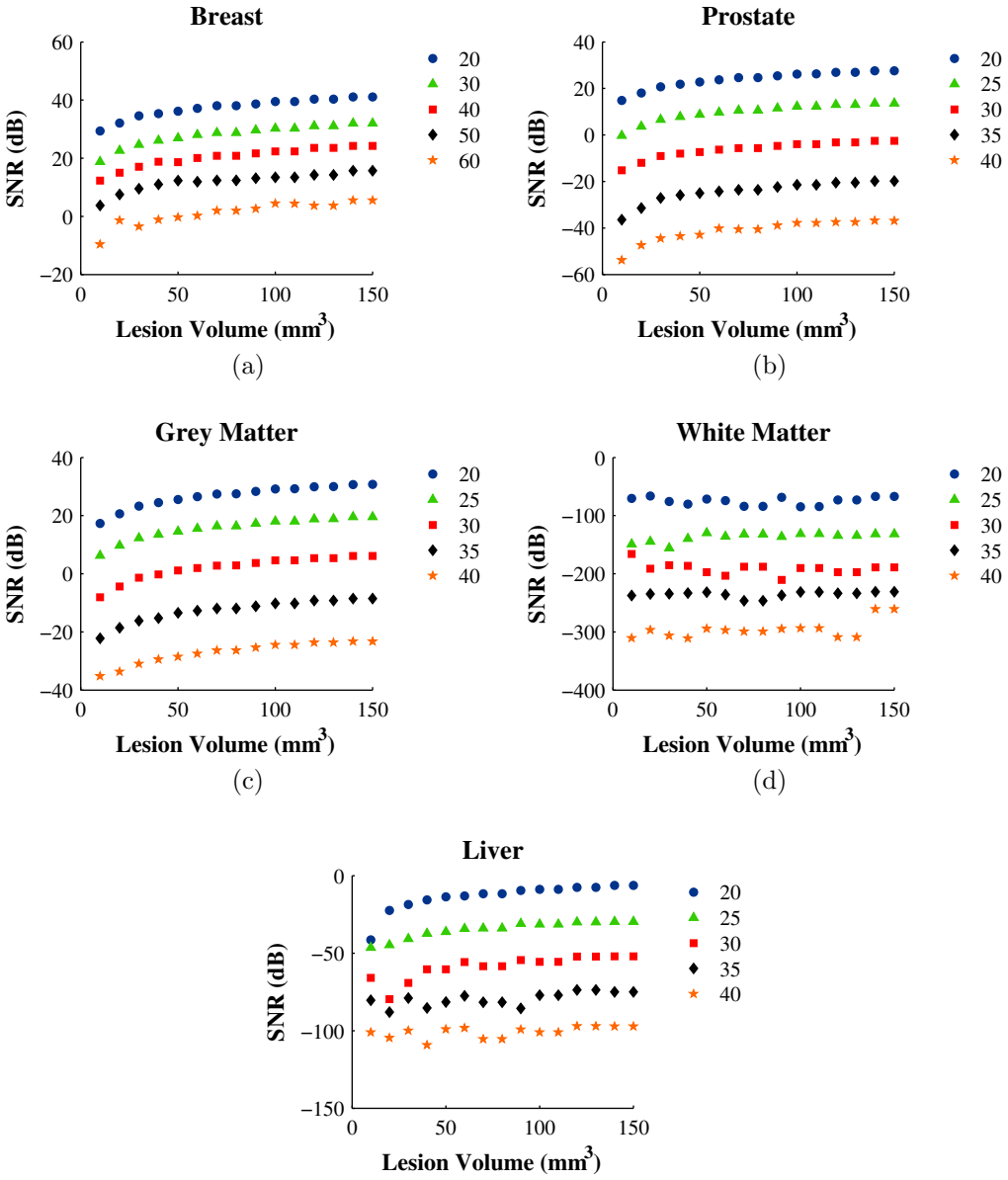

Figure 5·4: The SNR of the AO signal as a function of lesion volume in breast (a), prostate (b), grey matter (c), white matter (d), and liver (e) tissues of varying thicknesses and lesion depths. The tissue is illuminated with a 200 mW, 1064 nm source and detection is performed in transmission. All lesions are located in the centers of the tissues. Tissues thicknesses are shown in the figure legends in mm.

S_0	η_{det}	Integration Time	Filter Roll-off
200 mW	0.004	30 ms	12 dB/oct

Table 5.3: The default illumination power, light collection efficiency, and lock-in filter integration time and roll off used in the simulations presented in this chapter (Lai et al., 2011).

is heavily attenuated when it reaches the HIFU focus, and even further attenuated when it reaches the detector. Furthermore, as Table 5.1 shows, the contrast between native and lesioned tissue is low compared to other tissues. Consequently, liver and white matter are not good candidates for AO guided HIFU.

Alternatively, real-time AO guidance in breast, prostate, and grey matter appears to be feasible given the proper conditions. For breast tissues, the SNR is greater than 0 dB for all investigated lesion volumes given a thickness of 50 mm or less. Even with a thickness of 60 mm, a lesion with a volume greater than 60 mm^3 may be detected in real-time using the current system. Therefore, breast seems to be the most viable candidate organ for AO guidance. For prostate and grey matter, the SNR is greater than zero given tissue thicknesses of 25 mm or less. However, it should be possible to improve the SNR in all of the tissues by adjusting properties such as the illumination source power (S_0), the light collection efficiency of the detector (η_{det}), and the lock-in amplifier properties.

Figure 5·5 shows the SNR of a 30 mm^3 lesion in a 60 mm thick breast and a 30 mm thick prostate as a function of S_0 (a), η_{det} (b), the lock-in amplifier integration time (c), and the slope of the lock-in amplifier's low-pass filter (d). A 30 mm^3 lesion was chosen here because it is approximately the same size as the HIFU focus. As each of these properties was varied, the other properties were held constant at the values shown in Table 5.3. As Fig. 5·5(a) shows, the SNR is greater than 0 dB when the illumination power is increased to 350 mW for a 60 mm thick breast, or 600 mW for a

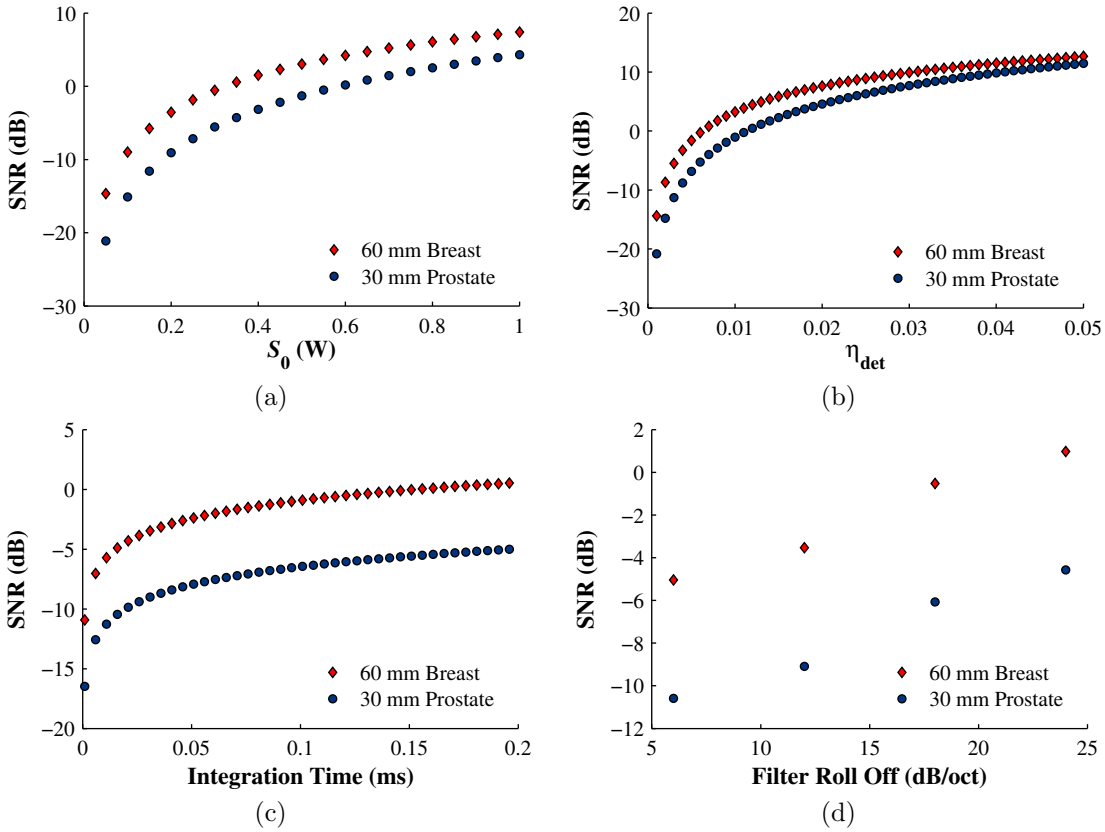

Figure 5·5: The SNR of a 30 mm^3 lesion in 60 mm thick breast and 30 mm thick prostate tissues as the illumination power (a), light collection efficiency (b), and lock-in amplifier properties (c,d) are varied. While one property is varied, the others are kept constant at the values shown in Table 5.3.

30 mm thick prostate. Given the maximum permissible exposure of 1 W/cm^2 at 1064 nm (International Commission on Non-Ionizing Radiation Protection, 1996), a 600 mW illumination power can be employed for beam sizes greater than 0.6 cm^2. Figure 5·5(b) demonstrates that SNR can also be dramatically improved by increasing the light collection efficiency of the detector. By increasing η_{det} to 0.02, which may be possible by using a large aperture fiber bundle (Lai et al., 2012), the SNR for both tissues is increased by more than 10 dB when compared to the system modeled in Fig. 5·4. Figure 5·5(c) and 5·5(d) indicate the SNR can be modestly improved by increasing the lock-in amplifier integration time and filter roll-off. However, increasing both of those result in longer settling times, and thus compromise the speed at which the lock-in signal can be acquired.

It is important to emphasize that the data presented in Figs. 5·4 and 5·5 is only applicable for transmission detection. For the case of reflection detection, the SNR is significantly worse. However, as discussed in Chapter 4, designing an AO guided HIFU system with transmission detection requires access to three sides of the target organ. Therefore, while such a system is simple to implement in breast, it would likely require the insertion of one or more catheters for targeting prostate, thus increasing the invasiveness of the surgery. On the other hand, a transmission detection system for grey matter, which is located primarily on the surface of the brain, may not be achievable.

In order to investigate the feasibility of AO-guidance in grey matter, the SNR must be evaluated in a reflection detection geometry. As Fig. 5·6 shows, where reflection detection was performed with a 20-mm radius detection aperture centered at the location of the optical source, detecting in reflection reduces the SNR by about 28 dB at 1064 nm. Given this reduction in the SNR, real-time AO sensing in grey matter does not seem attainable at 1064 nm. Nevertheless, the simulation results show that

if the illumination wavelength is changed from 1064 nm to 800 nm, most of the loss in SNR is recovered and real-time sensing may be possible in tissue thicknesses up to 25 mm, corresponding to a lesion located 12.5 mm below the surface of the tissue. However, it is critical to recognize that these predictions of SNR were based on a detection system that only operates at 1064 nm, and that the optical and acoustic simulations were performed in the absence of a skull, which would significantly distort the acoustic field and would further attenuate the light which reached the HIFU focus. Given these caveats, the SNR of a 30 mm^3 lesion centered 15 mm below the tissue surface is plotted as a function of illumination power (a), η_{det} (b), and lock-in amplifier properties (c,d) in Fig. 5·7. As the data shows, given the proper illumination power and detection efficiency, real-time AO sensing may be possible at a depth of 15 mm.

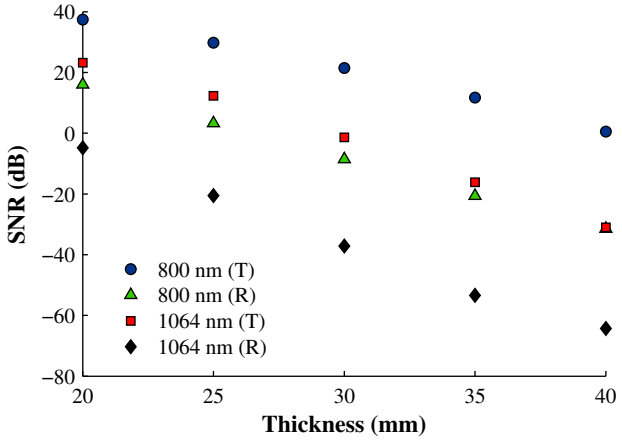

Figure 5·6: The SNR of a 30 mm^3 lesion in grey matter of multiple thicknesses given illumination at 800 nm and 1064 nm, and detection in both reflection (R) and transmission (T). All lesions are located in the centers of the tissues.

5.5 AO Guidance in a Tumor Model

Although it is critical to identify organs in which AO guidance may be feasible, all of the studies presented in Section 5.4 were conducted in media with the optical

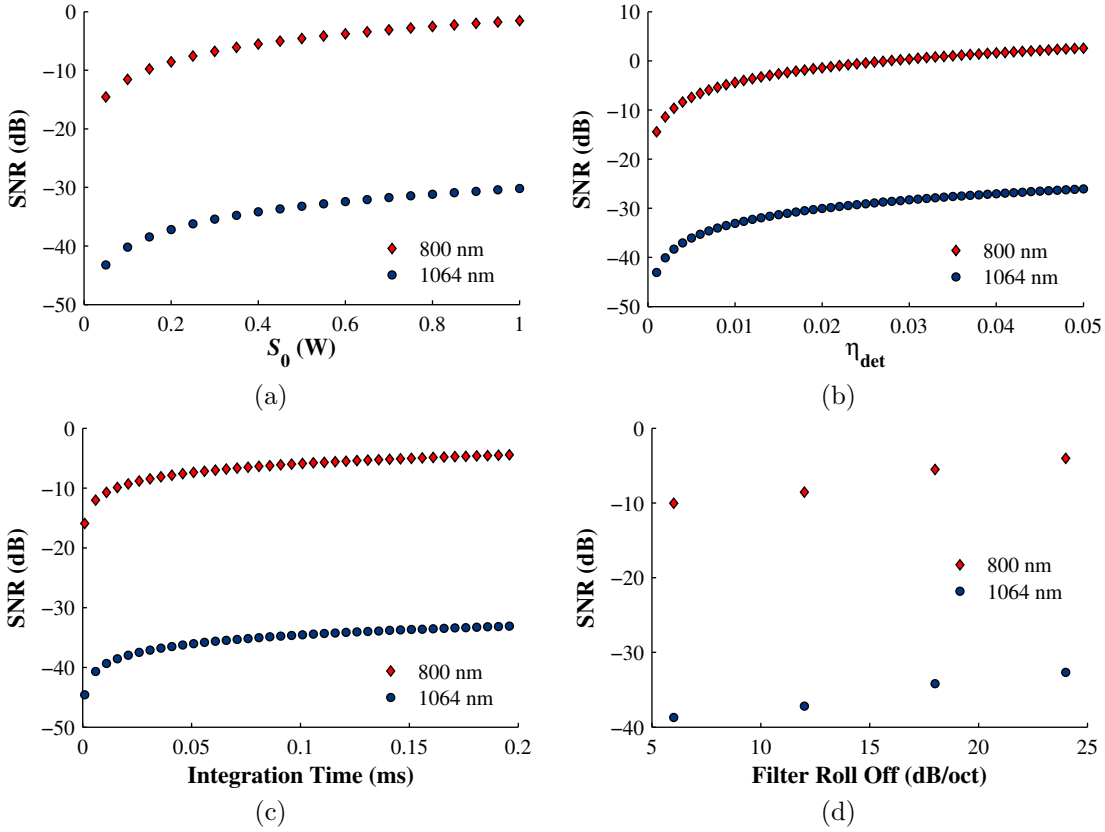

Figure 5·7: The SNR of a 30 mm^3 lesion centered 15 mm below the surface of grey matter brain tissue illuminated with a 800 nm source, and detected in a reflection geometry. SNR is plotted as a function of illumination power (a), light collection efficiency (b), and lock-in amplifier properties (c,d). While one property is varied, the others are kept constant at the values shown in Table 5.3.

properties of native and lesioned healthy tissues. However, because the focus of many HIFU therapies is the treatment of cancer, it is critical to understand if the AO system will still be viable for HIFU guidance in tumors. In this section, we seek to answer this question by comparing the SNR of lesions created in a 40 mm thick cubic breast tissue with and without the presence of a 10-mm diameter tumor. For each simulation, both the elliptical lesion and the tumor are centered within the volume, and the simulation geometry is identical to that described in Section 5.4. Breast tissue is chosen here because it is the most realistic candidate for real-time AO-guidance.

In order to predict the SNR in breast tissues containing or absent of a tumor, the optical properties listed in Table 5.4 were used. The acoustic properties of the tumor were assumed to be equal to those of breast. The native properties of bulk breast (Koelzer et al., 1995) and tumor (Jacques, 2013) tissues were taken from measurements of *ex vivo* tissues, but no data exists in literature of lesioned breast or tumor tissues. For this reason, the optical properties of the lesioned breast and tumor tissues were calculated based on the average contrast between native and lesioned liver, prostate, and brain tissues. Thus, the simulated optical contrast between native and lesioned breast and tumor tissues is the same. Unfortunately, we can not be sure as to how gross of an approximation this is. Keeping this in mind, the AO SNR is presented as a function of lesion volume in Fig. 5·8 for the elliptical lesions created

	Native		Lesioned	
Tissue	μ_a (cm^{-1})	μ_s' (cm^{-1})	μ_a (cm^{-1})	μ_s' (cm^{-1})
Bulk Breast	0.042	8.4	0.061	20.9
Tumor	0.11	9.2	0.16	22.9

Table 5.4: The optical properties at 1064 nm of native and lesioned bulk breast and tumor tissues used in simulations. The refractive index of all tissues was assumed to be 1.4, and the anisotropy coefficient was approximately 0.9 for every tissue.

inside of an otherwise homogeneous breast (red diamonds), and inside of a 10-mm diameter tumor located in the center of the breast (blue circles).

As the data shows, the presence of the tumor has an insignificant impact on the SNR of the lesions. This result is not surprising considering that the optical properties of the tumor tissue are not significantly different from those of the breast tissue, and the same contrast was assumed between native and lesioned tissues. However, the insignificant difference between the optical properties of bulk breast and tumor tissues means that it would be difficult to optically detect a breast tumor, at least at 1064 nm. Nevertheless, these results suggest that AO guided HIFU should be equally as viable in tumors as it is in normal breast tissue. The illumination and detection properties used in the simulation were the same as in Section 5.4, and are given in Table 5.3.

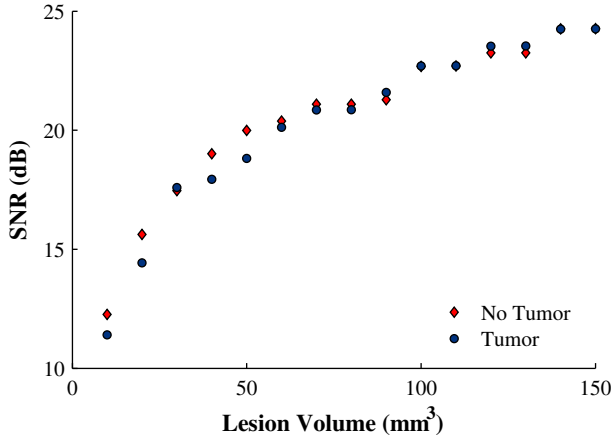

Figure 5·8: The SNR of the AO signal as a function of lesion volume for lesions created in the center of breast tissue in the presence (blue circles) and absence (red diamonds) of a 10 mm diameter tumor.

5.6 Summary and Conclusions

In this chapter, several different clinical scenarios were explored with the goal of evaluating the clinical viability of an AO guided HIFU system. First, it was shown

that although AO-guidance is suitable for guiding the ablation of large volumes, an appropriate strategy must be employed. By starting away from the optical source and moving towards it, an array of homogenous lesions can be created to treat a large volume. However, if the treatement was to start close to the optical source and move away from it, the resulting lesion volumes would be completely inhomogeneous and the array would be grossly asymmetric. This demonstrates that there is an optimum strategy to be employed while using AO guidance, and in order for the technique to be more predictable, the optical properties of the targeted tissue may need to be imaged prior to treatment. This is in addition to the strategy for moving the HIFU source to minimize interactions from prior lesions.

Subsequently, the expected SNR of the AO signal in breast, prostate, brain, and liver tissues was evaluated in an effort to determine which organs could be appropriate for AO guidance. Overall, it was found that due to the low absorption and the optical accessibility of the breast, it is the ideal target organ for AO guided HIFU. By varying illumination and detection properties such as the source power, the light collection efficiency, and the lock-in amplifier properties, it was shown that real-time AO guidance may be feasible in breast at depths up to 30 mm and in prostate at depths up to 15 mm. Furthermore, it was shown that by employing an 800 nm source and a reflection-based detector, real-time guidance may be possible at lesion depths up to 15 mm in the brain grey matter. In the final section, it was shown that the presence of a breast tumor is expected to have a negligible impact on AO guidance, although there is a need for more measurements as there is scant optical data on tumor properties. However, the simulations suggest that the data presented in Section 5.4 may be equally applicable to the treatment of cancerous tissues.

Although a number of predictions about the clinical viability of AO guidance have been made in this chapter, it must be understood that several assumptions have been

made in coming to these conclusions. The largest assumption made was that all of these simulations were performed using optical properties that were not measured *in vivo*. Moreover, the optical properties of lesioned breast and tumor tissues were based off of the average contrast measured in other organs. Therefore, although it was found that breast is the ideal candidate organ for AO guided HIFU, the optical properties of native and lesioned breast tissues must be confirmed *in vivo* before the technique can truly be considered clinically viable.

Chapter 6

Summary and Conclusions

6.1 Summary of Results

The overall goals of the studies reported in this thesis were to better understand the optical contrast between native and lesioned tissues, and to assess and improve upon current AO guided HIFU techniques using a modeling based approach. In accordance with these objectives, four specific aims were established and presented in Section 1.3. The key results associated with each of these specific aims are summarized in this section.

6.1.1 Thermally Induced Optical Property Changes

In Chapter 2, the basic theory of light propagation and light-tissue interactions was introduced. Using first-order kinematic processes for describing irreversible thermal damage, a model was developed to express thermally induced optical property changes as a function of thermal dose – a widely-used metric for predicting thermal damage induced by HIFU. A system for measuring the optical properties of tissues was constructed using a spectrophotometer fitted with a modified integrating sphere accessory, and experiments were performed to measure thermally induced optical property changes in *ex vivo* chicken breast between 500-1100 nm. Results showed that while the nominal parameters used in the thermal dose model were insufficient for describing optical property changes, the parameters could be altered to develop reasonable predictions. Additionally, the data suggested that the optical scattering coefficient

was significantly more sensitive to thermal effects than the absorption coefficient. It was also determined that a temperature threshold exists for scattering changes, but no such threshold was observed for thermally induced absorption changes.

6.1.2 AO-Guided HIFU Model Development

In Chapter 3, a comprehensive model was developed to describe the AO guidance of HIFU. The model consisted of five separate sub-models integrated into a single MATLAB script. The theory relevant to each sub-model was presented, and numerical solutions were validated by comparisons to analytical solutions. The angular spectrum method was used to model the linear acoustic field from the HIFU source, while the resulting temperature field, due to the absorption of ultrasound, was modeled using a finite-difference time-domain solution to the Pennes bioheat transfer equation. Changes in tissue optical properties were calculated using the thermal dose dependent model presented in Chapter 2. The diffuse optical field was modeled using an open-source, GPU-accelerated Monte Carlo algorithm, which was modified to calculate light-sound interactions in a linear regime, and AO signals were calculated using a photorefractive crystal detection model. The restrictions and requirements of the model were presented in Section 3.7.2, and all of the code can be found on the Boston University Digital Common Library (Adams, 2014).

6.1.3 Design of an AO-Guided HIFU System

In Chapter 4, the comprehensive model was used to develop an optimal design for an AO guided HIFU system, and to assess the robustness of its AO signal to changes in tissue thickness, lesion contrast, and lesion location. Comparisons were made between the model and experimental data, and excellent agreement was observed when the size of the lesion was less than or equal to the HIFU focal volume. With larger lesions, a divergence between the model and the previously obtained experimental

data was observed, and it was hypothesized that this discrepancy was caused by the high pressures used in experiments. Furthermore, it was demonstrated that the AO signal contrast is much more sensitive to lesion formation than the total optical signal contrast, and a discussion was presented which argued that AO sensing is better to use for HIFU guidance than purely optical sensing due to its higher signal contrast and spatial resolution.

With regard to system design, it was found that an optimally designed AO guided HIFU system should have an optical source that illuminates the target organ at 90° relative to the HIFU propagation, employ an optical wavelength which exhibits minimal absorption in tissue, and set up signal detection in transmission mode using a detection aperture that collects as much light as possible. By perturbing the tissue thickness and the lesion position, it was shown that both of these factors affect how the AO signal changes as a lesion is formed, and that ΔAO scales with the optical fluence within the HIFU focus. Therefore, predictions of lesion volume based on AO signal change should be adjusted according to those factors. Additionally, it was found that variations in the optical properties of a lesion cause significant uncertainties in the prediction of lesion volume, and that these uncertainties are greater for larger lesions.

6.1.4 Assessing the Clinical Viability of AO-Guided HIFU

In Chapter 5, the comprehensive model was used to assess the clinical viability of AO guided HIFU by examining its ability to guide the ablation of large volumes, and by predicting the SNR of AO signals in multiple tissue types. It was determined that AO sensing is a clinically viable technique for guiding the ablation of large volumes, but that results are heavily dependent upon the treatment strategy employed. Furthermore, it was determined that real-time sensing may be feasible using the current AO system in breast tissue up to 60 mm thick and prostate tissue up to 30 mm thick. Additionally, it was shown that illumination and detection properties such as source

power, light collection efficiency, and lock-in amplifier settings can be adjusted to achieve higher SNR and greater sensing depths. It was shown that if a system can be designed with an 800 nm source and a reflection-based detector, real-time guidance may be possible at lesion depths up to 15 mm in the brain's grey matter.

In order to demonstrate that the system should also be viable for ablating cancerous tissues, a study was performed to compare the SNR of a lesion created in the absence and presence of a tumor inside of a breast. Results showed that the tumor had a negligible impact of the calculated AO SNR. However, this study was performed using assumed optical properties, and must be confirmed using measured optical properties. Overall, the results suggest that real-time AO guidance of HIFU is clinically viable, and it is best suited for guiding HIFU treatments in breasts.

6.2 Suggestions for Future Work

Although this dissertation has demonstrated significant progress towards understanding the important mechanisms and parameters associated with AO guided HIFU, much work remains to be done in order to make the technique suitable for clinical trials. In this section, suggestions for future work are divided into three categories.

6.2.1 Model Improvement

The AO guided HIFU model developed in Chapter 3 was sufficient for the purposes of this work, but it has many limitations in its current form. In order to improve the model's flexibility, performance, and accuracy, the following improvements are recommended. First and foremost is the incorporation of a nonlinear acoustic model for HIFU propagation, and the development of the AO model to allow for the high pressures and nonlinearities of the acoustic field. This would allow for more accurate predictions of tissue heating, optical property changes, ultrasound induced phase modulations, and AO signals for acoustic parameters that are commonly used for

HIFU therapy. Next, it is recommended that the model be adjusted to allow for the inclusion of inhomogeneous acoustic and thermal properties. This would allow for tissue inhomogeneities such as blood vessels to be present in simulations, and for lesions to possess different properties than the unlesioned medium. Additionally, it is recommended that the temperature field solution be adjusted to allow for arbitrarily complex geometries. This would allow for temperature calculations to be performed in realistic organ models instead of approximating them as cubic media. Finally, it is recommended that the performance of the acoustic and temperature codes be improved by implementing them in more efficient computational languages, such as CUDA.

6.2.2 Apparatus Improvement

As the results presented in Chapter 5 demonstrated, the SNR of the AO signal can be enhanced by increasing the system's illumination power and light collection efficiency. Furthermore, increasing the illumination power of the system has the additional benefit of improving the response time of the PRC, which is required in order for the detection system to be compatible with the short speckle decorrelation times observed *in vivo*. However, increasing the illumination power of a CW source requires that the beam size be increased appropriately, in order to stay below the maximum permissible exposure intensities *in vivo*. Alternatively, by employing a long-pulse laser with high peak powers but low duty cycles, the SNR of the system can be improved without increasing the beam size or the time averaged intensities (Rousseau et al., 2008).

In addition to increasing the source power by incorporating a long-pulse laser, it is also recommended that the light collection efficiency of the system be improved. Currently, the system uses large free-space lenses to perform diffuse light collection and image the surface of the tissue to the face of the PRC. However, by placing a large aperture fiber bundle at the surface of the tissue, significantly more diffuse

light can be collected (Lai et al., 2012) and SNR can be drastically improved. The implementation of fibers would be advantageous from a portability perspective as well. Overall, it is recommended that both a pulsed laser and a large aperture fiber bundle be implemented in the current apparatus.

6.2.3 Experiments

As previously discussed, all of the results presented in Chapter 5 were based on assumed optical properties. In the best case scenarios, the properties were derived from measurements of *ex vivo* human tissues, but many were calculated from contrast observed in other tissues. Specifically, the optical properties of lesioned breast and tumor tissue, which we have concluded are the ideal target organs for AO guidance, were calculated from the average contrast exhibited by lesioned brain, liver, and prostate tissues. While we consider this a sufficient approximation for the purposes of this work, the optical properties of both healthy and cancerous breast tissues must be quantified prior to performing animal or clinical trials. In order to characterize thermally induced optical property changes in breast, the *ex vivo* experiments presented in Chapter 2 should be repeated with human breast tissues. Additionally, it is recommended that optical property measurements be performed on HIFU lesions, and these measurements be compared to lesions created in thermal baths. Although we believe that we have accurately characterized thermally induced optical changes, it is possible that the mechanical effects of HIFU could induce further contrast.

Furthermore, it is recommended that a method be developed for characterizing the optical properties of native and lesioned tissues *in vivo*. In reality, there is likely to be additional optical changes in lesioned tissue that is caused by factors such as hydration, blood content, and blood coagulation. However, these factors are impossible to replicate *ex vivo*. Moreover, the ability to measure optical properties *in situ* would allow for the target region to be imaged prior to a HIFU treatment, and al-

gorithms could be created to adjust predictions of lesion volume based on the lesion location and the surrounding medium. One such method that could possibly be used for imaging optical properties prior to HIFU is pressure contrast imaging (Lai et al., 2009).

Appendices

Appendix A

Using the Inverse Adding–Doubling Program

In this thesis, the optical properties of tissues are determined by making measurements of total reflectance and transmittance using an integrating sphere, and then passing these measurements to an inverse adding-doubling (IAD) program, obtained from Prahl (2013). The IAD guesses the optical properties of the sample, then iteratively performs a numerical solution to the RTE using the adding–doubling method (Prahl, 1995) until the solution converges to measured values of reflection and transmission. The adding–doubling method is a general numerical solution to the RTE, which quickly solves numerical integrals in order to obtain a solution to the RTE given a tissue with a known set of optical properties in a slab geometry.

Below is a sample input file (InputFile.rxt) that is used to pass integrating sphere measurements to the IAD. In this case, total reflectance (M_R) and transmittance (M_T) are passed to the IAD, while the collimated transmission fields (M_U) are left blank. The # symbol indicates that the rest of the line is a comment. The input file is passed to the IAD from the command line with the following syntax:

```
prompt> ./iad -g 0.97 -e 0.002 -X InputFile
```

where the "-g" option sets the anisotropy coefficient, the "-e" option sets the error tolerance, and the "-X" enables the dual-beam spectrophotometer option. If collimated transmission measurements are available, the anisotropy coefficient does not need to be specified.

```
IAD1   # Mandatory identification tag

1.4    # Index of refraction of the sample
1.52   # Index of refraction of the top and bottom slides
1.95   # [mm] Thickness of sample
1.01   # [mm] Thickness of slides
2      # [mm] Diameter of illumination beam
0.99   # Reflectivity of the reflectance calibration standard

1      # Number of spheres during each measurement

       # Properties of sphere used for reflection measurements
110    # [mm] Sphere Diameter
16     # [mm] Sample Port Diameter
20.3   # [mm] Entrance Port Diameter
26.9   # [mm] Detector Port Diameter
0.99   # Reflectivity of the sphere wall

       # Properties of sphere used for transmission measurements
110    # [mm] Sphere Diameter
16     # [mm] Sample Port Diameter
0      # [mm] Entrance Port Diameter
26.9   # [mm] Detector Port Diameter
0.99   # Reflectivity of the sphere wall

2      # Measurements, i.e., M_R, M_T, M_U

#lambda   M_R   M_T   M_U
500   0.546718674   0.069128938
501   0.550080528   0.070991306
502   0.552532845   0.073047185
503   0.553249588   0.075036602
504   0.556943436   0.076993542
505   0.558506432   0.079091129
...
1100   0.43905613   0.385099678
```

Appendix B

AO Guided HIFU Example

Below is an example MATLAB script that is used to simulate the AO guidance of HIFU. The script calls several sub-functions, all of which can be found on the BU Digital Common Library (Adams, 2014). In order to run, each instance of the AO MCX binary calls on an input file. An example input file, "MainLesions.inp", is given following the MATLAB script.

B.1 AO_ExampleCode.m

```
%% AO_ExampleCode.m
% An example of how to use the AO guided HIFU code. This example
% exposes a chicken breast tissue to a target peak pressure of 6
% MPa for 120 s and calculates the AO signal every 5 s from a
% detector in transmission.
%
% Written by Matt Adams, 7/20/14

%% Setup
% Set paths for subfunctions
addpath /mnt/nokrb/adamsm2/MATLAB/mtimesx_20110223
addpath /mnt/nokrb/adamsm2/MATLAB
addpath /mnt/nokrb/adamsm2/aoi-mcx/mcx/utils
binpath = '/mnt/nokrb/adamsm2/aoi-mcx/mcx/bin/mcx_det';

%HIFU Exposure Parameters
PeakP_Water = 6e6;   % Target Peak Pressure in Water
feedback_time = 5;   %AO feedback step time (s)
DutyCycle = 1; % The duty cycle of the HIFU (100%)
size_tissue = [40 40 40]*1e-3;  %Tissue size in mm

```

```
% Grid, Domain, Heating time
grid =0.1e-3;   % grid spacing (mm)
time_step = 100e-3; % Time step for BHTE simulations (s)
cooling_time = 0;  % (s)
AO_times = [0:feedback_time:120]; %2 min of heating

% Acoustic Properties
f0 = 1.1e6;     %Acoustic Frequency
tissue.cs = 1585;    %Speed of sound in tissue (m/s)
tissue.alpha = 5*(f0/1e6).^1.1;   %Attenuation Coefficient (Np/m)
tissue.alphaAbs = tissue.alpha * 0.7816;   %Absorption coefficient ...
    (Np/m)
tissue.rho = 1040;      % Density of tissue

% Thermal Properties
tissue.Cv = 3210; %Specific Heat of Tissue (J/kgC)
tissue.K = 0.4683; %Thermal Conductivity (W/mC)
T_ambient = 21; %Ambient Temperature (C)
tissue.Wb = 0;  %No perfusion or metabolic heat generation
tissue.Cb = 0;
tissue.Tb = T_ambient;
tissue.Qm = 0;

% Thermal dose isodose constants
tissue.R1 = 0.25;  % See Adams et al 2014 (in PMB)
tissue.R2 = 0.63;

% Optical Properties
tissue.mu_a0 = 0.01;   %(1/cm)
tissue.deltaA = 6.5;  % maximum relative absorption change
tissue.mu_sp0 = 1.1;   %(1/cm)
tissue.deltaS_low = 6.85; % max mu_sp change below threshold
tissue.deltaS_high = 10.6; % max mu_sp change above threshold
tissue.g = 0.9;   % anisotropy coefficient
tissue.n = 1.4;    % refractive index
tissue.D0_43 = 2214; %Thermal dose constant in CEM_43
tissue.TempThreshold = 70;     % scattering threshold temp (C)
tissue.MaxScat = 12.759;    % Maximum scattering coefficient

% Target lesion location
target.shiftx = 0; %center
target.shifty = 0; %center
```

```
63 target.depth = size_tissue(3)/2+2e-3; % approx in center
64
65 % Initialize some vectors
66 PRC_DC = zeros(1,length(AO_times));    %AO signal
67 Volumes = zeros(1,length(AO_times));    %Lesion Volumes
68 Thermal_Dose = 0;
69 Tfinal = T_ambient;
70 Tmax = T_ambient;
71
72 %% Calculate Pressure
73 [~,~,p_tissue,~,~] = ...
      Calc_H102_Pressure(grid,f0,tissue,size_tissue,target);
74 Cal_factor = 45.347994; % Max pressure in water for a 1 Pa source
75 p_tissue = p_tissue/Cal_factor*PeakP_Water; %Adjust pressure
76
77 %% Calculate Intensity
78 [Intensity,P_Mag,P_Angle,i_hat,j_hat,k_hat] = ...
79     Calc_Intensity(p_tissue, f0, tissue, grid ,'AO');
80 mydim=size(Intensity);
81 PRESSURE = zeros(mydim(1),mydim(2),mydim(3),4);
82 PRESSURE(:,:,:,1)=P_Mag.*i_hat;
83 PRESSURE(:,:,:,2)=P_Mag.*j_hat;
84 PRESSURE(:,:,:,3)=P_Mag.*k_hat;
85 PRESSURE(:,:,:,4)=P_Angle;
86
87 % Reduce Pressure to 100 kPa and write file for AO simulation
88 PRESSURE(:,:,:,1:3) = PRESSURE(:,:,:,1:3)/max(max(max(P_Mag)))*1e5;
89 PRESSURE=single(PRESSURE);
90 fid = fopen('Acoustics.bin','wb');
91 aa = fwrite(fid,PRESSURE,'float');
92 fclose(fid);
93 clear PRESSURE i_hat j_hat k_hat P_Mag P_Angle
94 display(['Acoustics Calculated at ' datestr(now) ' EST'])
95
96 %% Calculate Homogeneous
97 % Calculate volume and write file
98 vol=ones(mydim(1),mydim(2),mydim(3));
99 fid=fopen('Homogeneous.bin','wb');
100 aa=fwrite(fid,vol,'uchar');
101 fclose(fid);
102
103 % Run AO mcx file (0.1 mm grid spacing and detect a max of 6e7 photons)
```

```
104 [status,result] = system([binpath ' -u 0.1 -H 60000000 -f Homo.inp']);
105 % Postprocess and calculate PRC signal
106 [~,~,~,~,PRC,~,~,~,~] = ...
107     AOI_MCX_Eval('Homo.inp',5e-9,size(vol),tissue.mu_a0/10);
108 PRC_DC(1) = PRC(2,1);   %Only use the DC signal
109 display(['Homogeneous Medium Calculated at ' datestr(now) ' EST'])
110
111 %% Calculate heating and AO for each feedback time step
112 for idx = 2:length(AO_times)
113     %  NOTE: The first two steps need to be calculated separately
114     %  because the optical properties haven't reached their maximum
115     %  values yet
116
117     % Calculate Temperature and Thermal_Dose
118     [Tfinal, Tmax, Thermal_Dose, ~] = Calc_BHTE(Intensity*DutyCycle, ...
119     Tfinal, Thermal_Dose, feedback_time, cooling_time,time_step, ...
120     tissue, grid, Tmax);
121
122     % Calculate Optical Properties
123     [mu_spfinal,mu_afinal]= ...
            Calc_Optical_Changes(tissue,Thermal_Dose,Tmax);
124     % Calculate Lesion Volume
125     Volumes(idx)=length(find(mu_spfinal > tissue.MaxScat))*(grid*1e3)^3;
126
127     % Create Volume with 5 tissue types
128     max_scat = CreateAoMcxVolume(mu_spfinal,5,'OpticalVolume.bin');
129
130     % Run Simulation
131     if idx == 2
132         [status,result] = ...
133             system([binpath ' -u 0.1 -H 60000000 -f Step1.inp']);
134         % Postprocess and calculate PRC signal
135         [~,~,~,~,PRC,~,~,~,~] = ...
136             AOI_MCX_Eval('Step1.inp',5e-9,size(vol),...
137             linspace(tissue.mu_a0/10,max(max(max(mu_afinal)))/10,5));
138     elseif idx == 3
139         [status,result] = ...
140             system([binpath ' -u 0.1 -H 60000000 -f Step2.inp']);
141         % Postprocess and calculate PRC signal
142         [~,~,~,~,PRC,~,~,~,~] = ...
143             AOI_MCX_Eval('Step2.inp',5e-9,size(vol),...
144             linspace(tissue.mu_a0/10,max(max(max(mu_afinal)))/10,5));
```

```
    else
        [status,result] = ...
            system([binpath ' -u 0.1 -H 60000000 -f MainLesions.inp']);
        % Postprocess and calculate PRC signal
        [~,~,~,~,PRC,~,~,~,~]= ...
            AOI_MCX_Eval('MainLesions.inp',5e-9,size(vol),...
            linspace(tissue.mu_a0/10,max(max(max(mu_afinal)))/10,5));
    end

    PRC_DC(idx) = PRC(2,1);
    display(['Heating Time ' num2str(idx) ' of ' ...
        num2str(length(AO_times)) ' Calculated at ' datestr(now) ' ...
           EST'])
end
```

B.2 MainLesions.inp

```
100000000     # total photon, use -n to overwrite in the command line
1655742     # RNG seed, negative to generate
1 201.5 201.5     # source position (in grid units)
1 0 0     # initial directional vector (x,y,z)
0.e+00 5.e-09 5.e-09     # time-gates(s): start, end, step
OpticalVolume.bin     # volume of media types (‘uchar’ format)
Acoustics.bin     # Acoustics volume (4D‘float’ format)
1 401 1 401     # x: leave as 1, voxels per side, start/end indices
1 401 1 401     # y: leave as 1, voxels per side, start/end indices
1 401 1 401     # z: leave as 1, voxels per side, start/end indices
1040 1585 1.1     # rho (kg/m^3), cs (m/s), f0 (MHz)
1064 0.32      # lambda0 (nm), nu
5     # total number of media (not including air)
1.100 0.9 0.001000 1.4     #mu_s (1/mm), g, mu_a(1/mm), n
4.015 0.9 0.002625 1.4
6.930 0.9 0.004250 1.4
9.845 0.9 0.005875 1.4
12.76 0.9 0.007500 1.4
1 200     # number of detectors and radii (in grid units)
401 201 201     # detector 1 position (in grid units)
```

References

Abramowitz, M. and Stegun, I. A. (1972). *Handbook of mathematical functions: with formulas, graphs, and mathematical tables*. Number 55. Courier Dover Publications.

Adams, M. T. (2014). A modeling-based assessment of acousto-optic sensing for monitioring high-intensity focused ultrasound lesion formation. *Boston University Digital Common, ENG: Mechanical Engineering Theses and Dissertations, http://open.bu.edu/handle/2144/1362*.

Adams, M. T., Wang, Q., Cleveland, R. O., and Roy, R. A. (2014). Thermal dose dependent optical property changes of *ex vivo* chicken breast tissues between 500 and 1100 nm. *Physics in Medicine & Biology*, 59(13):3249–3260.

Agah, R., Gandjbakhche, A., Motamedi, M., Nossal, R., and Bonner, R. (1996). Dynamics of temperature dependent optical properties of tissue: dependence on thermally induced alteration. *IEEE Transactions on Biomedical Engineering*, 43(8):839–846.

Al-Bataineh, O., Jenne, J., and Huber, P. (2012). Clinical and future applications of high intensity focused ultrasound in cancer. *Cancer Treatment Reviews*, 38(5):346–353.

Alhamami, M., Kolios, M. C., and Tavakkoli, J. (2014). Photoacoustic detection and optical spectroscopy of high-intensity focused ultrasound-induced thermal lesions in biologic tissue. *Medical Physics*, 41(5):053502.

Ames, W. (1992). *Numerical methods for partial differential equations*, chapter 5. Academic Press, San Diego.

ANSI (2005). Ansi z136.3. *American National Standard for the Safe Use of Lasers in Healthcare Facilities*.

ANSI (2007). Ansi z136.1. *American National Standard for the Safe Use of Lasers*.

Arridge, S. R. (1999). Optical tomography in medical imaging. *Inverse Problems*, 15(2):R41.

Bailey, M. R., Couret, L. N., Sapozhnikov, O. A., Khokhlova, V. A., ter Haar, G., Vaezy, S., Shi, X., Martin, R., and Crum, L. A. (2001). Use of overpressure to assess the role of bubbles in focused ultrasound lesion shape *in vitro*. *Ultrasound in Medicine & Biology*, 27(5):695–708.

Ben-David, M., Cantor, R., Balbul, N., Yehuda, M., and Gannot, I. (2008). Measuring tissue heat penetration by scattered light measurements. *Lasers in Surgery and Medicine*, 40(7):494–499.

Benoit a la Guillaume, E., Bortolozzo, U., Huignard, J.-P., Residori, S., and Ramaz, F. (2013). Dynamic ultrasound modulated optical tomography by self-referenced photorefractive holography. *Optics Letters*, 38(3):287–289.

Benoit a la Guillaume, E., Farahi, S., Bossy, E., Gross, M., and Ramaz, F. (2012). Acousto-optical coherence tomography with a digital holographic detection scheme. *Optics Letters*, 37(15):3216–3218.

Black, J. F. and Barton, J. K. (2004). Chemical and structural changes in blood undergoing laser photocoagulation. *Photochemistry and Photobiology*, 80(1):89–97.

Blackstock, D. T. (2000). *Fundamentals of physical acoustics*. John Wiley & Sons.

Blonigen, F. J., Nieva, A., DiMarzio, C. A., Manneville, S., Sui, L., Maguluri, G., Murray, T. W., and Roy, R. A. (2005). Computations of the acoustically induced phase shifts of optical paths in acoustophotonic imaging with photorefractive-based detection. *Applied Optics*, 44(18):3735–3746.

Boas, D., Culver, J., Stott, J., and Dunn, A. (2002). Three dimensional Monte Carlo code for photon migration through complex heterogeneous media including the adult human head. *Optics Express*, 10(3):159–170.

Boas, D. A., Brooks, D. H., Miller, E. L., DiMarzio, C. A., Kilmer, M., Gaudette, R. J., and Zhang, Q. (2001). Imaging the body with diffuse optical tomography. *IEEE Signal Processing Magazine*, 18(6):57–75.

Bohren, C. F. and Huffman, D. R. (2008). *Absorption and scattering of light by small particles*. John Wiley & Sons.

Çilesiz, I. F. and Welch, A. J. (1993). Light dosimetry: effects of dehydration and thermal damage on the optical properties of the human aorta. *Applied Optics*, 32(4):477–487.

Chaves, J. (2008). *Introduction to nonimaging optics*. CRC Press.

Cheong, W.-F., Prahl, S. A., Welch, A. J., et al. (1990). A review of the optical properties of biological tissues. *IEEE Journal of Quantum Electronics*, 26(12):2166–2185.

Chitnis, P. V., Brecht, H.-P., Su, R., and Oraevsky, A. A. (2010). Feasibility of optoacoustic visualization of high-intensity focused ultrasound-induced thermal lesions in live tissue. *Journal of Biomedical Optics*, 15(2):021313.

Chung, A. H., Jolesz, F. A., and Hynynen, K. (1999). Thermal dosimetry of a focused ultrasound beam in vivo by magnetic resonance imaging. *Medical Physics*, 26(9):2017–2026.

Church, C. C. (2007). Thermal dose and the probability of adverse effects from hifu. In *6th International Symposium on Therapeutic Ultrasound*, volume 911, pages 131–137. AIP Publishing.

Cobbold, R. S. (2007). *Foundations of biomedical ultrasound*. Oxford University Press, USA.

Contini, D., Martelli, F., and Zaccanti, G. (1997). Photon migration through a turbid slab described by a model based on diffusion approximation. I. Theory. *Applied Optics*, 36(19):4587–4599.

Coussios, C. C., Farny, C. H., Ter Haar, G., and Roy, R. A. (2007). Role of acoustic cavitation in the delivery and monitoring of cancer treatment by high-intensity focused ultrasound (HIFU). *International Journal of Hyperthermia*, 23(2):105–120.

Coussios, C. C. and Roy, R. A. (2008). Applications of acoustics and cavitation to noninvasive therapy and drug delivery. *Annual Review of Fluid Mechanics*, 40:395–420.

Delaye, P., Blouin, A., Drolet, D., De Montmorillon, L.-A., Roosen, G., and Monchalin, J.-P. (1997). Detection of ultrasonic motion of a scattering surface by photorefractive InP:Fe under an applied dc field. *Journal of the Optical Society of America B*, 14(7):1723–1734.

Delaye, P., De Montmorillon, L.-A., and Roosen, G. (1995). Transmission of time modulated optical signals through an absorbing photorefractive crystal. *Optics Communications*, 118(1):154–164.

Dolfi, D. and Micheron, F. (1992). Imaging process and system for transillumination with photon frequency marking. US Patent 5,174,298.

Draudt, A. B. (2012). *Evaluation of harmonic motion elastography and acousto-optic imaging for monitoring lesion formation by high intensity focused ultrasound*. PhD thesis, Boston University.

Drezek, R., Dunn, A., and Richards-Kortum, R. (1999). Light scattering from cells: finite-difference time-domain simulations and goniometric measurements. *Applied Optics*, 38(16):3651–3661.

Duck, F. A. (1990). *Physical properties of tissues: a comprehensive reference book*. Academic Press.

Edson, P. L. (2001). *The role of acoustic cavitation in enhanced ultrasound-induced heating in a tissue-mimicking phantom*. PhD thesis, Boston University.

Elson, D. S., Li, R., Dunsby, C., Eckersley, R., and Tang, M.-X. (2011). Ultrasound-mediated optical tomography: a review of current methods. *Interface Focus*, 1(4):632–648.

Essenpreis, M. (1992). Thermally induced changes in optical properties of biological tissues. *University College London, England*.

Fang, Q. (2009). Monte Carlo eXtreme (MCX). *http://mcx.sourceforge.net/cgi-bin/index.cgi?Home*.

Fang, Q. and Boas, D. A. (2009). Monte Carlo simulation of photon migration in 3D turbid media accelerated by graphics processing units. *Optics Express*, 17(22):20178–20190.

Farahi, S., Montemezzani, G., Grabar, A. A., Huignard, J.-P., and Ramaz, F. (2010). Photorefractive acousto-optic imaging in thick scattering media at 790 nm with a $Sn_2P_2S_6$:Te crystal. *Optics Letters*, 35(11):1798–1800.

Farrell, T. J., Patterson, M. S., and Wilson, B. (1992). A diffusion theory model of spatially resolved, steady-state diffuse reflectance for the noninvasive determination of tissue optical properties *in vivo*. *Medical Physics*, 19(4):879–888.

Forget, B.-C., Ramaz, F., Atlan, M., Selb, J., and Boccara, A.-C. (2003). High-contrast fast Fourier transform acousto-optical tomography of phantom tissues with a frequency-chirp modulation of the ultrasound. *Applied Optics*, 42(7):1379–1383.

Fry, F., Heimburger, R., Gibbons, L., and Eggleton, R. (1970). Ultrasound for visualization and modification of brain tissue. *IEEE Transactions on Sonics and Ultrasonics*, 17(3):165–169.

Germer, C.-T., Roggan, A., Ritz, J. P., Isbert, C., Albrecht, D., Mueller, G., and Buhr, H. J. (1998). Optical properties of native and coagulated human liver tissue and liver metastases in the near infrared range. *Lasers in Surgery and Medicine*, 23(4):194–203.

Gleyzes, P., Guernet, F., and Boccara, A. (1995). Picometric profilometry. II. Multidetector approach and multiplexed lock-in detection. *Journal of Optics*, 26(6):251–265.

Goldberg, S. N., Grassi, C. J., Cardella, J. F., Charboneau, J. W., Dodd III, G. D., Dupuy, D. E., Gervais, D. A., Gillams, A. R., Kane, R. A., Lee Jr, F. T., et al. (2009). Image-guided tumor ablation: standardization of terminology and reporting criteria. *Journal of Vascular and Interventional Radiology*, 20(7):S377–S390.

Goodman, J. W. (1985). *Statistical optics*. John Wiley & Sons.

Goodman, J. W. (2005). *Introduction to Fourier optics*. Roberts and Company Publishers.

Goodman, J. W. (2007). *Speckle phenomena in optics: theory and applications*. Roberts and Company Publishers.

Graaff, R., de Mul, F. F., Jentink, H. W., and Aarnoudse, J. G. (1993). Similarity relations for anisotropic scattering in absorbing media. *Optical Engineering*, 32(2):244–252.

Gross, M., Goy, P., and Al-Koussa, M. (2003). Shot-noise detection of ultrasound-tagged photons in ultrasound-modulated optical imaging. *Optics Letters*, 28(24): 2482–2484.

Gross, M., Goy, P., Forget, B., Atlan, M., Ramaz, F., Boccara, A., and Dunn, A. (2005). Heterodyne detection of multiply scattered monochromatic light with a multipixel detector. *Optics Letters*, 30(11):1357–1359.

Gross, M., Lesaffre, M., Ramaz, F., Delaye, P., Roosen, G., and Boccara, A. (2009). Detection of the tagged or untagged photons in acousto-optic imaging of thick highly scattering media by photorefractive adaptive holography. *The European Physical Journal E*, 28(2):173–182.

Hale, G. and Querry, M. (1973). Optical constants of water in the 200-nm to 200-μm wavelength region. *Applied Optics*, 12(3):555–563.

Haskell, R. C., Svaasand, L. O., Tsay, T.-T., Feng, T.-C., McAdams, M. S., and Tromberg, B. J. (1994). Boundary conditions for the diffusion equation in radiative transfer. *Journal of the Optical Society of America A*, 11(10):2727–2741.

Henyey, L. G. and Greenstein, J. L. (1941). Diffuse radiation in the galaxy. *The Astrophysical Journal*, 93:70–83.

Hill, C. and Ter Haar, G. (1995). High intensity focused ultrasound—potential for cancer treatment. *The British Journal of Radiology*, 68(816):1296–1303.

Huang, L. and Liu, L.-S. (2009). Simultaneous determination of thermal conductivity and thermal diffusivity of food and agricultural materials using a transient plane-source method. *Journal of Food Engineering*, 95(1):179–185.

Hynynen, K., Freund, W. R., Cline, H. E., Chung, A. H., Watkins, R. D., Vetro, J. P., and Jolesz, F. A. (1996). A clinical, noninvasive, MR imaging-monitored ultrasound surgery method. *Radiographics*, 16(1):185–195.

Illing, R., Kennedy, J., Wu, F., Ter Haar, G., Protheroe, A., Friend, P., Gleeson, F., Cranston, D., Phillips, R., and Middleton, M. (2005). The safety and feasibility of extracorporeal high-intensity focused ultrasound (HIFU) for the treatment of liver and kidney tumours in a Western population. *British Journal of Cancer*, 93(8):890–895.

International Commission on Non-Ionizing Radiation Protection (1996). Guidelines on limits of exposure to laser radiation of wavelengths between 180 nm and 1,000 nm.

Ishihara, Y., Calderon, A., Watanabe, H., Okamoto, K., Suzuki, Y., Kuroda, K., and Suzuki, Y. (1995). A precise and fast temperature mapping using water proton chemical shift. *Magnetic Resonance in Medicine*, 34(6):814–823.

Ishimaru, A. (1978). *Wave propagation and scattering in random media*. Academic Press, 6 edition.

Jacques, S. (1996). *Biomedical Optical Instrumentation and Laser-Assisted Biotechnology*, chapter 1, pages 21–32. Kluwer Academic.

Jacques, S. and Gaeeni, M. (1989). Thermically induced changes in optical properties of heart. *Proceedings of the 11th International Conference on Engineering in Medicine and Biology*, 11, Part 4/6:1199–1200.

Jacques, S. L. (2013). Optical properties of biological tissues: a review. *Physics in Medicine & Biology*, 58(11):R37–R61.

Jacques, S. L., Newman, C., and He, X.-Y. (1991). Thermal coagulation of tissues: liver studies indicate a distribution of rate parameters, not a single rate parameter, describes the coagulation process. In *J. McGrath (ed.) Advances in Biological Heat and Mass Transfer, 1991. New York: ASME*, pages 71–73.

Jacques, S. L. and Pogue, B. W. (2008). Tutorial on diffuse light transport. *Journal of Biomedical Optics*, 13(4):041302.

Jensen, C. R., Ritchie, R. W., Gyöngy, M., Collin, J. R., Leslie, T., and Coussios, C.-C. (2012). Spatiotemporal monitoring of high-intensity focused ultrasound therapy with passive acoustic mapping. *Radiology*, 262(1):252–261.

Jiménez, J. and Hita, E. (2001). Babinet's principle in scalar theory of diffraction. *Optical Review*, 8(6):495–497.

Kempe, M., Larionov, M., Zaslavsky, D., and Genack, A. (1997). Acousto-optic tomography with multiply scattered light. *Journal of the Optical Society of America A*, 14(5):1151–1158.

Kennedy, J. (2005). High-intensity focused ultrasound in the treatment of solid tumours. *Nature Reviews Cancer*, 5(4):321–327.

Khokhlova, T. D., Canney, M. S., Lee, D., Marro, K. I., Crum, L. A., Khokhlova, V. A., and Bailey, M. R. (2009). Magnetic resonance imaging of boiling induced by high intensity focused ultrasound. *The Journal of the Acoustical Society of America*, 125(4):2420–2431.

Khokhlova, T. D., Pelivanov, I. M., Sapozhnikov, O. A., Solomatin, V. S., and Karabutov, A. A. (2006). Opto-acoustic diagnostics of the thermal action of high-intensity focused ultrasound on biological tissues: the possibility of its applications and model experiments. *Quantum Electronics*, 36(12):1097–1102.

Kienle, A. and Patterson, M. S. (1997). Improved solutions of the steady-state and the time-resolved diffusion equations for reflectance from a semi-infinite turbid medium. *Journal of the Optical Society of America A*, 14(1):246–254.

Kim, B.-M., Jacques, S. L., Rastegar, S., Thomsen, S., and Motamedi, M. (1996). Nonlinear finite-element analysis of the role of dynamic changes in blood perfusion and optical properties in laser coagulation of tissue. *IEEE Journal of Selected Topics in Quantum Electronics*, 2(4):922–933.

Kim, C., Wang, L. V., Vellekoop, I., Mosk, A., Wu, T. T., Qu, J. Y., Xu, M., Cottrell, W., Wilson, J., Foster, T., et al. (2007). Multi-optical-wavelength ultrasound-modulated optical tomography: a phantom study. *Optics Letters*, 32(16):2285–2287.

Kim, Y.-s., Park, M. J., Keserci, B., Nurmilaukas, K., Köhler, M. O., Rhim, H., and Lim, H. K. (2014). Uterine fibroids: postsonication temperature decay rate enables prediction of therapeutic responses to MR imaging-guided high-intensity focused ultrasound ablation. *Radiology*, 270(2):589–600.

Kingston, R. H. (1995). *Optical sources, detectors, and systems: fundamentals and applications*. Academic Press.

Koelzer, J. G., Mitic, G., Otto, J., and Zinth, W. (1995). Measurements of the optical properties of breast tissue using time-resolved transillumination. In *International Symposium on Biomedical Optics Europe '94*, pages 143–152. International Society for Optics and Photonics.

Kothapalli, S.-R. and Wang, L. V. (2008). Ultrasound-modulated optical microscopy. *Journal of Biomedical Optics*, 13(5):054046.

Kothapalli, S.-R. and Wang, L. V. (2009). *Ex vivo* blood vessel imaging using ultrasound-modulated optical microscopy. *Journal of Biomedical Optics*, 14(1): 014015.

Laforest, T., Dupret, A., Verdant, A., Ramaz, F., Gigan, S., Tessier, G., and la Guillaume, E. B. (2013). A 4000 Hz CMOS image sensor with in-pixel processing for light measurement and modulation. In *2013 IEEE 11th International New Circuits and Systems Conference (NEWCAS)*. IEEE.

Lai, P. (2010). *Photorefractive crystal-based acousto-optic imaging in the near-infrared and its applications*. PhD thesis, Boston University.

Lai, P., McLaughlan, J. R., Draudt, A. B., Murray, T. W., Cleveland, R. O., and Roy, R. A. (2011). Real-time monitoring of high-intensity focused ultrasound lesion formation using acousto-optic sensing. *Ultrasound in Medicine & Biology*, 37(2):239–252.

Lai, P., Roy, R. A., and Murray, T. W. (2009). Quantitative characterization of turbid media using pressure contrast acousto-optic imaging. *Optics Letters*, 34(18):2850–2852.

Lai, P., Suzuki, Y., Xu, X., and Wang, L. V. (2013). Exploring ultrasound-modulated optical tomography at clinically useful depths using the photorefractive effect. In *SPIE BiOS*, page 85812X. International Society for Optics and Photonics.

Lai, P., Xu, X., and Wang, L. V. (2012). Ultrasound-modulated optical tomography at new depth. *Journal of Biomedical Optics*, 17(6):0660061–0660066.

Le Clerc, F., Collot, L., and Gross, M. (2000). Numerical heterodyne holography with two-dimensional photodetector arrays. *Optics Letters*, 25(10):716–718.

Lesaffre, M., Jean, F., Ramaz, F., Boccara, A.-C., Gross, M., Delaye, P., and Roosen, G. (2007). In situ monitoring of the photorefractive response time in a self-adaptive wavefront holography setup developed for acousto-optic imaging. *Optics Express*, 15(3):1030–1042.

Leutz, W. and Maret, G. (1995). Ultrasonic modulation of multiply scattered light. *Physica B: Condensed Matter*, 204(1):14–19.

Lev, A. and Sfez, B. (2003). *In vivo* demonstration of the ultrasound-modulated light technique. *Journal of the Optical Society of America A*, 20(12):2347–2354.

Leveque, S., Boccara, A., et al. (1999). Ultrasonic tagging of photon paths in scattering media: parallel speckle modulation processing. *Optics Letters*, 24(3):181–183.

Li, J., Ku, G., and Wang, L. V. (2002). Ultrasound-modulated optical tomography of biological tissue by use of contrast of laser speckles. *Applied Optics*, 41(28):6030–6035.

Li, Y., Hemmer, P., Kim, C., Zhang, H., and Wang, L. V. (2008a). Detection of ultrasound-modulated diffuse photons using spectral-hole burning. *Optics Express*, 16(19):14862–14874.

Li, Y., Zhang, H., Kim, C., Wagner, K. H., Hemmer, P., and Wang, L. V. (2008b). Pulsed ultrasound-modulated optical tomography using spectral-hole burning as a narrowband spectral filter. *Applied Physics Letters*, 93(1):011111.

Lynn, J. and Putnam, T. (1944). Histology of cerebral lesions produced by focused ultrasound. *The American Journal of Pathology*, 20(3):637–642.

Lynn, J., Zwemer, R., Chick, A., and Miller, A. (1942). A new method for the generation and use of focused ultrasound in experimental biology. *The Journal of General Physiology*, 26(2):179–193.

Ma, X., Lu, J. Q., Brock, R. S., Jacobs, K. M., Yang, P., and Hu, X.-H. (2003). Determination of complex refractive index of polystyrene microspheres from 370 to 1610 nm. *Physics in Medicine & Biology*, 48(24):4165–4172.

Mahan, G., Engler, W., Tiemann, J., and Uzgiris, E. (1998). Ultrasonic tagging of light: theory. *Proceedings of the National Academy of Sciences*, 95(24):14015–14019.

Marks, F. A., Tomlinson, H. W., and Brooksby, G. W. (1993). Comprehensive approach to breast cancer detection using light: photon localization by ultrasound modulation and tissue characterization by spectral discrimination. In *OE/LASE '93: Optics, Electro-Optics, & Laser Applications in Science & Engineering*, pages 500–510. International Society for Optics and Photonics.

Maxwell, J. (1865). A dynamical theory of the electromagnetic field. *Philosophical Transactions of the Royal Society of London*, 155:459–512.

McDannold, N. (2005). Quantitative MRI-based temperature mapping based on the proton resonant frequency shift: review of validation studies. *International Journal of Hyperthermia*, 21(6):533–546.

Meade, M. L. (1983). *Lock-in amplifiers: principles and applications*. Peregrinus.

Meaney, P. M., Cahill, M. D., and ter Haar, G. (2000). The intensity dependence of lesion position shift during focused ultrasound surgery. *Ultrasound in Medicine & Biology*, 26(3):441–450.

Meshorer, A., Prionas, S., Fajardo, L., Meyer, J., Hahn, G., and Martinez, A. (1983). The effects of hyperthermia on normal mesenchymal tissues. Application of a histologic grading system. *Archives of Pathology & Laboratory Medicine*, 107(6):328–334.

Metropolis, N. (1987). The beginning of the Monte Carlo method. *Los Alamos Science*, 15(584):125–130.

Millerd, J. E., Ziari, M., and Partovi, A. (1998). *Photorefractivity in Semiconductors, in Nonlinear Optics in Semiconductors I*, volume 58, chapter 5. Academic Press.

Mo, S., Coussios, C.-C., Seymour, L., and Carlisle, R. (2012). Ultrasound-enhanced drug delivery for cancer. *Expert Opinion on Drug Delivery*, 9(12):1525–1538.

Monchalin, J.-P. (1985). Optical detection of ultrasound at a distance using a confocal Fabry–Perot interferometer. *Applied Physics Letters*, 47(1):14–16.

Monchalin, J.-P., Heon, R., Bouchard, P., and Padioleau, C. (1989). Broadband optical detection of ultrasound by optical sideband stripping with a confocal Fabry–Perot. *Applied Physics Letters*, 55(16):1612–1614.

Murray, T. W., Lai, P., and Roy, R. A. (2012). Measuring tissue properties and monitoring therapeutic responses using acousto-optic imaging. *Annals of Biomedical Engineering*, 40(2):474–485.

Murray, T. W. and Roy, R. A. (2008). Illuminating sound: Imaging tissue optical properties with ultrasound. *Acoustics Today*, 3(3):17–24.

Murray, T. W., Sui, L., Maguluri, G., Roy, R. A., Nieva, A., Blonigen, F., and DiMarzio, C. A. (2004). Detection of ultrasound-modulated photons in diffuse media using the photorefractive effect. *Optics Letters*, 29(21):2509–2511.

Nandlall, S. D., Jackson, E., and Coussios, C.-C. (2011). Real-time passive acoustic monitoring of HIFU-induced tissue damage. *Ultrasound in Medicine & Biology*, 37(6):922–934.

Nandlall, S. D., Schiffter, H. A., Vonhoff, S., Bazán-Peregrino, M., Arora, M., and Coussios, C.-C. (2010). Real-time optical measurement of biologically relevant thermal damage in tissue-mimicking hydrogels containing bovine serum albumin. *International Journal of Hyperthermia*, 26(5):456–464.

Newman, C. and Jacques, S. (1991). Laser penetration into prostate for various wavelengths. *Lasers in Surgery and Medicine (Suppl3)*, page 75.

Nightingale, K. R., Palmeri, M. L., Nightingale, R. W., and Trahey, G. E. (2001). On the feasibility of remote palpation using acoustic radiation force. *The Journal of the Acoustical Society of America*, 110(1):625–634.

Nikitin, S. M., Khokhlova, T. D., and Pelivanov, I. M. (2012). Temperature dependence of the optoacoustic transformation efficiency in *ex vivo* tissues for application in monitoring thermal therapies. *Journal of Biomedical Optics*, 17(6):0612141–0612149.

Nilsson, A. M., Sturesson, C., Liu, D. L., and Andersson-Engels, S. (1998). Changes in spectral shape of tissue optical properties in conjunction with laser-induced thermotherapy. *Applied optics*, 37(7):1256–1267.

O'Neil, H. (1949). Theory of focusing radiators. *The Journal of the Acoustical Society of America*, 21(5):516–526.

Pantelides, M., Whitehurst, C., Moore, J. V., King, T., and Blacklock, N. (1990). Photodynamic therapy for localised prostatic cancer: light penetration in the human prostate gland. *The Journal of urology*, 143(2):398–401.

Parker, K. J. (1983). The thermal pulse decay technique for measuring ultrasonic absorption coefficients. *The Journal of the Acoustical Society of America*, 74(5):1356–1361.

Parker, K. J. (1985). Effects of heat conduction and sample size on ultrasonic absorption measurements. *The Journal of the Acoustical Society of America*, 77(2):719–725.

Pazdur, R. and Hoskins, W. J. (2003). *Cancer management: a multidisciplinary approach: medical, surgical & radiation oncology*. Oncology Group.

Pearce, J. A. (2009). Relationship between Arrhenius models of thermal damage and the CEM 43 thermal dose. In *Proceedings of SPIE 7181, Energy-based Treatment of Tissue and Assessment V*. 718104 (February 23, 2009); doi:10.1117/12.807999.

Pennes, H. H. (1948). Analysis of tissue and arterial blood temperatures in the resting human forearm. *Journal of Applied Physiology*, 1(2):93–122.

Phatak, S. and Rao, S. S. (1995). Logistic map: A possible random-number generator. *Physical Review E*, 51(4):3670–3678.

Pickering, J. W., Prahl, S. A., Van Wieringen, N., Beek, J. F., Sterenborg, H. J., and Van Gemert, M. J. (1993). Double-integrating-sphere system for measuring the optical properties of tissue. *Applied Optics*, 32(4):399–410.

Pierce, A. D. (1989). *Acoustics: an introduction to its physical principles and applications*. Acoustical Society of America.

Pifferi, A., Swartling, J., Chikoidze, E., Andersson-Engels, S., Cubeddu, R., Torricelli, A., Taroni, P., and Bassi, A. (2004). Spectroscopic time-resolved diffuse reflectance and transmittance measurements of the female breast at different interfiber distances. *Journal of Biomedical Optics*, 9(6):1143–1151.

Pogue, B. W. and Patterson, M. S. (2006). Review of tissue simulating phantoms for optical spectroscopy, imaging and dosimetry. *Journal of Biomedical Optics*, 11(4):0411021–04110216.

Powell, S. and Leung, T. S. (2012). Highly parallel Monte-Carlo simulations of the acousto-optic effect in heterogeneous turbid media. *Journal of Biomedical Optics*, 17(4):045002.

Powell, S. and Leung, T. S. (2013a). Acousto-optic monitoring of high-intensity focused ultrasound lesion formation with fibre-coupled autocorrelation detection. In *Proceedings of Meetings on Acoustics*, volume 15, page 075004. Acoustical Society of America.

Powell, S. and Leung, T. S. (2013b). Linear reconstruction of absorption perturbations in coherent ultrasound-modulated optical tomography. *Journal of Biomedical Optics*, 18(12):126020.

Powell, S. and Leung, T. S. (2014). Quantitative reconstruction of absorption and scattering coefficients in ultrasound-modulated optical tomography. In *Proceedings of SPIE*, volume 8943, pages 89434X–1.

Prahl, S., van Gemert, M., and Welch, A. (1993). Determining the optical properties of turbid media by using the adding–doubling method. *Applied Optics*, 32(4):559–568.

Prahl, S. A. (1995). The adding-doubling method. In *Optical-thermal response of laser-irradiated tissue*, pages 101–129. Springer.

Prahl, S. A. (2012a). A compendium of tissue optical properties. *http://omlc.ogi.edu/spectra*.

Prahl, S. A. (2012b). Mie scattering calculator. *http://omlc.ogi.edu/calc/mie_calc.html*.

Prahl, S. A. (2013). Inverse adding–doubling software. *http://omlc.ogi.edu/software/iad/index.html*.

Prost, A., Funke, A., Tanter, M., Bossy, E., et al. (2012). Photoacoustic-guided ultrasound therapy with a dual-mode ultrasound array. *Journal of Biomedical Optics*, 17(6):0612051–0612056.

Rabkin, B. A., Zderic, V., Crum, L. A., and Vaezy, S. (2006). Biological and physical mechanisms of HIFU-induced hyperecho in ultrasound images. *Ultrasound in Medicine & Biology*, 32(11):1721–1729.

Rabkin, B. A., Zderic, V., and Vaezy, S. (2005). Hyperecho in ultrasound images of HIFU therapy: involvement of cavitation. *Ultrasound in Medicine & Biology*, 31(7):947–956.

Raman, C. and Nagendra Nath, N. (1935). The diffraction of light by high frequency sound waves. In *Proceedings of the Indian Academy of Sciences, Section A*, volume 2:406-420; 3:75-84; 3:119-125; 3:459-465, 4:222-242. Indian Academy of Sciences.

Ramaz, F., Forget, B., Atlan, M., Boccara, A.-C., Gross, M., Delaye, P., and Roosen, G. (2004). Photorefractive detection of tagged photons in ultrasound modulated optical tomography of thick biological tissues. *Optics Express*, 12(22):5469–5474.

Rassweiler, J. J., Knoll, T., Köhrmann, K.-U., McAteer, J. A., Lingeman, J. E., Cleveland, R. O., Bailey, M. R., and Chaussy, C. (2011). Shock wave technology and application: an update. *European Urology*, 59(5):784–796.

Righetti, R., Kallel, F., Stafford, R. J., Price, R. E., Krouskop, T. A., Hazle, J. D., and Ophir, J. (1999). Elastographic characterization of HIFU-induced lesions in canine livers. *Ultrasound in Medicine & Biology*, 25(7):1099–1113.

Ritz, J.-P., Roggan, A., Isbert, C., Müller, G., Buhr, H. J., and Germer, C.-T. (2001). Optical properties of native and coagulated porcine liver tissue between 400 and 2400 nm. *Lasers in Surgery and Medicine*, 29(3):205–212.

Rivens, I., Shaw, A., Civale, J., and Morris, H. (2007). Treatment monitoring and thermometry for therapeutic focused ultrasound. *International Journal of Hyperthermia*, 23(2):121–139.

Rousseau, G., Blouin, A., and Monchalin, J.-P. (2008). Ultrasound-modulated optical imaging using a powerful long pulse laser. *Optics Express*, 16(17):12577–12590.

Rousseau, G., Blouin, A., and Monchalin, J.-P. (2009). Ultrasound-modulated optical imaging using a high-power pulsed laser and a double-pass confocal fabry-perot interferometer. *Optics Letters*, 34(21):3445–3447.

Royston, D. D., Poston, R. S., and Prahl, S. A. (1996). Optical properties of scattering and absorbing materials used in the development of optical phantoms at 1064 nm. *Journal of Biomedical Optics*, 1(1):110–116.

Rubinstein, R. Y. and Kroese, D. P. (2007). *Simulation and the Monte Carlo method*. John Wiley & Sons, 2nd edition.

Sakadžić, S. and Wang, L. V. (2002). Ultrasonic modulation of multiply scattered coherent light: an analytical model for anisotropically scattering media. *Physical Review E*, 66(2):026603.

Sakadžić, S. and Wang, L. V. (2004). High-resolution ultrasound-modulated optical tomography in biological tissues. *Optics Letters*, 29(23):2770–2772.

Sakadžić, S. and Wang, L. V. (2005). Modulation of multiply scattered coherent light by ultrasonic pulses: an analytical model. *Physical Review E*, 72(3):036620.

Sakadžić, S. and Wang, L. V. (2006a). Correlation transfer and diffusion of ultrasound-modulated multiply scattered light. *Physical Review Letters*, 96(16):163902.

Sakadžić, S. and Wang, L. V. (2006b). Correlation transfer equation for ultrasound-modulated multiply scattered light. *Physical Review E*, 74(3):036618.

Sanghvi, N. T., Fry, F. J., Bihrle, R., Foster, R. S., Phillips, M. H., Syrus, J., Zaitsev, A. V., and Hennige, C. W. (1996). Noninvasive surgery of prostate tissue by high-intensity focused ultrasound. *IEEE Transactions on Ultrasonics, Ferroelectrics and Frequency Control*, 43(6):1099–1110.

Sapareto, S. A. and Dewey, W. C. (1984). Thermal dose determination in cancer therapy. *International Journal of Radiation Oncology*Biology*Physics*, 10(6):787–800.

Sibille, A., Prat, F., Chapelon, J.-Y., Abou El Fadil, F., Henry, L., Theilliere, Y., Ponchon, T., and Cathignol, D. (1993). Characterization of extracorporeal ablation of normal and tumor-bearing liver tissue by high intensity focused ultrasound. *Ultrasound in Medicine & Biology*, 19(9):803–813.

Skinner, M. G., Everts, S., Reid, A. D., Vitkin, I. A., Lilge, L., and Sherar, M. D. (2000). Changes in optical properties of *ex vivo* rat prostate due to heating. *Physics in Medicine & Biology*, 45(5):1375–1386.

Solymar, L., Webb, D. J., and Grunnet-Jepsen, A. (1996). *The physics and applications of photorefractive materials*. Oxford University Press.

Stepanishen, P. R. and Benjamin, K. C. (1982). Forward and backward projection of acoustic fields using FFT methods. *The Journal of the Acoustical Society of America*, 71(4):803–812.

Sui, L. (2006). *Acousto-optic imaging in diffuse media using pulsed ultrasound and the photorefractive effect*. PhD thesis, Boston University.

Sui, L., Roy, R. A., DiMarzio, C. A., and Murray, T. W. (2005). Imaging in diffuse media with pulsed-ultrasound-modulated light and the photorefractive effect. *Applied Optics*, 44(19):4041–4048.

Sun, P. and Wang, Y. (2010). Measurements of optical parameters of phantom solution and bulk animal tissues *in vitro* at 650nm. *Optics & Laser Technology*, 42(1):1–7.

Suzuki, Y., Lai, P., Xu, X., and Wang, L. (2013). High-sensitivity ultrasound-modulated optical tomography with a photorefractive polymer. *Optics Letters*, 38(6):899–901.

Teich, M. C. and Saleh, B. (1991). Fundamentals of photonics. *Canada, Wiley Interscience*, page 3.

Tempany, C. M., McDannold, N. J., Hynynen, K., and Jolesz, F. A. (2011). Focused ultrasound surgery in oncology: overview and principles. *Radiology*, 259(1):39–56.

ter Haar, G. (1995). Ultrasound focal beam surgery. *Ultrasound in medicine & biology*, 21(9):1089–1100.

ter Haar, G. (2004). *Physical principles of medical ultrasonics*, volume 2, chapter 13, pages 407–456. Wiley Online Library.

ter Haar, G. (2012). Principles of high-intensity focused ultrasound. In *Interventional Oncology*, pages 51–63. Springer.

ter Haar, G. and Coussios, C. (2007a). High intensity focused ultrasound: past, present and future. *International Journal of Hyperthermia*, 23(2):85–87.

ter Haar, G. and Coussios, C. (2007b). High intensity focused ultrasound: physical principles and devices. *International Journal of Hyperthermia*, 23(2):89–104.

ter Haar, G., Sinnett, D., and Rivens, I. (1989). High intensity focused ultrasound-a surgical technique for the treatment of discrete liver tumours. *Physics in Medicine & Biology*, 34(11):1743.

Thomsen, S. and Pearce, J. A. (2011). *Optical-thermal response of laser-irradiated tissue*, chapter 13, pages 487–549. Springer Science+Business Media, 2nd edition.

Thomsen, S. L., Vijverberg, H., Huang, R., and Schwartz, J. A. (1993). Changes in optical properties of rat skin during thermal coagulation. *Proceedings of SPIE*, 1882:230–236.

Torres, J. H., Welch, A. J., Çilesiz, I., and Motamedi, M. (1994). Tissue optical property measurements: overestimation of absorption coefficient with spectrophotometric techniques. *Lasers in Surgery and Medicine*, 14(3):249–257.

Tuchin, V. V. (2002). *Handbook of optical biomedical diagnostics*. SPIE press.

Vaezy, S., Shi, X., Martin, R. W., Chi, E., Nelson, P. I., Bailey, M. R., and Crum, L. A. (2001). Real-time visualization of high-intensity focused ultrasound treatment using ultrasound imaging. *Ultrasound in Medicine & Biology*, 27(1):33–42.

Van Der Ziel, A. (1970). Noise in solid-state devices and lasers. *Proceedings of the IEEE*, 58(8):1178–1206.

Vo-Dinh, T. (2010). *Biomedical photonics handbook*. CRC press.

Wagner, N. R. (1992). The logistic lattice in random number generation. In *Proceedings of the annual Allerton Conference on Communication, Control, and Computing*, volume 30, pages 922–922. University of Illinois.

Wang, L., Jacques, S., and Zheng, L. (1995a). MCML–Monte Carlo modeling of light transport in multi-layered tissues. *Computer Methods and Programs in Biomedicine*, 47(2):131–146.

Wang, L., Jacques, S. L., and Zhao, X. (1995b). Continuous-wave ultrasonic modulation of scattered laser light to image objects in turbid media. *Optics Letters*, 20(6):629–631.

Wang, L. and Zhao, X. (1997). Ultrasound-modulated optical tomography of absorbing objects buried in dense tissue-simulating turbid media. *Applied Optics*, 36(28):7277–7282.

Wang, L. V. (2001a). Mechanisms of ultrasonic modulation of multiply scattered coherent light: a Monte Carlo model. *Optics Letters*, 26(15):1191–1193.

Wang, L. V. (2001b). Mechanisms of ultrasonic modulation of multiply scattered coherent light: an analytic model. *Physical Review Letters*, 87(4):043903.

Wang, L. V. and Wu, H.-i. (2012). *Biomedical optics: principles and imaging*. John Wiley & Sons.

Watson, T. (2008). Ultrasound in contemporary physiotherapy practice. *Ultrasonics*, 48(4):321–329.

Wu, F., Chen, W.-Z., Bai, J., Zou, J.-Z., Wang, Z.-L., Zhu, H., and Wang, Z.-B. (2001). Pathological changes in human malignant carcinoma treated with high-intensity focused ultrasound. *Ultrasound in Medicine & Biology*, 27(8):1099–1106.

Wu, F., Wang, Z.-B., Chen, W.-Z., Zhu, H., Bai, J., Zou, J.-Z., Li, K.-Q., Jin, C.-B., Xie, F.-L., and Su, H.-B. (2004). Extracorporeal high intensity focused ultrasound ablation in the treatment of patients with large hepatocellular carcinoma. *Annals of Surgical Oncology*, 11(12):1061–1069.

Wu, F., Zhou, L., and Chen, W. R. (2007). Host antitumour immune responses to HIFU ablation. *International Journal of Hyperthermia*, 23(2):165–171.

Wu, P. and Stepinski, T. (1999). Extension of the angular spectrum approach to curved radiators. *The Journal of the Acoustical Society of America*, 105(5):2618–2627.

Xu, M. and Wang, L. V. (2006). Photoacoustic imaging in biomedicine. *Review of Scientific Instruments*, 77(4):041101.

Xu, X., Kothapalli, S.-R., Liu, H., and Wang, L. V. (2010). Spectral hole burning for ultrasound-modulated optical tomography of thick tissue. *Journal of Biomedical Optics*, 15(6):066018.

Xu, X., Zhang, H., Hemmer, P., Qing, D.-k., Kim, C., and Wang, L. V. (2007). Photorefractive detection of tissue optical and mechanical properties by ultrasound modulated optical tomography. *Optics Letters*, 32(6):656–658.

Yamaguchi, I. and Zhang, T. (1997). Phase-shifting digital holography. *Optics Letters*, 22(16):1268–1270.

Yang, X. (2003). Investigation of bubble dynamics and heating during focused ultrasound insonation in tissue-mimicking materials. *The Journal of the Acoustical Society of America*, 114(4):1704.

Yang, Y., Welch, A., and Rylander, H. (1991). Rate process parameters of albumen. *Lasers in Surgery and Medicine*, 11(2):188–190.

Yao, G., Jiao, S., and Wang, L. V. (2000). Frequency-swept ultrasound-modulated optical tomography in biological tissue by use of parallel detection. *Optics Letters*, 25(10):734–736.

Yaroslavsky, A., Schulze, P., Yaroslavsky, I., Schober, R., Ulrich, F., and Schwarzmaier, H. (2002). Optical properties of selected native and coagulated human brain tissues *in vitro* in the visible and near infrared spectral range. *Physics in Medicine & Biology*, 47(12):2059–2073.

CURRICULUM VITAE

Matthew Tyler Adams

CONTACT

Address Department of Mechanical Engineering
110 Cummington Mall, Boston, MA 02215
Email adamsm2@bu.edu

EDUCATION

Boston University — Boston, MA
Ph.D., Mechanical Engineering — 2012-2015

Boston University — Boston, MA
M.S., Mechanical Engineering — 2009-2012

Union College — Schenectady, NY
B.S., Mechanical Engineering, Minor: Bioengineering — 2005-2009

PROFESSIONAL DEVELOPMENT

Whitaker Enrichment Seminar — May, 2014
Rome, Italy

ESHO School on Thermal Cancer Therapy — February, 2014
Devon, UK

Physical Acoustics Summer School — May, 2012
Oxford, MS

RESEARCH AND PROFESSIONAL EXPERIENCE

Graduate Research Assistant — Boston University
Boston, MA — *May 2010 – December 2014*

Whitaker International Fellow — University of Oxford
Oxford, UK — *January – September 2014*

Naval Research Enterprise Internship Program — Naval Surface Warfare Center
Panama City, FL — *May – July 2013*

Undergraduate Research Assistant — Union College
Schenectady, NY — *June 2007 – April 2009*

Engineering Intern — Pervasis Therapeutics
Cambridge, MA — *August – September 2008*

TEACHING EXPERIENCE

Intro to Engineering Computation — Boston University
EK 127 — *Fall 2012*

Instrumentation & Theory of Experiments — Boston University
ME 310 — *Fall 2009 – Spring 2010*

HONORS AND AWARDS

Student Poster Award – Oxford Photonics Day	2014
Whitaker International Fellowship	2014
ICA Student Paper Award in Biomedical Acoustics	2013
NREIP Grantee	2013
Union College Departmental Honors	2009
Pi Tau Sigma, Alpha Alpha Chapter (President)	2009
Avon-Smith Fellowship for Engineering	2007

PUBLICATIONS

Refereed Journal Articles

Adams, M. T., Wang, Q., Cleveland, R. O., and Roy, R. A. (2014). Thermal dose dependent optical property changes of ex vivo chicken breast tissues between 500 and 1100 nm. *Physics in medicine and biology*, 59(13):3249.

Adams, M. T., Cleveland, R. O., and Roy, R. A. (2014). A modeling-based design and assessment of an acousto-optic guided high-intensity focused ultrasound system. *Journal of Biomedical Optics*, UNDER REVIEW.

Conference Presentations and Invited Lectures

Adams, M. T., Cleveland, R. O., and Roy, R. A. Modeling acousto-optic guided high-intensity focused ultrasound lesion formation. *39th International Symposium on Ultrasound in Tissue Characterization*, June, 2014.

Adams, M. T., Cleveland, R. O., and Roy, R. A. Guiding high-intensity focused ultrasound therapies with the interaction between light and sound. *Erasmus Medical Center*, May, 2014.

Adams, M. T., Cleveland, R. O., and Roy, R. A. Treatment planning and strategies for acousto-optic guided high-intensity focused ultrasound therapies. *167th Meeting of the Acoustical Society of America*, May, 2014.

Adams, M. T., Cleveland, R. O., and Roy, R. A. Treatment planning and strategies for acousto-optic guided high-intensity focused ultrasound therapies. *5th Anual Oxford Photonics Day*, April, 2014.

Adams, M. T., Cleveland, R. O., and Roy, R. A. Treatment planning and strategies for acousto-optic guided high-intensity focused ultrasound therapies. *14th International Symposium on Therapeutic Ultrasound*, April, 2014.

Adams, M. T., Cleveland, R. O., and Roy, R. A. Treatment planning and strategies for acousto-optic guided high-intensity focused ultrasound therapies. *Whitaker Enrichment Seminar*, March, 2014.

Adams, M. T., Cleveland, R. O., and Roy, R. A. Improving the acousto-optic detection of high-intensity focused ultrasound lesions. *21st International Congress on Acoustics*, June, 2013.

Adams, M. T., Giraud, D.S.H., Cleveland, R. O., and Roy, R. A. Modeling acousto-optic sensing of high-intensity focused ultrasound lesion formation. *164th Meeting of the Acoustical Society of America*, October, 2012.

Adams, M. T., Giraud, D.S.H., Cleveland, R. O., and Roy, R. A. Modeling the acousto-optic sensing of high-intensity focused ultrasound lesions in real time. *Boston University Science & Engineering Research Symposium*, March, 2012.

Giraud, D.S.H., **Adams, M. T.**, Cleveland, R. O., and Roy, R. A. GPU Based Simulations of Light Propagation in Turbid Media. *3rd Annual Boston University Translational Research Symposium*, April, 2012.

Adams, M. T., Cleveland, R. O., and Roy, R. A. Modeling the propagation of light

through turbid media by means of the diffusion approximation to the radiative transfer equation. *Boston University Science & Engineering Research Symposium*, March, 2011.

Adams, M. T., Bucinell, R.B. The photogrammetry of bullfrog hearts. *19th Annual Steinmetz Symposium*, May, 2009.

Adams, M. T., Bucinell, R.B. In-vivo measurements of strain field gradients in an amphibian heart. *23rd National Conference on Undergraduate Research*, April, 2009.